Solar Phys (2011) 269: 169–236
DOI 10.1007/s11207-010-9685-2

Coronal-Temperature-Diagnostic Capability of the *Hinode*/*X-Ray Telescope* Based on Self-Consistent Calibration

N. Narukage · T. Sakao · R. Kano · H. Hara · M. Shimojo · T. Bando · F. Urayama · E. DeLuca · L. Golub · M. Weber · P. Grigis · J. Cirtain · S. Tsuneta

Received: 19 February 2010 / Accepted: 24 November 2010 / Published online: 1 January 2011

Abstract The *X-Ray Telescope* (XRT) onboard the *Hinode* satellite is an X-ray imager that observes the solar corona with unprecedentedly high angular resolution (consistent with its 1″ pixel size). XRT has nine X-ray analysis filters with different temperature responses. One of the most significant scientific features of this telescope is its capability of diagnosing coronal temperatures from less than 1 MK to more than 10 MK, which has never been accomplished before. To make full use of this capability, accurate calibration of the coronal temperature response of XRT is indispensable and is presented in this article. The effect of on-orbit contamination is also taken into account in the calibration. On the basis of our calibration results, we review the coronal-temperature-diagnostic capability of XRT.

Keywords Corona · Instrumentation and data management

N. Narukage (✉) · R. Kano · H. Hara · T. Bando · S. Tsuneta
National Astronomical Observatory of Japan (NAOJ), 2-21-1 Osawa, Mitaka, Tokyo, 181-8588, Japan
e-mail: noriyuki.narukage@nao.ac.jp

N. Narukage
e-mail: narukage@solar.isas.jaxa.jp

T. Sakao
Institute of Space and Astronautical Science/Japan Aerospace Exploration Agency (ISAS/JAXA), 3-1-1 Yoshinodai, Sagamihara, Kanagawa, 229-8510, Japan

M. Shimojo
Nobeyama Solar Radio Observatory/National Astronomical Observatory of Japan, Minamimaki, Minamisaku, Nagano, 384-1305, Japan

F. Urayama
Space Engineering Development Co., Ltd., 1-12-2 Takezono, Tsukuba, Ibaraki, 305-0032, Japan

E. DeLuca · L. Golub · M. Weber · P. Grigis
Smithsonian Astrophysical Observatory, 60 Garden Street, Cambridge, MA 02138, USA

J. Cirtain
NASA/Marshall Space Flight Center, Huntsville, AL 35812, USA

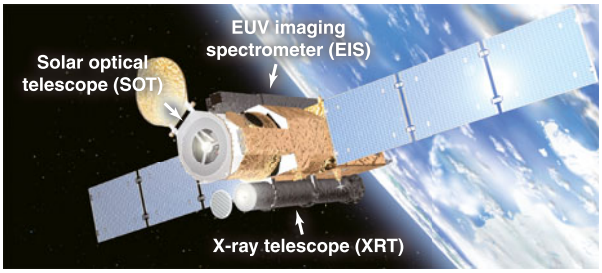

Figure 1 The *Hinode* satellite has three telescopes, namely the *Solar Optical Telescope* (SOT), *EUV Imaging Spectrometer* (EIS), and the *X-Ray Telescope* (XRT), to observe the Sun in different wavelengths. The XRT is mounted at the bottom of this image, as indicated. The size of *Hinode* is approximately 2 m (from XRT to EIS) $\times$ 10 m (between both ends of solar paddles) $\times$ 4 m (between Sun-facing and rear ends).

1. Introduction

The outer atmosphere of the Sun, the solar corona, is most clearly discernible when seen in soft X-rays. Since the early rocket experiments in the late 1960s, it has become widely recognized that soft X-ray imagery of the Sun provides a powerful means to investigate physical conditions of hot plasmas (whose temperature often exceeds 1 MK), which prevail in the corona. Coronal imaging with the *Soft X-ray Telescope* (SXT) onboard the *Yohkoh* (*Solar-A*) satellite (Ogawara *et al.*, 1991; Tsuneta *et al.*, 1991) (operation period: 1991 – 2001) covered a full solar-activity cycle and has revealed that magnetic reconnection plays an essential role in the energy-release processes in the dynamic solar corona.

The *Solar-B* satellite was launched at 21:36 UT on 22 September 2006. It was named *"Hinode"*, which means sunrise in Japanese (Kosugi *et al.*, 2007; Figure 1). The *X-Ray Telescope* (XRT) onboard *Hinode* is a successor of the *Yohkoh*/SXT. It also employs grazing-incidence optics, but with improved spatial resolution (consistent with $1''$ CCD pixel size compared with $\approx 2.5''$ pixel size in the case of SXT), while maintaining similar exposure cadence to that of SXT (only of the order of a few milli-seconds for flares and of the order of a few seconds for active regions). The XRT has the capability of imaging emission formed at much longer wavelengths than SXT. The combination of a backside-thinned CCD and thin Al-mesh filter allows XRT to image emission significantly longward of 60 Å. This is a major difference from *Yohkoh*/SXT in that the XRT can observe not only high-temperature plasmas (> 2 MK) seen with SXT, but also low-temperature (< 2 MK, reaching even below 1 MK) plasmas, which comprise a significant amount of the corona. With this enhanced temperature range for observing coronal plasmas, coupled with increased spatial resolution, the XRT is able to perform detailed imaging observations of a wide variety of coronal plasmas in a temperature range covering, continuously, from below 1 MK to well above 10 MK. One of the most significant scientific features of the XRT is its coronal-temperature-diagnostic capability, namely its capability to make temperature maps, for such plasmas.

In order to have XRT perform coronal-temperature diagnostics with its full capability, we carefully calibrated the effective area of the XRT and its response to coronal temperatures, using not only ground-based test data but also on-orbit data observed in X-rays and visible light. The effect of the on-orbit contamination, which manifested itself as decreasing intensity of the Sun's corona with time as imaged by XRT, was also calibrated as accurately as possible. On the basis of our calibration results, we review the coronal-temperature-diagnostic capability of XRT with the filter-ratio method.

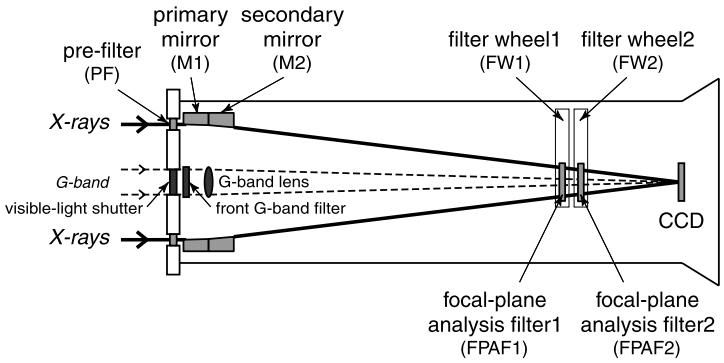

Figure 2 Optical elements of XRT. The solid line shows the optical path in X-rays. The optical elements for X-rays are the pre-filter (PF), primary mirror (M1), secondary mirror (M2), focal-plane analysis filters (FPAF1 and FPAF2) mounted on filter wheels (FW1 and FW2, respectively), and CCD. The optical path in visible light (G-band) is indicated by the dashed line. The optical elements for visible light are front G-band filter, G-band lens, G-band filter mounted on Filter Wheel 2 (FW2), and CCD.

In Section 2, the optical elements of XRT are briefly mentioned. In Section 3, we show an overview of the calibration performed in this article. In Section 4, we summarize how to identify the contaminant and how to measure its accumulating thickness on the focal-plane analysis filters (FPAFs) and CCD as a function of time. This then identifies the effective-area and temperature response of XRT including the contamination at every phase of the mission. In Section 5, we evaluate the coronal-temperature-diagnostic capability of XRT, explain the filter-ratio method to derive the coronal temperature, and present suitable filter pairs for each coronal temperature. An example of the coronal-temperature distribution with the XRT data is also shown. Finally, we summarize the result of this article in Section 6.

Additionally, in Appendix A, the calibration of the nine X-ray FPAFs with ground-based end-to-end test data is explained. In 2002 – 2003, the X-ray transmission measurement of the FPAFs was performed at the X-ray Astronomy Calibration and Testing (XACT) facility of the Istituto Nazionale di Astrofisica / Osservatorio Astronomico di Palermo "G.S. Vaiana" (Collura *et al.*, 1994). However, some of the calibrated FPAFs were unfortunately damaged. In this article, we characterize the complete flight set of FPAFs, namely both the un-damaged and re-manufactured FPAFs, with another ground-based test performed in 2005. Our calibrated thicknesses are consistent with the thicknesses available from XACT data.

An overview of the XRT scientific objectives, design, and performance of the XRT telescope are summarized by Golub *et al.* (2007), while the X-ray camera is described by Kano *et al.* (2008).

2. Optical Elements of XRT

In order to describe in detail the calibrations performed on the XRT, we first briefly describe the optical elements. Figure 2 shows the optical elements and optical paths of XRT. The XRT can take not only X-ray images but also visible-light (G-band) images for co-aligning images between XRT and other instruments mounted on *Hinode*. The solid and dashed lines in Figure 2 show the optical paths in X-rays and visible light, respectively.

The XRT optical elements for X-rays consist of a pre-filter (PF), two grazing-incidence mirrors (M1 and M2), two focal-plane analysis filters (FPAF1 and FPAF2), and a CCD.

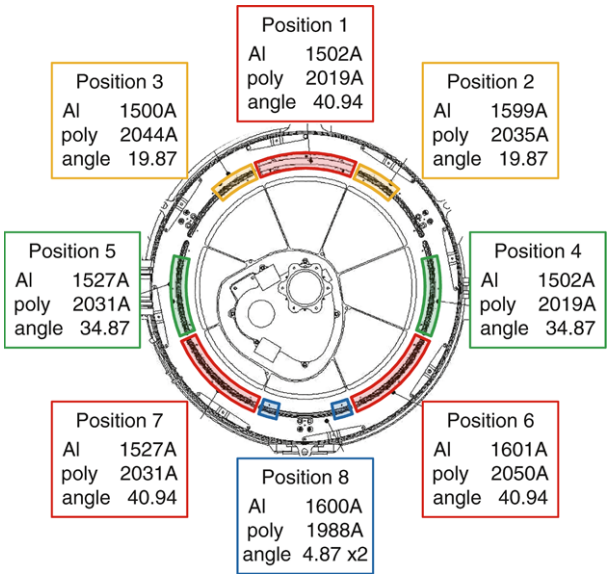

Figure 3 Entrance aperture and pre-filter of XRT. The pre-filter consists of eight fan-shaped annular segments made of aluminum on a polyimide film. The filter thicknesses measured by Luxel and the opening angles are summarized.

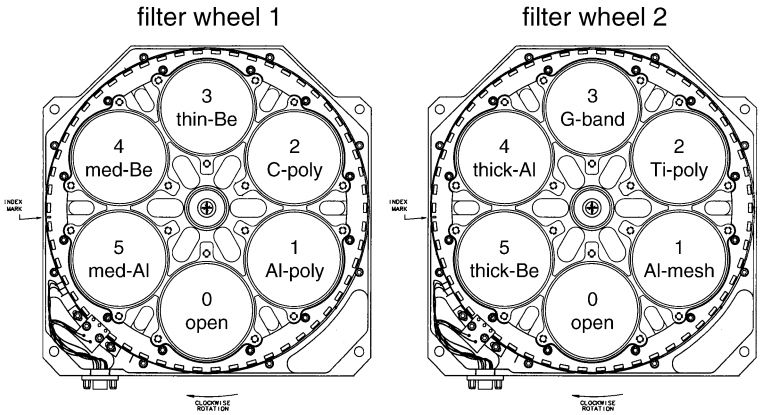

Figure 4 Filter wheels and focal-plane analysis filters. XRT has two filter wheels: Filter Wheels 1 and 2 (FW1 and FW2). Each filter wheel has six positions to mount the filters. Five X-ray analysis filters are mounted on FW1, and FW2 has four X-ray filters and one filter for visible-light observation (G-band). The position number and the name of the mounted filter are described in each filter position.

2.1. Optical Elements for X-rays

i) Pre-filter: The pre-filter consists of eight fan-shaped annular filter segments each made of thin aluminum on a polyimide film (Figure 3), which were manufactured by Luxel Corporation. The aperture shape was designed to obscure the locations of mirror-bonding pads to avoid possible degradation in image quality caused by surface deformation of the mirror at the bonding pads. In Figure 3, the aperture areas are shown in color with their respective opening angles. The average thickness of the entire pre-filter assembly is then given as $\sum(d \times \theta)/\sum\theta$, where d and θ are the thickness and opening

angle of each filter segment, respectively. The average pre-filter consists of 1538 Å Al and 2030 Å polyimide, based on measurement by the manufacturer.

ii) Mirrors: The M1 and M2 mirrors are grazing-incidence annular mirrors manufactured by Goodrich, each made of Zerodur. On the basis of measurements by the manufacturer, the annular entrance aperture of the XRT primary mirror is located between radii of $r_1 = 17.042446$ cm and $r_2 = 17.074051$ cm. Considering the open angle of pre-filter (242.04°, see Figure 3), the geometric aperture area of XRT is calculated to be $\pi \times (r_2^2 - r_1^2) \times (242.04/360) = 2.28$ cm^2. The grazing angle of X-rays at each XRT mirror is about 0.91° on average.

iii) Focal-plane analysis filters: XRT has two filter wheels: FW1 and FW2. Each filter wheel has six positions to mount focal-plane analysis filters (FPAFs). As shown in Figure 4, five X-ray analysis filters are mounted on FW1, and FW2 has four X-ray filters and one filter for visible-light observation (G-band). These nine X-ray filters are made of several kinds of metal and support, with different thicknesses, as summarized in Table 1. The filters are designed to observe the corona in a temperature range from less than 1 MK to more than 10 MK. Focal-plane analysis filters on FW1 and FW2 (hereafter FPAF1 and FPAF2, respectively) can be selected independently, even allowing combinations of filters both from FW1 and FW2 in series.

iv) CCD: X-rays are focused on a back-illuminated CCD (Kano *et al.*, 2008).

The effective area [$A_{\rm eff}$] of XRT is defined by the product of the geometric aperture area [A] and the efficiency of all of the optical elements:

$$A_{\rm eff} = A \times \mathcal{T}_{\rm PF} \times R_{\rm M1} \times R_{\rm M2} \times \mathcal{T}_{\rm FPAF1} \times \mathcal{T}_{\rm FPAF2} \times QE_{\rm CCD}, \quad (1)$$

where $\mathcal{T}_{\rm PF}$ is the transmission of the pre-filter, $R_{\rm M1}$ and $R_{\rm M2}$ the reflectivities at the primary and secondary mirrors, $\mathcal{T}_{\rm FPAF1}$ and $\mathcal{T}_{\rm FPAF2}$ the transmissions of FPAF1 and FPAF2, and $QE_{\rm CCD}$ the quantum efficiency of the CCD. Because each efficiency is a function of wavelength, $A_{\rm eff}$ is also a function of wavelength. In this article, we calibrate $\mathcal{T}_{\rm PF}$, $\mathcal{T}_{\rm FPAF1}$, and $\mathcal{T}_{\rm FPAF2}$, and then derive the effective area.

2.2. Optical Elements for G-band

When XRT takes visible-light images in G-band, the visible-light shutter is opened, and FW1 and FW2 are set to the open and G-band filter position, respectively. This G-band filter is a bandpass filter with a central wavelength of 4305.6 Å and a bandwidth of 172.8 Å (FWHM). The visible light is focused onto the same CCD as X-rays (Figure 2). X-rays cannot reach the CCD through the G-band (dotted line) or the X-ray (solid line) paths, because these X-rays are blocked by G-band filters employed at the front of the XRT and on FW2, respectively.

3. Overview of the Calibration

In Section 4 and the appendices, we will carefully calibrate the spectral response of XRT including the effect of the on-orbit contamination as accurately as possible. The on-orbit contamination makes our calibrations complicated. Therefore, before proceeding in detail, we first give an outline of the calibration activities in Figure 5.

In this figure, time passes from left to right. After the launch of *Hinode*, from the viewpoint of the XRT thermal environment, there are three distinct intervals: Phase 1 (22 September 2006 – 19 October 2006), Phase 2 (19 October 2006 – 18 June 2007), and Phase 3 (18

Table 1 Focal-plane analysis filters and pre-filter.

FW-pos[a]	Filter name	Pre-delivery measurements at Luxel[b]		Calibrated values in this article			
		Metal	Support	Pure metal	Oxidized	At fabrication[c]	Support
1-0	open	–	–	–	–	–	–
1-1	Al-poly	Al[d] 1283 Å (±50 Å)	poly[e] 2656 Å (±100 Å)	Al 1412 Å	Al_2O_3 75 Å	1470 Å	poly 2656 Å
1-2	C-poly	C[f] 6038 Å (±50 Å)	poly 3478 Å (±100 Å)	C 5190 Å	–	5190 Å	poly 3478 Å
1-3	thin-Be	Be[g] 9 µm (+5 µm)	–	Be 10.46 µm	BeO 150 Å	10.47 µm	–
1-4	med-Be	Be 30 µm (+5 µm /−2 µm)	–	Be 26.89 µm	BeO 150 Å	26.90 µm	–
1-5	med-Al	Al 12.5 µm (±5%)	–	Al 12.25 µm	Al_2O_3 150 Å	12.26 µm	–
2-0	open	–	–	–	–	–	–
2-1	Al-mesh	Al 1605 Å (±50 Å)	mesh[h]	Al 1583 Å	Al_2O_3 150 Å	1700 Å	77% trans. mesh
2-2	Ti-poly	Ti[i] 2345 Å (±50 Å)	poly 2522 Å (±100 Å)	Ti 2338 Å	TiO_2 75 Å	2380 Å	poly 2522 Å
2-3	G-band	Glass	–	–	–	–	–
2-4	thick-Al	Al 25 µm (±10%)	–	Al 26.09 µm	Al_2O_3 150 Å	26.1 µm	–
2-5	thick-Be	Be 300 µm (±30%)	–	Be 252.79 µm	BeO 150 Å	252.8 µm	–
	pre-filter	Al 1538 Å (±50 Å)	poly[e] 2030 Å (±100 Å)	Al 1492 Å	Al_2O_3 75 Å	1550 Å	poly 2030 Å

[a]"FW" and "pos" mean the filter wheel number and position on the filter wheel, respectively.

[b]These values are described in the certification sheet by Luxel. Note that the thicknesses measured by Luxel are only for reference.

[c]The expected metal thickness when it was fabricated. At fabrication, the metals had not oxidized at all. This value is derived from the calibrated thicknesses of pure and oxidized metal using Equation (56) in Appendix I. This is shown for comparison with the value measured by Luxel.

[d]"Al" means Aluminum.

[e]"poly" polyimide ($C_{22}H_{10}N_2O_5$).

[f]"C" Carbon.

[g]"Be" Beryllium.

[h]The mesh for Al-mesh filter is made of stainless steel.

[i]"Ti" Titanium.

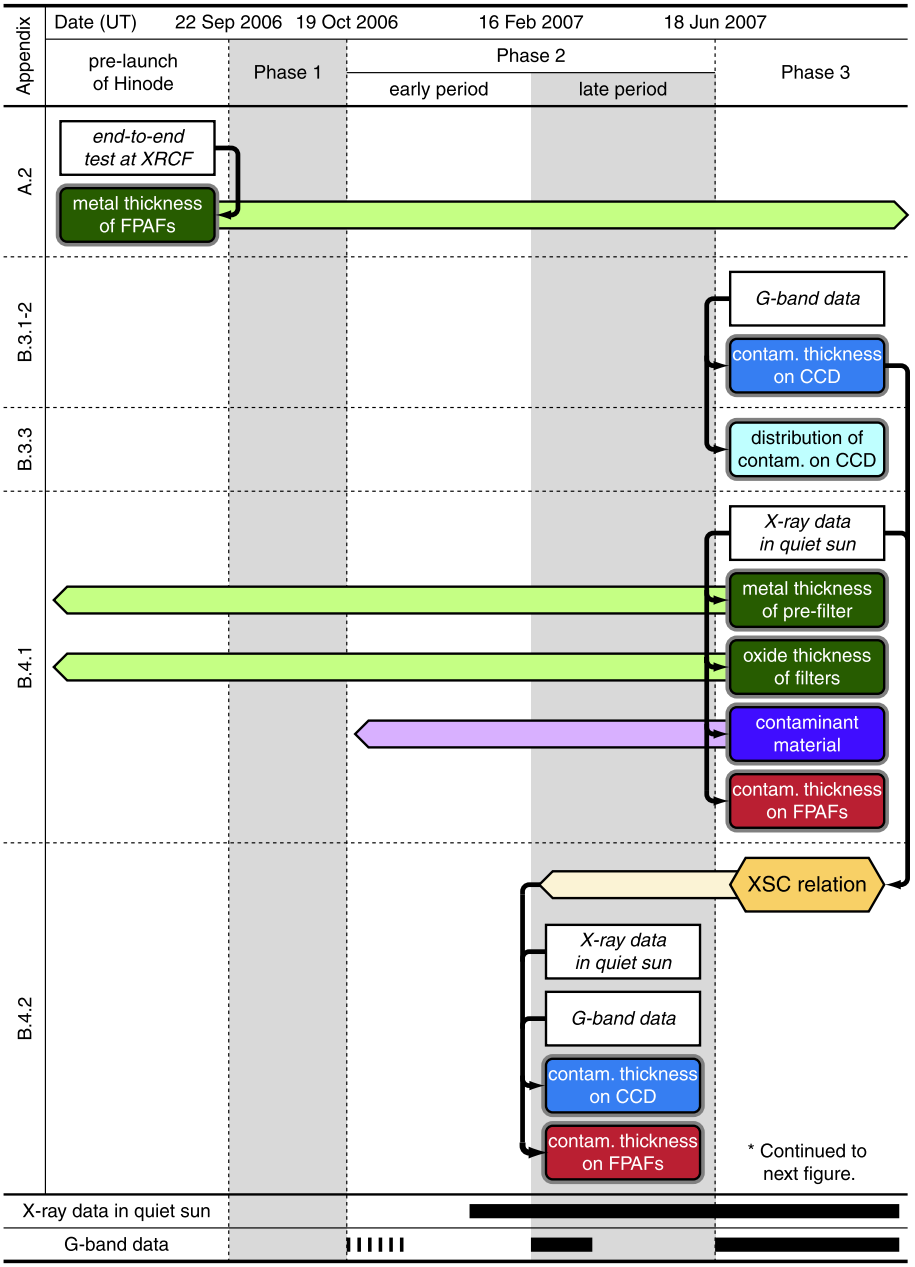

Figure 5 Outline of calibration activity for XRT.

June 2007 – present). Phase 1 is the period from launch to first light, when the CCD bakeout heater was kept on. Phases 2 and 3 are the periods of normal operation of XRT without and with enabling (turning on) of the operational heater, respectively. The details of each phase are described in Appendix B.1.

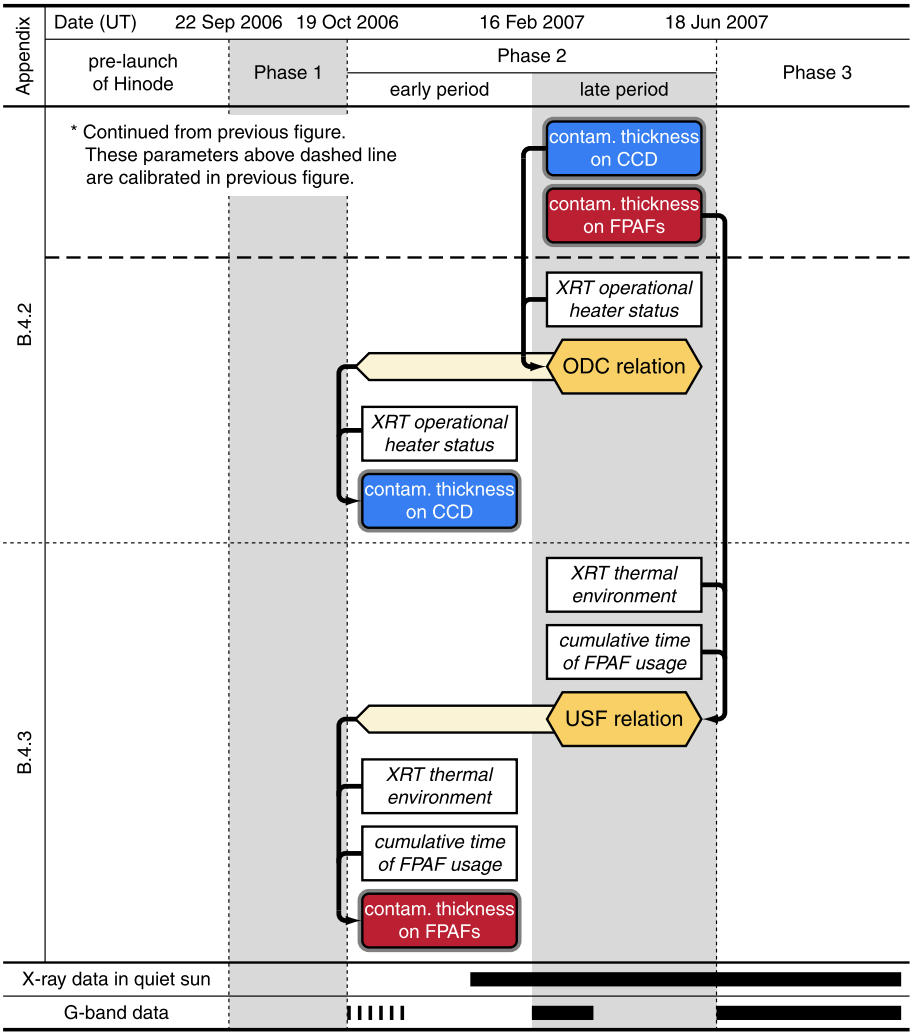

Figure 5 (*Continued.*)

At the bottom of Figure 5, the frequency of observations in X-rays and the G-band are shown by lines. The solid lines indicate that many data sets were taken, the dotted line are for the case of a few data sets, and no line signifies no data. From the viewpoint of this XRT observation, Phase 2 is divided into two periods, namely an early period (19 October 2006 – 16 February 2007) and a late period (16 February 2007 – 18 June 2007). In the early period, there are no simultaneous observations in X-rays and G-band, while in the late period, there are simultaneous observations.

The XRT calibrations were performed in order from top to bottom of the figure. The white boxes indicate the data sets used for our calibration. The black arrows connect the data sets or models to the calibrated results. The calibrated XRT instrumental parameters are shown by green boxes. The bars in light-green are extended from the green boxes to the times at which the calibrated results in the green boxes are valid. Note that the results shown

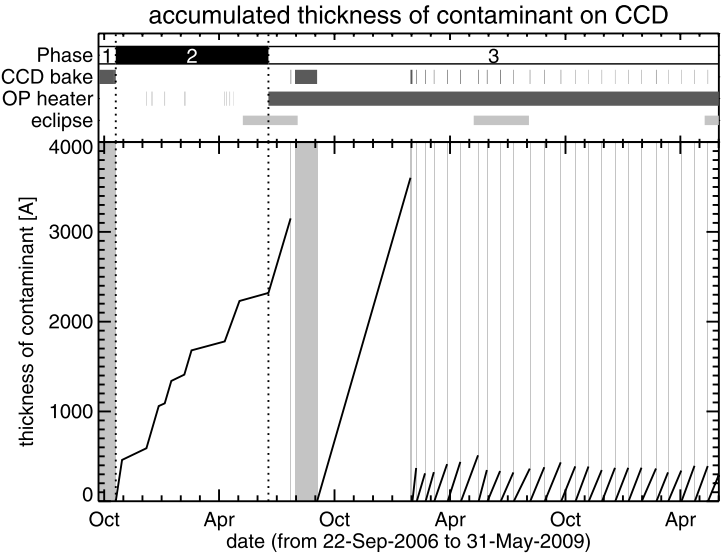

Figure 6 Calibrated thickness of contaminant accumulated on the CCD, with bakeouts indicated by gray vertical lines.

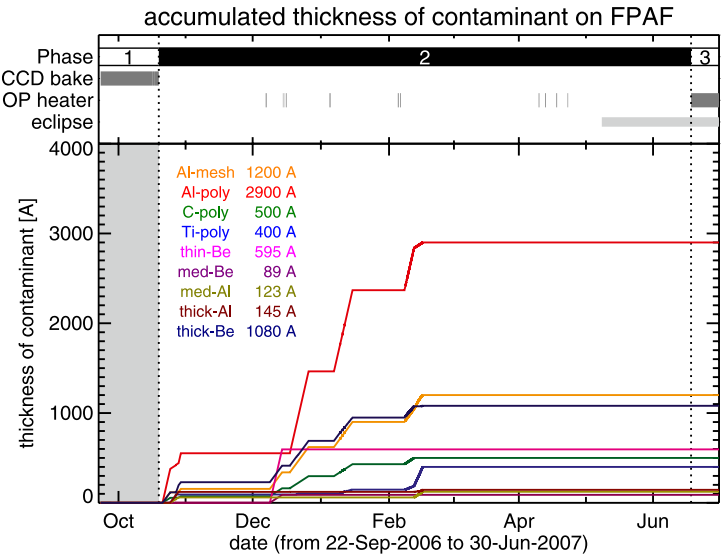

Figure 7 Calibrated thicknesses of contaminant accumulated on the FPAFs. The final thickness of contaminant on each FPAF is shown.

by green boxes and light-green bars are used for later calibration without indicating by black arrows. The blue and red boxes are the calibration results of contaminant accumulated on the CCD and FPAFs, respectively.

In Phase 3, since both X-ray and G-band data were taken sufficiently often (see bottom part of Figure 5), the calibrations of both the XRT instrument and contamination are

possible. However, in Phase 2 the data in X-rays and/or G-band were lacking for the calibration. In order to calibrate XRT for such intervals, we establish the three models shown in yellow boxes. For the late period of Phase 2, where G-band data are sparse, the model of the "XSC (X-ray-suggested CCD contamination) relation" based on the result of Phase 3 is used to calibrate the contaminant on both CCD and FPAFs, as shown by a bar in light-yellow. Meanwhile, for the early period of Phase 2 where the data are sparser than in the late period, two models – "ODC (operational heater driven contamination)" and "USF (FPAF-usage-suggested FPAF contamination)" relations – established in the late period are applied. In Phase 1, we expect that the contaminant did not accumulate on both CCD and FPAFs, because the CCD bake heater was kept on and the temperature around the FPAFs was high.

As shown in Figure 5, we calibrate the spectral response of XRT throughout its whole operation period. Table 1 summarizes the calibrated instrumental parameters of XRT with ground-based end-to-end test data (shown by green boxes in Figure 5). The details of this ground-based calibration are described in Appendix A. Time-varying thicknesses of on-orbit contaminant accumulated on the CCD (blue boxes) and FPAFs (red boxes) are given by Figures 6 and 7, respectively. The contaminant material is identified to have the chemical composition of a long-chain organic compound without silicon, a refractive index of ≈ 1.5, and a density of $\approx 1\ \mathrm{g\,cm^{-3}}$. In Section 4 and Appendix B, the on-orbit calibrations are described.

4. On-orbit Calibration

XRT took its first image on 23 October 2006. After this first light, XRT has been taking several thousand images a day. However, several months into the mission, we found that the X-ray intensity seen with XRT started to decrease continuously, especially using the thinner filters.

The top panel of Figure 8 shows the intensity [$\mathrm{DN\,sec^{-1}\ pixel^{-1}}$] of the quiet Sun in the four X-ray filters of XRT. In an intensity distribution (histogram) from a full-Sun corona, quiet-Sun areas manifest themselves as a concentration in the distribution whose profile is well expressed by a Gaussian. We took the center position of the Gaussian profile as representing the area-averaged quiet-Sun intensity. The orange, red, green, and blue pluses indicate the quiet-Sun intensity observed with the Al-mesh, Al-poly, C-poly, and Ti-poly filters, respectively. The gray area shows episodes of CCD bakeout (see Table 7 in Appendix C for details). The intensity decrease is seen in all filters, with that in the Al-mesh filter being most significant. While intensity fluctuations in the short-term (several weeks) are caused by solar activity such as the appearance of active regions, the systematic intensity decrease cannot be explained by solar activity. For example, the intensity of the quiet Sun with the Al-mesh, Al-poly, C-poly, and Ti-poly filters decreases to 27%, 59%, 80%, and 73%, respectively, during 142 days from 8 September 2007 to 28 January 2008. We conclude that the decrease is caused by accumulation of materials, namely contaminants, obscuring the optical path of the XRT.

The X-ray intensity ratio is a function of the XRT filter response and coronal temperature (see Equation (3)), and it is not affected by the variation of the coronal density nor the distance between the Sun and *Hinode* unlike the intensity. Since such an intensity ratio recovered to almost the same level following each CCD bakeout as seen in Phase 3 in the bottom panel of Figure 8, it is most likely that at least some fraction of the contaminants is accumulating on the CCD and each bakeout reduces the contaminant to the same thickness. The analysis of G-band intensity in Appendix B gives the result that this "same thickness"

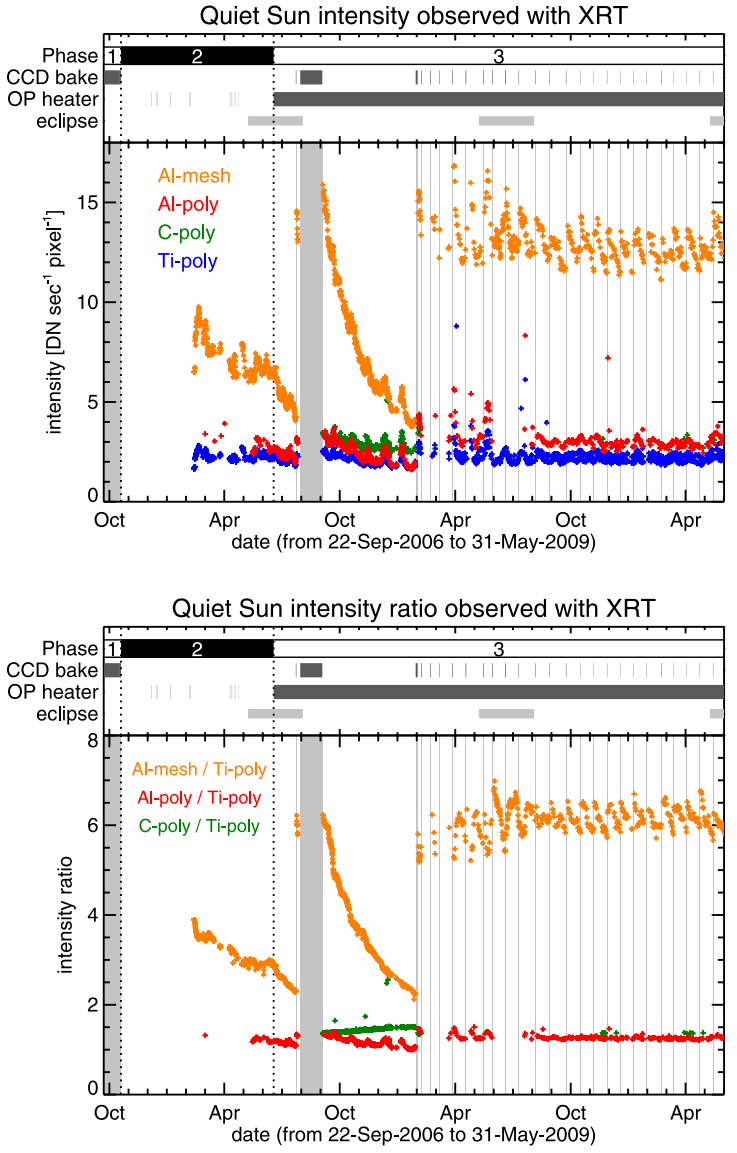

Figure 8 Intensity of the quiet Sun observed with XRT. Top panel: Original intensity of the quiet Sun observed with four kinds of X-ray filters. Bottom panel: Intensity ratio of the quiet Sun normalized with the intensity observed with Ti-poly filter. The gray area shows the duration of CCD bakeout.

Note – The information about the phase, which is defined in Appendix B.1, and the status of the bakeout heater and operational heater (gray bars mean that these heaters are on) are shown in the top part of these plots. *Hinode* has been placed in a Sun-synchronous polar orbit, that is, above the day – night line on Earth, where *Hinode* can continuously observe the Sun for 24 hours a day for about nine months per year. The remaining three months are called the "eclipse season", where the Sun is eclipsed by Earth for a maximum of 20 minutes in each 98-minute orbit. This eclipse season is indicated by light-gray bars.

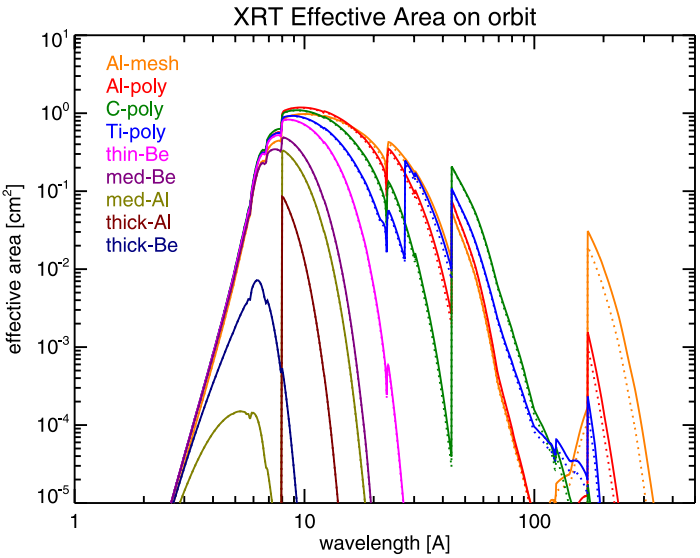

Figure 9 Effective area of XRT on orbit considering the contaminant accumulated on the FPAFs and CCD. The solid and dotted lines show the effective area just after CCD bakeout and one month after the bakeout in Phase 3, respectively. We assume that 800 Å of contaminant accumulated on the CCD one month after the bakeout.

is actually zero. Hence, we can say that each bakeout completely removes the contaminant from the CCD (except for the "spots" discussed in Appendix B). Details of the CCD bakeout are given in Appendix C.

We also find that the intensity of the quiet Sun taken with the Al-poly filter (red pluses) is weaker than with the C-poly filter (green pluses), as clearly seen in the period from September 2007 to February 2008 in the top panel of Figure 8. Strangely enough, however, the ground-based measurement at XRCF indicates that Al-poly filter should have a larger signal than the C-poly filter for all coronal temperatures (see the top panel of Figure 10). This discrepancy led us to the notion that, in addition to the CCD, the FPAFs also suffered from the accumulation of contaminants with different accumulated thickness for different filters.

Here, we briefly summarize how we characterized the material of the contaminant and the accumulation thicknesses on the CCD and FPAFs as a function of time. First, we measure the thickness of contaminant accumulated on the CCD using G-band data and a special method (see Appendix B.2 for details) as shown in Figure 6. Next, on the basis of the temporal evolution of the G-band and X-ray intensities, we identify the material of the contaminant as being of the chemical composition of a long-chain organic compound without silicon, with a refractive index of ≈ 1.5, and a density of $\approx 1\ \mathrm{g\,cm^{-3}}$. The thickness of the pre-filter, oxidization thickness of the pre-filter and FPAFs, and the thickness of contaminants accumulated on each FPAF are also calibrated (see Appendix B.3 for details), as summarized in Table 1 and Figure 7. Table 2 shows a summary of the on-orbit contamination behavior.

Since we now have accurate knowledge of the response parameters (filter thicknesses, contaminant thicknesses, *etc.*) at every epoch after launch of *Hinode*, we can accurately derive the XRT effective area and the temperature response. (The temperature response is explained in detail in Appendix D.2.) The calibrated effective area and temperature response

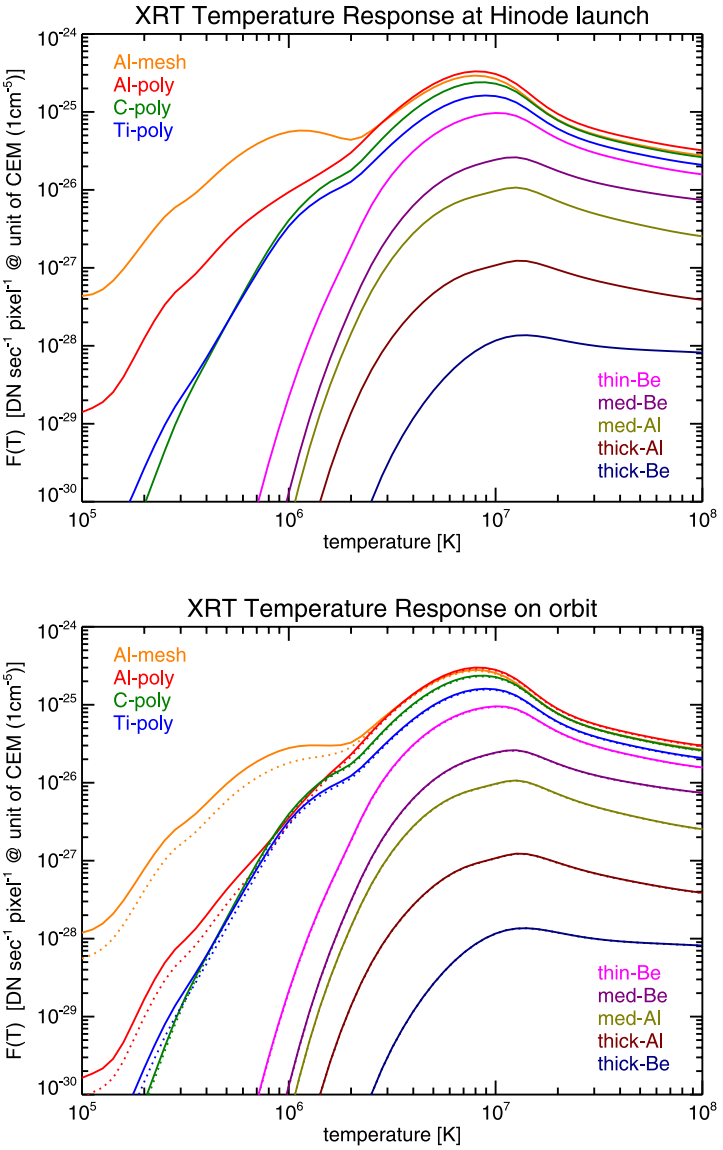

Figure 10 Top panel: Response of XRT to the coronal temperature at the launch of *Hinode*, *i.e.* when XRT had not been contaminated. Bottom panel: Response of XRT to coronal temperature on orbit considering the contaminant accumulated on the FPAFs and CCD. The solid and dotted lines in the bottom panel show the temperature response just after CCD bakeout and one month after the bakeout in Phase 3, respectively. We assume that 800 Å of contaminant accumulated on the CCD one month after the bakeout.

are shown in Figures 9 and 10, respectively. Let us next look into the temperature-diagnostic capability of XRT with the calibrated temperature response.

Table 2 Behavior of contamination.

Period[a]	Bake heater	Operational heater	Eclipse season	Contamination[b]	
				On CCD	On FPAFs
Phase 1	ON	OFF	no	none	none
Normal Phase 2	OFF	OFF	N/A	↗	⟶
CCP in Phase 2	OFF	ON→OFF	no	↗↗↗	↗↗↗
WCP in Phase 2	OFF	ON→OFF	close to	↗↗↗	⟶
Phase 3	OFF	ON	N/A	↗↗↗	⟶
CCD bakeout	ON	N/A	N/A	completely removed	⟶

[a]Phases 1 – 3 are defined in Appendix B.1. CCP and WCP represent the "cool contamination periods" and "warm contamination period" defined in Appendix B.3.3, respectively.

[b]"↗↗↗" and "↗" indicate the rapid and slow accumulation of contaminant, respectively. "⟶" means that the thickness of the contaminant is stable.

5. Temperature Diagnostics with Filter-Ratio Method

The coronal-temperature-diagnostic capability is the most significant scientific attribute of XRT. In Section 5.1, we explain the coronal-temperature diagnostics with the filter-ratio method and the estimate of statistical errors in the derived temperature due to photon noise for the XRT. The filter-ratio method derives a mean temperature weighted by the filter responses and emission measure from images observed with two different filters (Vaiana, Krieger, and Timothy, 1973). Hara *et al.* (1992) and Kano and Tsuneta (1995) discussed coronal-temperature diagnostics and statistical errors for the *Soft X-ray Telescope* (SXT) onboard *Yohkoh* (*Solar-A*: Tsuneta *et al.*, 1991), respectively. In Section 5.2, we summarize the suitable filter pairs of XRT for coronal-temperature diagnostics with the filter-ratio method. In Section 5.3, we discuss the meaning of the filter-ratio temperature as derived with XRT.

5.1. Filter-Ratio Method

Assuming that the corona is isothermal, the data number [DN] observed with XRT is

$$\mathrm{DN} = \frac{F(T)}{S} \times \mathrm{VEM} \times t \tag{2}$$

for an isothermal corona at a temperature of T, where $F(T)$, VEM, t, and S are the XRT temperature response, volume emission measure, exposure time, and solar area detected in 1 pixel of CCD ($\approx 560\,000$ km^2 derived from a plate scale of XRT ≈ 1.03 arcsec pixel^{-1} (Shimizu *et al.*, 2007) and the relation of 1 arcsec ≈ 726 km arcsec^{-1} on the solar surface), respectively. Then, the ratio $[R_{ij}(T)]$ of normalized DNs per unit time taken with two different filters is a function of only the coronal temperature $[T]$:

$$R_{ij}(T) \equiv \frac{\mathrm{DN}_i/t_i}{\mathrm{DN}_j/t_j} = \frac{F_i(T)/S \times \mathrm{VEM}}{F_j(T)/S \times \mathrm{VEM}} = \frac{F_i(T)}{F_j(T)}. \tag{3}$$

The subscripts i and j specify the two different filters.

The coronal temperature can be estimated with the observed ratio of normalized DNs as

$$T = R_{ij}^{-1}\left(\frac{\mathrm{DN}_i/t_i}{\mathrm{DN}_j/t_j}\right), \tag{4}$$

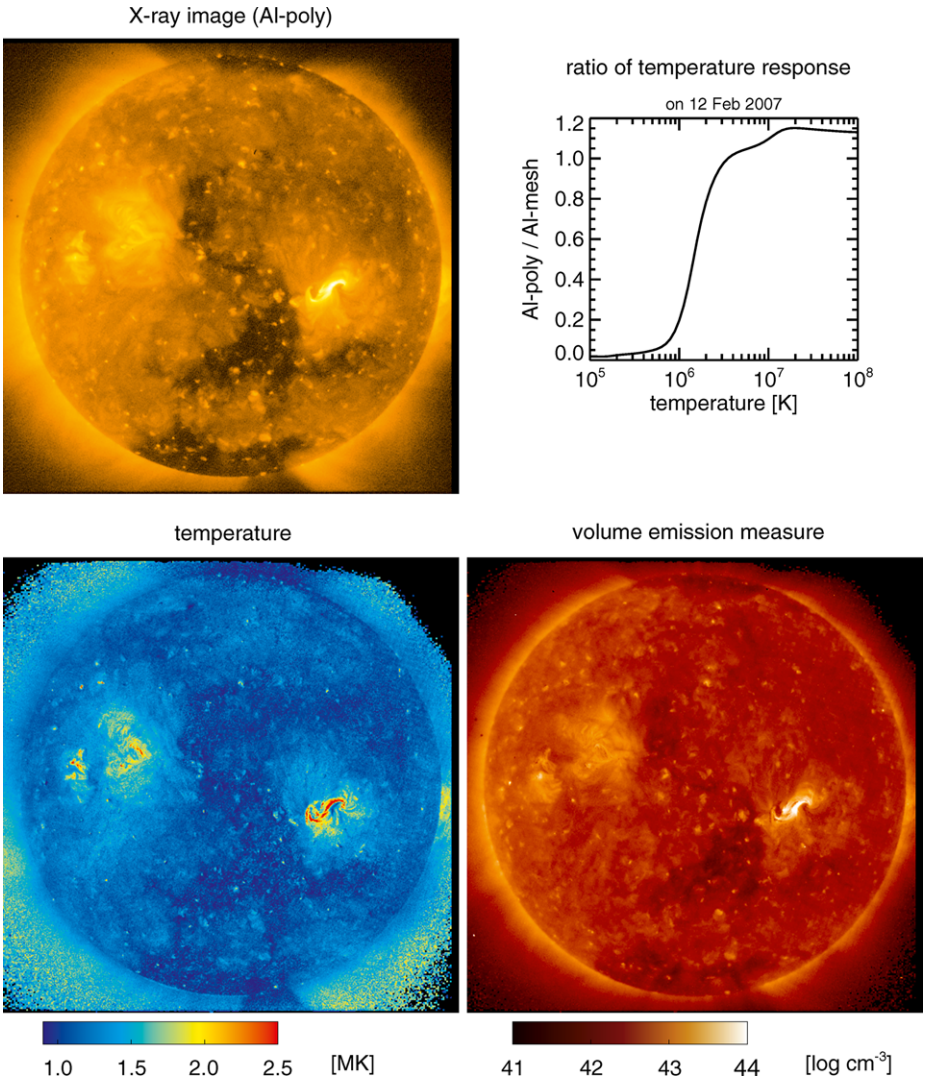

Figure 11 Example of the XRT temperature diagnostics with the filter-ratio method applied to full-disk images taken with Al-mesh and Al-poly filters on 12 February 2007. Top-left panel: the original X-ray data taken with Al-poly filter. Top-right panel: the ratio of temperature response between Al-poly and Al-mesh filters. Bottom-left panel: the full-Sun temperature. Bottom-right panel: the volume emission measure.

where R_{ij}^{-1} is the inverse of R_{ij}. Once the coronal temperature is obtained, we can derive the volume emission measure

$$\mathrm{VEM} \equiv \int n_\mathrm{e} n_\mathrm{H}\, \mathrm{d}l\, \mathrm{d}S = \frac{\mathrm{DN}_i / t_i}{F_i / S} \text{ or } \frac{\mathrm{DN}_j / t_j}{F_j / S}, \tag{5}$$

where n_e, n_H, and $\mathrm{d}l$ are the electron number density [cm^{-3}], the hydrogen number density [cm^{-3}], and the unit length along the line-of-sight [cm], respectively. Figure 11 is an example of the coronal-temperature diagnostics with the filter-ratio method applied to XRT data

taken with Al-mesh and Al-poly filters on 12 February 2007. The bottom-left and bottom-right panels are the full-Sun temperature and emission-measure maps, respectively.

Next, we discuss the estimate of the statistical errors in the derived temperature and emission measure due to Poisson noise of incident photons into XRT. Since Poisson noise of incident photons dominates over other noise sources (*e.g.*, the camera system noise and dark-current noise reported by Kano *et al.* (2008)), we consider only Poisson noise for the error estimate. Note that Kano and Tsuneta (1995) estimated those errors for *Yohkoh*/SXT. The differences between our estimate and that of Kano and Tsuneta (1995) are the adopted solar spectrum database and its units. We adopt solar photon-number spectra in units of photon $\mathrm{cm}^{-2}\,\mathrm{sec}^{-1}\,\mathrm{sr}^{-1}\,\text{Å}^{-1}$ from the CHIANTI atomic database version 6.0.1 (Dere *et al.*, 1997, 2009, which was the latest version when we were analyzing) with ionization equilibrium from chianti.ioneq (Dere, 2007) and abundance from sun_coronal_ext.abund (Feldman *et al.*, 1992; Landi, Feldman, and Dere, 2002), while Kano and Tsuneta (1995) used solar emissivity [$\mathrm{erg}\,\mathrm{cm}^{-2}\,\mathrm{sec}^{-1}\,\mathrm{sr}^{-1}\,\text{Å}^{-1}$] from Mewe's spectral data (Mewe, Gronenschild, and van den Oord, 1985; Mewe, Lemen, and van den Oord, 1985).

First, we derive two conversion factors as preparation for the error estimate. When XRT observes an isothermal corona at a temperature of T and a volume emission measure of VEM with p pixels of the CCD and t [sec] exposure, the incident photon number in the range of wavelength from λ to $\lambda + \mathrm{d}\lambda$ is

$$\mathrm{d}N = \left(\tilde{P}_{\mathrm{iso}\odot}(\lambda, T) \times s \times \frac{A_{\mathrm{eff}}(\lambda)}{f^2} \times \mathrm{d}\lambda \right) \times \frac{t}{S} \times \mathrm{VEM}, \tag{6}$$

where $\tilde{P}_{\mathrm{iso}\odot}(\lambda, T)$ [$\mathrm{cm}^{-2}\,\mathrm{sec}^{-1}\,\mathrm{sr}^{-1}\,\text{Å}^{-1}$] is the photon-number spectrum emitted from an isothermal corona at a temperature of T and a unit of column emission measure (CEM) of 1 cm^{-5}, s is the area of one CCD pixel (13.5^2 μm^2; see Kano *et al.* (2008)), $A_{\mathrm{eff}}(\lambda)$ is the effective area of XRT, and f is the focal length of XRT (2708 mm; see Golub *et al.* (2007)). The total photon number observed with XRT is, then,

$$N = \int \mathrm{d}N. \tag{7}$$

The data number (DN) observed with XRT is derived as

$$\mathrm{DN}(T) = \int \left(\tilde{P}_{\mathrm{iso}\odot}(\lambda, T) \times s \times \frac{A_{\mathrm{eff}}(\lambda)}{f^2} \times \frac{hc}{\lambda} \times \frac{1}{e \times 3.65 \times G} \right) \mathrm{d}\lambda \times \frac{t}{S} \times \mathrm{VEM} \tag{8}$$

(from Equations (2) and (39) in Appendix D.2), where h, c, e, and G are Planck's constant, the speed of light, the elementary electric charge, and the system gain of the CCD camera, which is 57.5 [electron DN^{-1}] for XRT (Kano *et al.*, 2008), respectively. When we define $K^{(1)}(T)$ as

$$K^{(1)}(T) \equiv \frac{\int \tilde{P}_{\mathrm{iso}\odot}(\lambda, T) \times A_{\mathrm{eff}}(\lambda) \times \frac{hc}{\lambda} \times \frac{1}{e \times 3.65 \times G}\,\mathrm{d}\lambda}{\int \tilde{P}_{\mathrm{iso}\odot}(\lambda, T) \times A_{\mathrm{eff}}(\lambda)\,\mathrm{d}\lambda}, \tag{9}$$

we can rewrite Equation (7) as

$$N = \frac{\mathrm{DN}}{K^{(1)}(T)}. \tag{10}$$

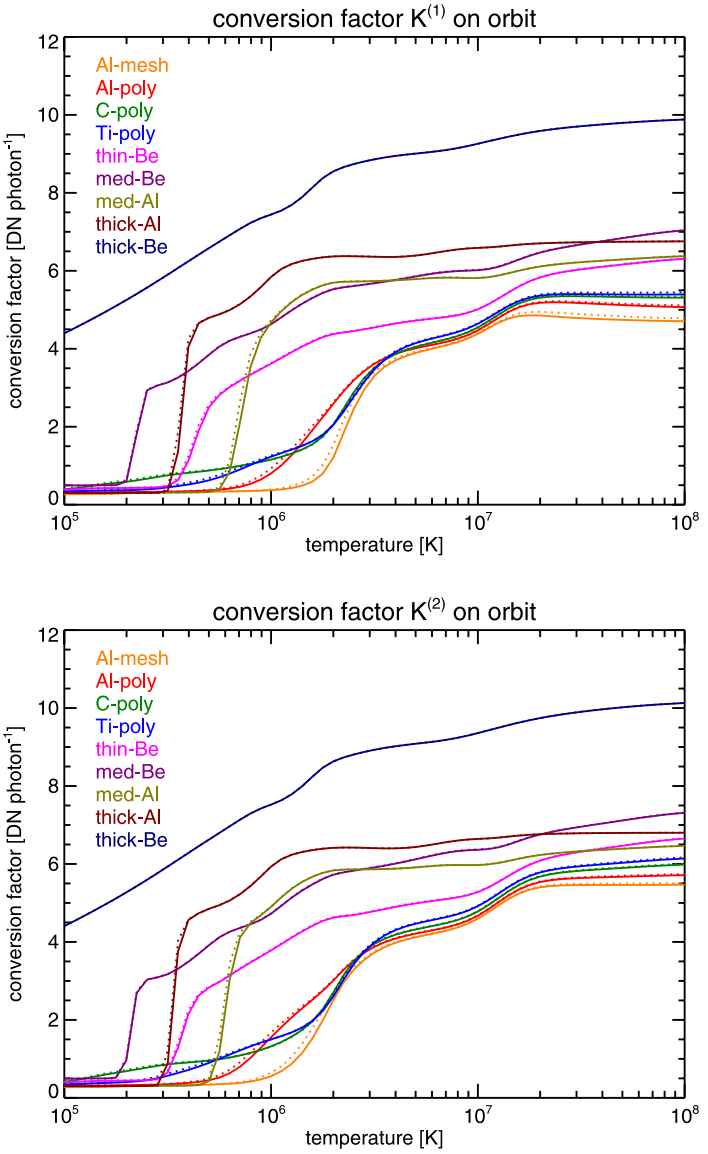

Figure 12 Top panel: Conversion factor $[K^{(1)}(T)]$ of each FPAF from observed data number (DN) to incident photon number $[N]$, namely $N = \mathrm{DN}/K^{(1)}(T)$. Bottom panel: Conversion factor $[K^{(2)}(T)]$ of each FPAF from observed DN to the square of DN error $[\sigma_{\mathrm{DN}}]$, namely $\sigma^2_{\mathrm{DN}} = K^{(2)}(T) \times \mathrm{DN}$. These figures show the conversion factors on orbit considering the contaminant accumulated on the FPAFs and CCD, where the solid and dotted lines indicate the conversion factors just after CCD bakeout and one month after the bakeout in Phase 3, respectively. We assume that 800 Å of contaminant accumulated on the CCD one month after the bakeout.

$K^{(1)}(T)$ is the conversion factor from observed DN to incident photon number. The top panel of Figure 12 shows $K^{(1)}(T)$ for each filter.

Table 3 Typical values of coronal structures.

Coronal structure	DEM reference	Electron number density	Exposure time	Binning size
Flare	Dere and Cook (1979)	$10^{11.0}$ cm^{-3}	1 sec	1×1
Active region	Warren, Brooks, and Winebarger (2011)	$10^{9.4}$ cm^{-3}	10 sec	2×2
Quiet Sun	Brooks and Warren (2006)	$10^{8.3}$ cm^{-3}	30 sec	4×4
Coronal hole	Vernazza and Reeves (1978)	$10^{8.0}$ cm^{-3}	64 sec	8×8

Since dN follows a Poisson distribution, the standard deviation dσ of dN is expressed as

$$\mathrm{d}\sigma = \sqrt{\mathrm{d}N}. \tag{11}$$

Since Equation (8) is rewritten as

$$\mathrm{DN} = \int \left(\frac{hc}{\lambda} \times \frac{1}{e \times 3.65 \times G} \right) \mathrm{d}N, \tag{12}$$

we can derive the error [σ_{DN}] of DN as

$$\sigma_{\mathrm{DN}} = \sqrt{\int \left(\frac{hc}{\lambda} \times \frac{1}{e \times 3.65 \times G} \right)^2 (\mathrm{d}\sigma)^2} = \sqrt{K^{(2)}(T)\mathrm{DN}}, \tag{13}$$

where

$$K^{(2)}(T) \equiv \frac{\int \tilde{P}_{\mathrm{iso}\odot}(\lambda, T) \times A_{\mathrm{eff}}(\lambda) \times \left(\frac{hc}{\lambda} \times \frac{1}{e \times 3.65 \times G} \right)^2 \mathrm{d}\lambda}{\int \tilde{P}_{\mathrm{iso}\odot}(\lambda, T) \times A_{\mathrm{eff}}(\lambda) \times \frac{hc}{\lambda} \times \frac{1}{e \times 3.65 \times G} \, \mathrm{d}\lambda}. \tag{14}$$

$K^{(2)}(T)$ is a conversion factor from observed DN to the square of the DN error. The bottom panel of Figure 12 shows $K^{(2)}(T)$ for each filter.

We note that these two conversion factors [$K^{(1)}$ and $K^{(2)}$] vary in the part of detectable temperature range of XRT from $\approx$1 MK to $\approx$5 MK (see Figure 12), while those factors for *Yohkoh*/SXT were almost constant at three throughout the whole detectable temperature range of $\approx$2 MK to $>$ 10 MK (Kano and Tsuneta, 1995).

Following the appendix of Kano and Tsuneta (1995), we can estimate the error of derived temperature and volume emission measure from these conversion factors as

$$\frac{\sigma_T}{T} = \left| \frac{\mathrm{d} \ln R_{ij}(T)}{\mathrm{d} \ln T} \right|^{-1} \sqrt{\frac{K_i^{(2)}(T)}{\mathrm{DN}_i} + \frac{K_j^{(2)}(T)}{\mathrm{DN}_j}} \tag{15}$$

and

$$\frac{\sigma_{\mathrm{VEM}}}{\mathrm{VEM}} = \left| \frac{\mathrm{d} \ln R_{ij}(T)}{\mathrm{d} \ln T} \right|^{-1} \sqrt{\left[\frac{\mathrm{d} \ln F_j(T)}{\mathrm{d} \ln T} \right]^2 \frac{K_i^{(2)}(T)}{\mathrm{DN}_i} + \left[\frac{\mathrm{d} \ln F_i(T)}{\mathrm{d} \ln T} \right]^2 \frac{K_j^{(2)}(T)}{\mathrm{DN}_j}}. \tag{16}$$

These relations show how the errors in observed data number [DN] propagate to the errors in the derived temperature [T] and volume emission measure [VEM].

We note that the temperature in the right-hand side of Equations (15) and (16) should be the actual temperature of the coronal plasma. However, we get the estimated coronal

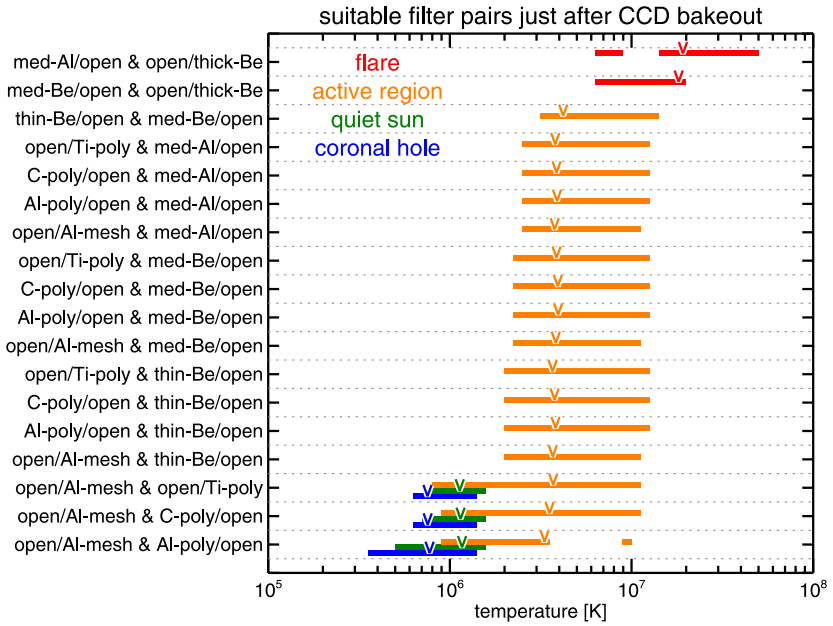

Figure 13 Suitable filter pairs to derive the temperature with the filter-ratio method and their useful temperature ranges just after the CCD bakeout in Phase 3; namely, there is no contamination on the CCD but the contaminant accumulated on the FPAFs. The red, orange, green, and blue bars show the useful temperature ranges for flare, active region, quiet Sun, and coronal hole, respectively. The "v" marks indicate the filter-ratio temperatures derived from the DEMs of each region.

temperature with the filter-ratio method. Hence, we used the derived temperature to estimate the errors instead of the actual temperature. In the case of poor signal-to-noise ratio (S/N) data, the difference between actual and derived temperatures may be larger than in the case of good S/N data, and the above treatment of T in the error estimate will cause the additional error. We confirmed that 10% S/N data makes this additional error sufficiently small.

On the basis of the error estimate discussed above, the full-Sun temperature map in Figure 11 was created. In this map, the poor S/N pixels, namely pixels in the coronal hole and quiet Sun, are summed (8×8 pixels binning maximum) to improve the S/N. Using these good S/N data, the coronal temperature with the filter-ratio method can be derived with less than 20% errors across the Sun. This diagnostic capability is the most significant scientific feature of XRT.

5.2. Suitable Filter Pairs for Coronal-Temperature Diagnostics with the Filter-Ratio Method

On the basis of the discussion in the previous section, we present suitable filter pairs to derive temperatures with filter-ratio method for various coronal structures: flares, active regions, quiet Sun, and coronal holes. The typical values for each coronal structure are summarized in Table 3. The electron number density is calculated as the integral over temperature of the DEM with the assumption that the line-of-sight depth is 10^5 km. The exposure time and binning size is determined from the time scale and spatial scale of each structure, respectively. Figures 13 and 14 show the "suitable filter pairs" and their "useful temperature ranges" for

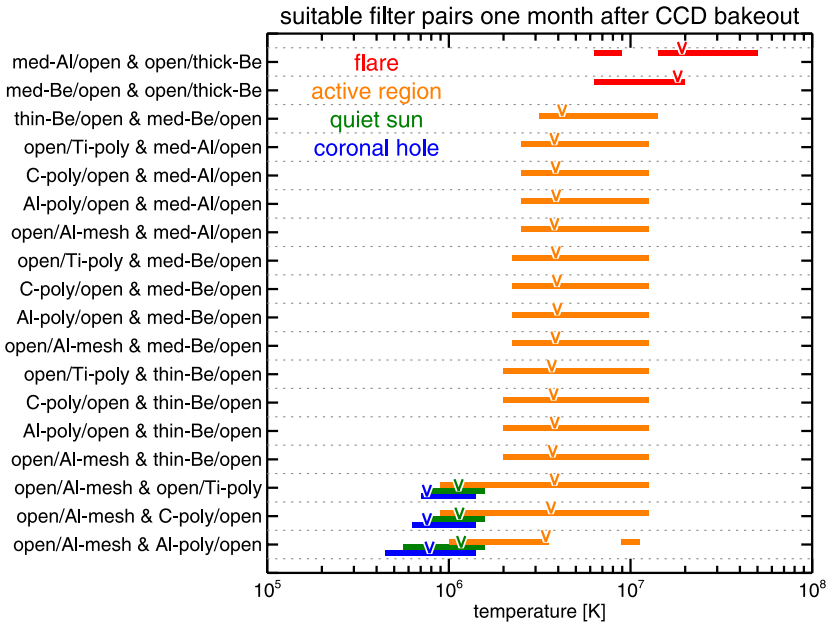

Figure 14 Suitable filter pairs to derive the temperature with the filter-ratio method and their useful temperature ranges one month after the CCD bakeout in Phase 3, namely there is contamination not only on the FPAFs but also on the CCD. We assume that 800 Å of contaminant accumulated on the CCD. The others are the same as in Figure 13.

some representative cases of contamination accumulated on the CCD and the FPAFs. The "useful temperature range" means the range where a filter pair can estimate the temperature (within 20% accuracy) with the filter-ratio method for a given coronal structure with the typical exposure time and binning size (see Table 3). The "suitable filter pair" means that the pair has a wide "useful temperature range" as shown in Figures 13 and 14. For example, the Al-mesh and Ti-poly filter pair can have a wide temperature coverage for a wide variety of coronal structures, coronal holes, quiet Sun, and active regions. Thus, this pair is suitable for full-disk synoptic observations.

Let us now examine how to derive the suitable filter pairs and their useful temperature ranges. Figures 15 and 16 are examples of the filter-pair study for quiet Sun and active region, respectively. A summary of the study is described in the top-left of these figures. Here [target] indicates the coronal structure to be analyzed. The typical differential emission measure (DEM) of such a target is plotted in the top-right side of these figures (the references of typical DEMs are summarized in Table 3). The row with [binning size] is the recommended binning size to collect enough photons. For a bright flare, [binning size] is 1×1 binning, that is, there is no binning. Meanwhile, for the dark coronal hole, [binning size] is 8×8 binning. The binning size used in our calculation is shown in Table 3. The rows with [filter1] and [filter2] summarize the evaluated filter pair. Labels "fw1" and "fw2" indicate used FPAFs on Filter Wheels 1 and 2, respectively. The label "contam." gives the accumulated thickness of contaminant on each FPAF. The label "full-well exp. time" expresses the exposure time necessary to obtain the full-well intensity of the XRT CCD, about 200 000 electrons $\approx$ 3500 DN, when XRT observes the coronal structure shown in [target] with [filter1] or [filter2]. The full-well intensity means the maximum intensity to keep the linearity between

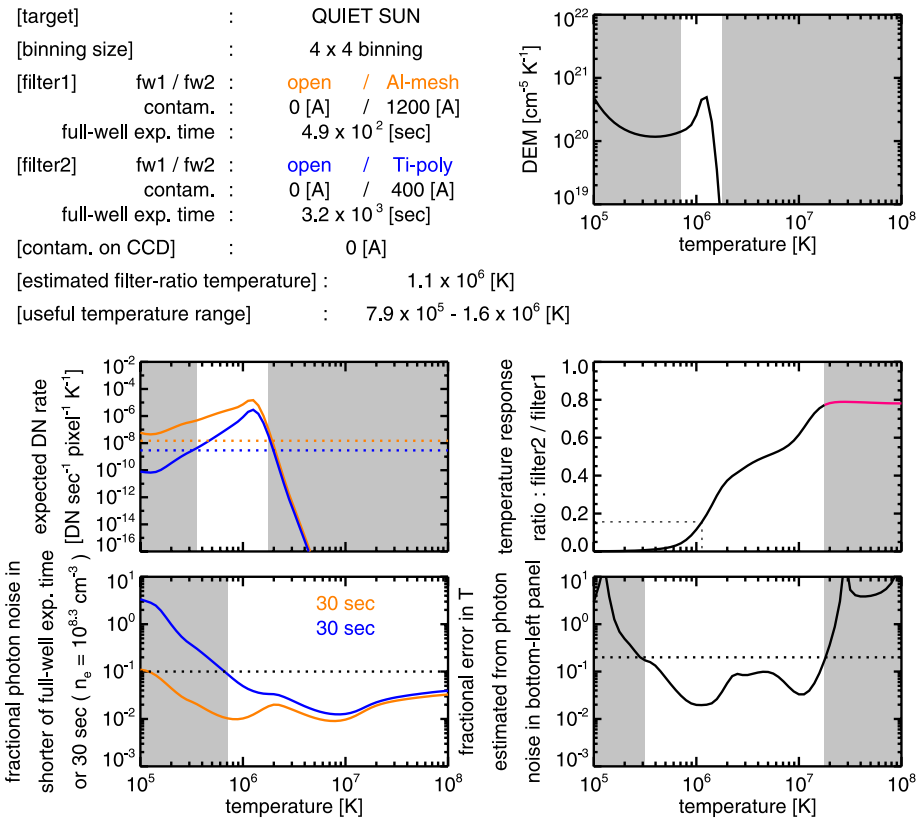

Figure 15 Evaluation of the Al-mesh and Ti-poly filter pair for coronal-temperature diagnostics with the filter-ratio method. This is the case of the quiet Sun just after the CCD bakeout in Phase 3. This pair is suitable for temperature diagnostics in the quiet Sun.

the incident photon energy and output intensity as shown by Equation (33). In the case of the intensity exceeding the full-well intensity, the actual output intensity becomes smaller than the intensity expected from Equation (33). The row with [contam. on CCD] indicates the accumulated thickness of contaminant on the CCD.

Next, we explain six conditions for a filter pair shown in [filter1] and [filter2] to be suitable for the temperature diagnostics with the filter-ratio method. The six conditions, (A) – (F), are given below. The four panels at the bottom part of Figures 15 and 16 show the temperature ranges (white areas) that satisfy the Conditions (A) – (D), as described next.

(A) Expected DN rate at each temperature:
The middle-left panel shows the expected DN rates (whose units are $\mathrm{DN\,sec^{-1}\,pixel^{-1}\,K^{-1}}$) at each temperature when XRT with [filter1] and [filter2] observes the [target] which has the DEM shown in the top-right side of the figures. Since the dynamic range of the XRT CCD is about 1000, we assume that XRT can detect temperature components where the DN rate is exceeding 1/1000 of the peak DN rate in each expected DN rate plot. Condition (A) is that the expected DN rate exceeds 1/1000 of the peak DN rate (shown by dotted lines) in the two cases of [filter1] and [filter2].

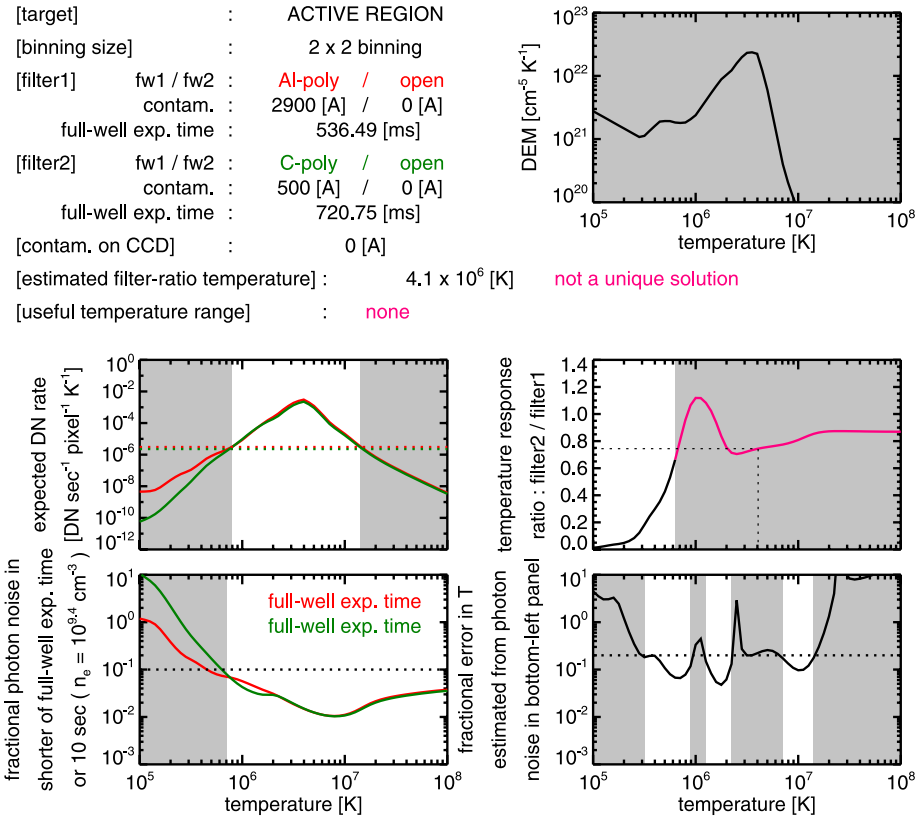

Figure 16 Evaluation of the Al-poly and C-poly filter pair for coronal-temperature diagnostics with the filter-ratio method. This is the case of the active region just after the CCD bakeout in Phase 3. This pair is not suitable for temperature diagnostics in the active region.

(B) Low photon noise:
The bottom-left panel presents the photon noise, when XRT observes an isothermal plasma at each temperature given by the horizontal axis of the panel. The electron number density at each temperature is set to have a constant value as the typical value described in Table 3 and vertical axis. Hence, this plot shows how much photon noise is expected in the observed data when we obtain the filter-ratio temperature from such data. The photon noise can be calculated with Equation (13) as a function of temperature and DN. The DN is derived from temperature, VEM, and exposure time as shown in Equation (2). For the calculation of VEM, we use the above electron number density and 10^5 km as the line-of-sight length. The effect of binning is also considered. The exposure time adopted for this evaluation is the shorter of the typical exposure time (see Table 3) or the exposure time to obtain the full-well intensity (see the label "full-well exp. time"). The adopted exposure time for each filter is described in each filter color in the bottom-left panel. The horizontal dotted line corresponds to 10% photon noise (S/N = 10). We consider that good S/N data (S/N > 10) should be used for the temperature diagnostics, because poor S/N data make the error large as mentioned above. Condition (B) is that the photon noise should be lower than 10%. We note that Condition (B)

is not so strict, because we can adequately sum many images to have enough photons. When we collect enough photons with a single image, Condition (B) should be satisfied.

(C) Profile of temperature-response ratio:
The middle-right panel indicates the temperature response ratio of [filter1] and [filter2] shown by Equation (3). Using this ratio, we can estimate the coronal temperature from the observed intensity ratio. The horizontal dashed lines in Figures 15 and 16 show the expected intensity ratio, when XRT observes [target] with [filter1] and [filter2]. In the case of Figure 15, the temperature is uniquely derived as shown by the vertical dashed line. The derived temperature is described by [estimated filter-ratio temperature] in the top-left panel of the figure. However, in the case of Figure 16, the temperature cannot be uniquely determined. In this case, [estimated filter-ratio temperature] shows the closest temperature to the peak temperature of DEM in the top-right panel as a reference. The temperature range where the intensity ratio gives the alternative temperatures is indicated by the magenta line and a gray area. Condition (C) is that the temperature is derived uniquely from the filter-ratio method.

(D) Error in estimated temperature:
The bottom-right panel shows the fractional error in estimated temperature caused by 10% photon noise. The error in the estimated temperature is calculated with Equation (15) as a function of temperature and DN. The DN is derived with the method described in Condition (B). We take an estimate error of 20%, which is twice the value of the photon noise, as the threshold for a reasonable temperature estimate. This is Condition (D). The horizontal dotted line is located at the 20% error in estimated temperature.

(E) No saturation:
The shortest exposure time for XRT is 1 ms. Hence, the "full-well exp. time" should be longer than 1 ms. For bright coronal structures, namely active regions and flares, the suitable filter pairs are limited by this condition.

(F) Filter-ratio temperature:
The useful temperature range with the filter-ratio method is derived from satisfying Conditions (A) – (E) as shown by [useful temperature range] and in the white area in the top-right DEM panel. We call the filter pair suitable if the [estimated filter-ratio temperature] falls within this [useful temperature range]. This is Condition (F).

The suitable filter pairs for coronal-temperature diagnostics with the filter-ratio method should satisfy all of the Conditions (A) – (F). These suitable filter pairs depend on the target, filter pair, and accumulation of the contaminant. Examples are summarized in Figures 13 and 14 for some representative cases of contamination accumulated on the CCD and the FPAFs with their [useful temperature range] and [estimated filter-ratio temperature] shown by bars and "v" marks, respectively. These suitable filter pairs and their useful temperature range are useful for understanding the temperature-diagnostic capability of XRT and for making the XRT observation plan for temperature analysis. In the analysis with actual data taken with XRT, it is also possible to estimate the temperature with filter pairs other than those that we described here as suitable filter pairs, since the suitable filter pairs are derived with the typical values of coronal structures (DEMs, density, and binning size) summarized in Table 3.

We note that, since the actual solar corona may have a multi-temperature structures, the photon noise for Condition (B) should be estimated with a multi-temperature (DEM). However, we consider that the treatment in Condition (B) is valid, since we confirmed that the photon noise derived with the filter-ratio temperature well represents one derived with DEM, at least at the estimated filter-ratio temperature, as will be discussed in Appendix J. In

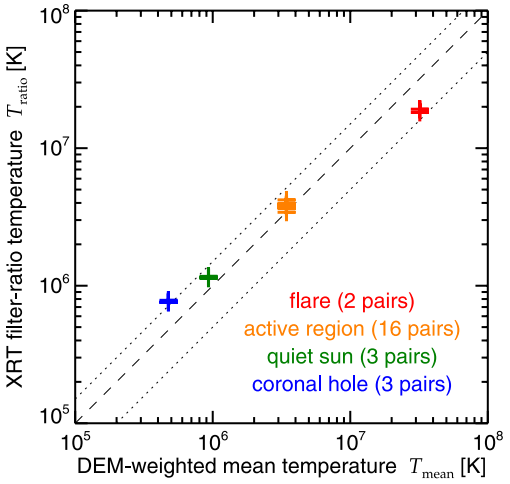

Figure 17 Correlation between DEM-weighted mean temperature [$T_{\rm mean}$] and XRT filter-ratio temperature [$T_{\rm ratio}$] for the four DEMs shown in Table 3, for the case when one month passed after the CCD bakeout, *i.e.* 800 Å of contaminant on the CCD. The dashed and dotted lines indicate the positions where $T_{\rm ratio}$ is equal to $T_{\rm mean}$, and where the difference between $T_{\rm mean}$ and $T_{\rm ratio}$ is 50%, respectively. The number of analyzed filter pairs is shown in parentheses.

Condition (D), we evaluated the error in the estimated filter-ratio temperature. Although the error is derived under the assumption that the corona is the single filter-ratio temperature, the derived error is useful as the accuracy-index of the estimated filter-ratio temperature, which depends on the photon noise and the shape of the temperature responses in each filter.

5.3. Meaning of Filter-Ratio Temperature Derived with XRT

The actual solar corona may have a multi-temperature structure, and the temperature derived with the filter-ratio method is a mean temperature weighted by the filter responses. Unlike filter-ratio temperatures from narrow-band instruments (see the discussion in Martens, Cirtain, and Schmelz (2002)), filter-ratio temperatures from broad-band instruments (*e.g.*, *Hinode*/XRT and *Yohkoh*/SXT) are expected to provide a temperature which is close to the mean temperature [$T_{\rm mean} \equiv \frac{\int T \times {\rm DEM}\, {\rm d}T}{\int {\rm DEM}\, {\rm d}T}$] weighted by the differential emission measure (DEM) of the coronal observation target, as demonstrated by Acton, Weston, and Bruner (1999) for *Yohkoh*/SXT. In the case of *Hinode*/XRT, Figure 17 shows the correlation between the DEM-weighted mean temperature [$T_{\rm mean}$] and filter-ratio temperature [$T_{\rm ratio}$] for four DEMs (regions), summarized in Table 3. The $T_{\rm ratio}$ is calculated for all suitable filter pairs, which are investigated in Section 5.2 and summarized in Figure 14. The values of $T_{\rm ratio}$ derived with different filter pairs are different, *i.e.* the thinner and thicker filter pairs give the lower and higher $T_{\rm ratio}$, respectively (see the "v" marks in Figures 13 and 14). Additionally, $T_{\rm ratio}$ is higher than $T_{\rm mean}$ in the lower-temperature region ($T < 1$ MK: coronal hole), and $T_{\rm ratio}$ is lower than $T_{\rm mean}$ in the higher-temperature region ($T > 10$ MK: flare). This is caused by the bias of the XRT temperature response (Figure 10), which has a sensitivity to mainly 1 – 10 MK plasma. However, the difference between $T_{\rm mean}$ and $T_{\rm ratio}$ is less than 50% (within two dotted lines in Figure 17) for all filter pairs. Hence, we claim that the filter-ratio temperature with XRT (the broad-band instruments) is useful for quantitative analysis, *e.g.*, coronal energetics. Additionally, the filter-ratio method has the following advantages:

i) the filter-ratio method applied to XRT data can estimate a coronal temperature over a wide field of view at once, in contrast to a spectrometer;
ii) the filter-ratio method can investigate a rapid temporal evolution of coronal temperature, with a time scale well below one minute, since XRT can quickly take a data set with a pair of filters.

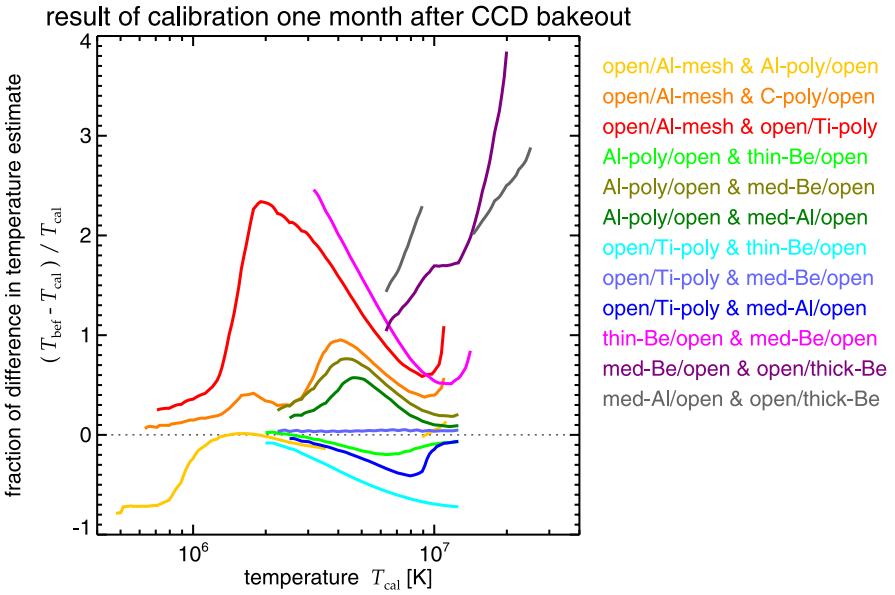

Figure 18 Comparison between filter-ratio temperatures with the calibrated results in this article [T_{cal}] and with the instrumental parameters before calibration [T_{bef}]. The horizontal and vertical axes of this plot show T_{cal} and the fraction of the difference in the temperature estimate defined as $(T_{bef} - T_{cal})/T_{cal}$, respectively. The dotted line indicates the position where these temperatures are the same.

Hence, the temperature diagnostics obtained with the filter-ratio method and the advanced DEM analysis with data sets taken with multiple filters of the XRT or *EUV Imaging Spectrometer* (EIS) onboard *Hinode* are complementary.

6. Summary

We calibrated the effective-area and coronal-temperature response of the XRT using ground-based test data and also on-orbit data in X-rays and visible light, with the effect of contamination taken into account in a way corresponding to the best of our knowledge. The calibrated thicknesses of pre-filter and FPAFs are summarized in Table 1. The time-varying thicknesses of the contaminant accumulated on the CCD and FPAFs are shown in Figures 6 and 7, respectively.

Here, we examine how much our calibration results improve the coronal-temperature-diagnostic capability of XRT. Figure 18 shows a comparison between filter-ratio temperatures with our calibrated results and with the instrumental parameters before calibration (Golub *et al.*, 2007) for some suitable filter pairs (see Figure 14). This plot is created as follows. We derive the expected intensity ratios with our calibrated parameters at each temperature [T_{cal}] in the useful temperature range of each filter pair (see Figure 14). Next, we derive the temperature [T_{bef}] with the above-derived ratios and instrumental parameters before calibration. Figure 18 shows the fractional difference of the temperature estimate defined as $(T_{bef} - T_{cal})/T_{cal}$. Note that this plot varies with the accumulation of contaminants on the CCD and FPAFs as a function of time. This plot shows the case when one month passed after the CCD bakeout, *i.e.* 800 Å of contaminant was deposited on the CCD. While

some filters happen to provide consistent temperature estimates in some temperature ranges, for most filters there are large deviations, as illustrated in Figure 18. Hence, we claim that our calibration result is indispensable for accurately estimating coronal temperatures with XRT.

On the basis of our calibration results, we reviewed the coronal-temperature-diagnostic capability of XRT with the filter-ratio method. XRT has a wide variety of suitable filter pairs to estimate coronal temperatures with the filter-ratio method. For reference, we briefly mention the multi-temperature diagnostics. Using simultaneous data from more than two filters allows one to obtain more information on the temperature distribution, and to resolve the ambiguity in the results of the filter-ratio method (*i.e.*, it increases the ability to pass Condition (C) in Section 5.2). With many XRT filters, at least more than four filters (Golub *et al.*, 2007), one can try to derive the differential emission measure (DEM). In this situation, the calculation of DEM with the XRT data including the error estimate itself is the topic of interest (Schmelz *et al.*, 2009a, 2009b, 2010). The XRT is a powerful instrument not only for observing the morphology of coronal structures in detail but also in deriving coronal physical quantities.

6.1. Software for the Coronal-Temperature Diagnostics with XRT

Lastly, we itemize the software used for the XRT calibrations and the coronal-temperature diagnostics described in this article. These routines are distributed in the hinode/xrt directory tree of Solar Software (Freeland and Handy, 1998).

xrt_time2contam.pro
: gives the total thickness of contaminant on the FPAFs and the CCD as a function of time (Figures 6 and 7).

xrt_eff_area.pro
: gives the XRT effective area (Figure 9).

xrt_flux.pro
: gives the XRT temperature response (Figure 10).

xrt_cvfact.pro
: gives the conversion factor $[K^{(1)}(T)]$ from observed DN to incident photon number (Equation (10) and the top panel of Figures 12). With the /error keyword, the conversion factor $[K^{(2)}(T)]$ from observed DN to the square of DN error is given (Equation (13) and the bottom panel of Figures 12).

xrt_teem.pro
: returns the estimated coronal temperature and emission measure with the filter-ratio method (Figure 11).

The XRT team have provided more software than the above. For example, we have the following.

make_xrt_wave_resp.pro
: gives the XRT effective areas, and it provides an option for user-specified spectral emission models.

make_xrt_temp_resp.pro
: gives the XRT temperature responses, and provides an option for user-specified spectral emission models.

The above two procedures are useful to examine the effect of uncertainties in the atomic physics, *i.e.* difference in spectral emission models, on the temperature analysis. For the DEM analysis, we have the following.

xrt_dem_iterative2.pro
gives DEM solutions for multi-filter datasets, and provides an option for Monte Carlo-style analysis of uncertainties.

The details of how to analyze XRT data with these software packages are described in the XRT analysis guide (http://xrt.cfa.harvard.edu/resources/documents/XAG/XAG.pdf).

Acknowledgements The authors thank the members of the XRT team for useful discussions and comments. We acknowledge D. Brooks and H. Warren for various pieces of information on quiet-Sun and active region DEMs. *Hinode* is a Japanese mission developed and launched by ISAS/JAXA, collaborating with NAOJ as a domestic partner, NASA and STFC (UK) as international partners. Scientific operation of the *Hinode* mission is conducted by the *Hinode* science team organized at ISAS/JAXA. This team mainly consists of scientists from institutes in the partner countries. Support for the post-launch operation is provided by JAXA and NAOJ (Japan), STFC (UK), NASA, ESA, and NSC (Norway). CHIANTI is a collaborative project involving the NRL (USA), the Universities of Florence (Italy) and Cambridge (UK), and George Mason University (USA). We wish to express our sincere gratitude to the late Takeo Kosugi, former project manager of *Hinode* (*Solar-B*) at ISAS, who passed away in November 2006. Without his leadership in the development of *Hinode*, this mission would never have been realized. We express our sincere gratitude to those who participated in, or supported, the XRT end-to-end calibration measurement at MSFC XRCF that was carried out for two weeks in May – June 2005. First of all, we are very much indebted to an extremely-talented team of people at XRCF led by C. Reily and J. McCracken, including R. Siler, E. Wright, J. Carpenter, J. Keegley and G. Zirnstein, and also M. Baker, H. Haight, B. Hale, T. Hill, B. Hoghe, D. Javins, J. Norwood, H. Rutledge, G. St. John, J. Tucker, and D. Watson. Without their continuous, enormous support including preparation of the LN2-cooled cold plate facing XRT radiators in the cryogenic chamber of XRCF, from an early preparation phase of the XRCF experiment and throughout the experiment's duration, the filter calibration at XRCF would have been totally impossible. We are also grateful to people from SAO who supported the XRCF measurement; G. Austin, W. Podgorski, E. Dennis, J. Chappel, D. Caldwell, W. Martell, M. Harris, M. Cosmo, D. Weaver, S. Park and T. Kent who participated in the experiment, and P. Cheimets, J. Bookbinder, J. Boczenowski. Also A. Sabbag of Naval Research Laboratory is appreciated for his support during a pre-shipment instrument check performed at SAO. K. Kumagai and M. Tamura of NAOJ, K. Yaji of Rikkyo U., and K. Kobayashi of MSFC are greatly appreciated for preparing, and participating in, the XRCF experiment. Also, people from MSFC, L. Hill, J. Owens, B. Cobb, D. Coleman, R. Jayroe, T. Perrin, D. Schultz, A. Sterling and C. Talley are sincerely acknowledged for their various supportive contributions throughout our stay in Huntsville and also for our transportation to and from XRCF. Finally, the authors are grateful to the referees for their detailed and careful reviews.

Appendix A: Ground-Based Calibration

Measurements of the X-ray transmission of focal-plane analysis filters (FPAFs) were made with five characteristic X-ray lines as part of the end-to-end throughput test with the flight XRT telescope (except for the flight pre-filters and sun-shield plate in front of the telescope) performed at the X-ray Calibration Facility (XRCF) at NASA/Marshall Space Flight Center in June 2005. Spectra of the X-ray lines used for the measurement are shown in Figure 19 (see also Appendix E for details).

A.1. Check of XRCF X-Ray Spectra

In the end-to-end test, XRT pre-filters were not installed. Therefore, the effective area as measured at the XRCF can be written as

$$A_{\mathrm{eff@XRCF}} = A \times R_{\mathrm{M1}} \times R_{\mathrm{M2}} \times \mathcal{T}_{\mathrm{FPAF1}} \times \mathcal{T}_{\mathrm{FPAF2}} \times QE_{\mathrm{CCD}}. \tag{17}$$

With FW1 and FW2 set to the open positions, this can be simplified to

$$A^{\mathrm{open}}_{\mathrm{eff@XRCF}} = A \times R_{\mathrm{M1}} \times R_{\mathrm{M2}} \times QE_{\mathrm{CCD}}. \tag{18}$$

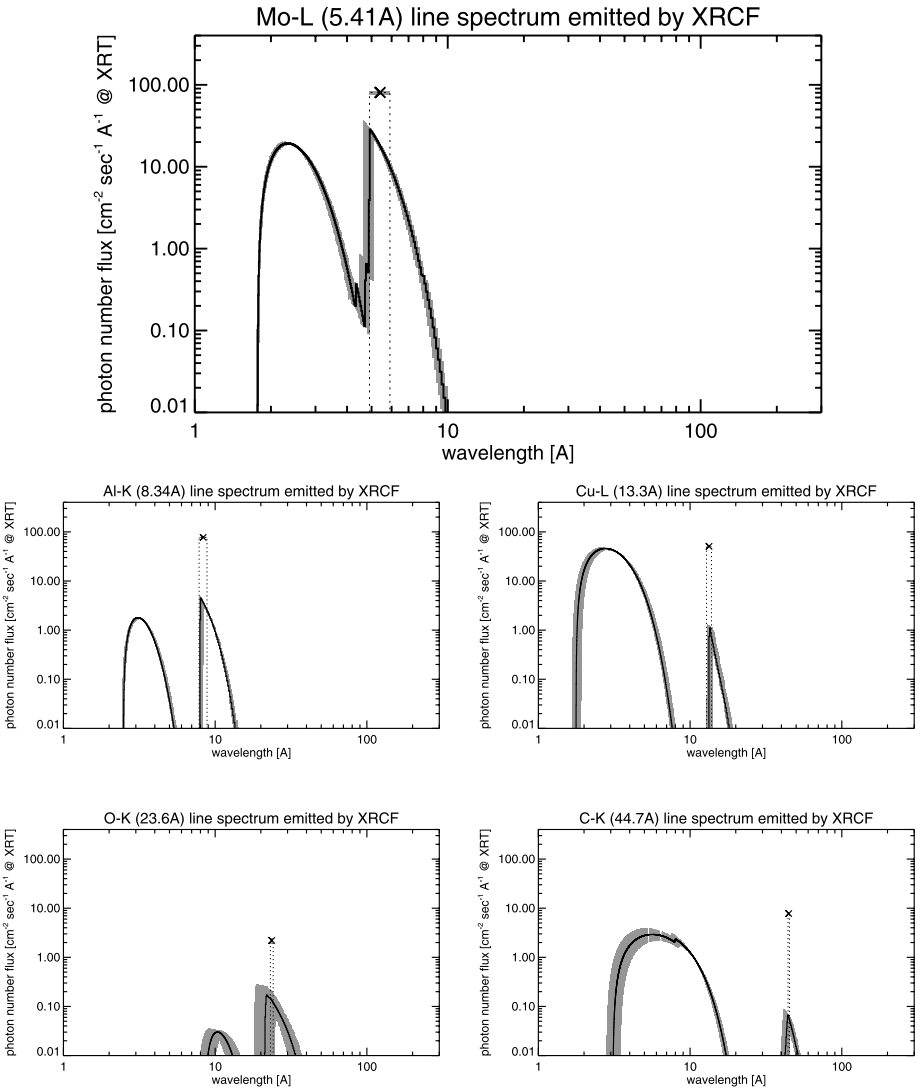

Figure 19 Spectra of characteristic X-ray lines and continua emitted by XRCF. These are the incident spectra into XRT. The solid lines are the spectra of continuum bremsstrahlung. The crosses (×) show the wavelength (horizontal axis) and photon-number flux in units of $\mathrm{cm}^{-2}\,\mathrm{sec}^{-1}$ (vertical axis) emitted by the characteristic X-ray lines. If we present the characteristic X-ray lines as spectra in units of $\mathrm{cm}^{-2}\,\mathrm{sec}^{-1}\,\text{Å}^{-1}$, the spectra can be indicated with the dotted lines, whose width and height are 1 Å and the same value as photon-number flux in the unit of $\mathrm{cm}^{-2}\,\mathrm{sec}^{-1}$, respectively. The gray areas show the error bar of the estimated spectra.

With the manufacturer-supplied information on the geometric aperture area [A], on the reflectivities of primary and secondary mirrors [R_{M1} and R_{M2}], and on the quantum efficiency [QE_{CCD}] of the CCD, we can check whether the XRCF X-ray spectra (Figure 19) were well estimated, by comparing the signal from the XRT CCD (in terms of data number (DN), which represents the number of electrons generated) at the open/open position and that ex-

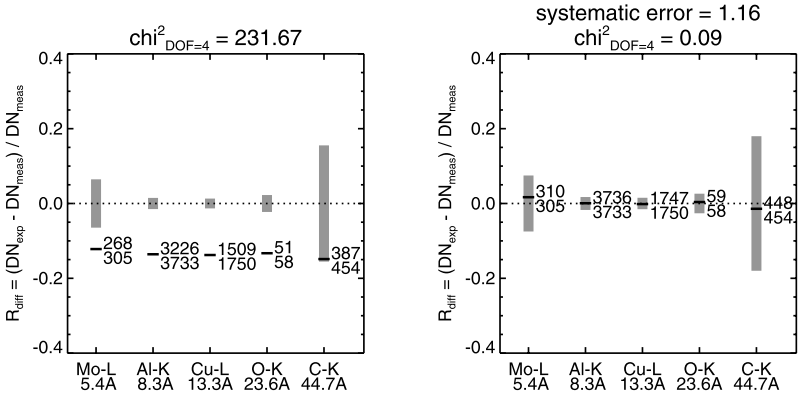

Figure 20 Left panel: the residual between the DN measured with XRT CCD (DN_{meas}) and DN expected with XRCF spectra (DN_{exp}) with one second exposure in the case where FW1 and FW2 are set at the open position. Black marks (−) indicate the differences defined as $R_{diff} \equiv (DN_{exp} - DN_{meas})/DN_{meas}$. The top and bottom values near the black marks (−) show the value of DN_{exp} and DN_{meas}, respectively. The gray bar is the 1σ error bar. Right panel: the best correlative case, where the systematic error of 1.16 is taken into account.

pected from energy spectra of the X-ray beams at XRCF measured with a flow proportional counter (FPC) (see Appendix D.1 for details).

The left panel of Figure 20 shows the result of the comparison. The vertical axis shows the fractional difference $R_{diff} \equiv (DN_{exp} - DN_{meas})/DN_{meas}$, where DN_{meas} and DN_{exp} are the measured DN with the CCD of the XRT and the expected DN from the XRCF spectra. If DN_{meas} and DN_{exp} are consistent, $R_{diff} \approx 0$. The 1σ error is shown by gray bars with observation error of CCD (*e.g.*, photon noise and fluctuation of dark level) and the estimate error of the XRCF spectrum taken into account as the source of errors. We found that R_{diff} of each X-ray line is almost constant at -0.14 as shown in the left panel of Figure 20. This suggests that the spectral shape of the XRCF beam is well estimated, but that the intensity is underestimated. We found that "$DN_{exp} \times 1.16$" gives the best fit to the data with $\chi^2_{DOF=4} = 0.09$, as shown in the right panel of Figure 20, where DOF stands for the degree of freedom. We consider that this coefficient of 1.16 is the systematic error caused by the ambiguous aperture area of FPC and the slight difference in the locations of XRT and FPC (see Figure 41), because we do not know the exact values of these, and we apply the approximate values provided from XRCF. Below, we derive DN_{exp}, correcting this systematic error. The fact that DN_{meas} and DN_{exp} show a good match across the entire wavelength range in the right panel of Figure 20 gives support to the reliability of the calibration result on the thicknesses of FPAFs with the XRCF X-ray spectra.

A.2. Calibration of Focal-Plane Analysis Filters

Among the materials used for FPAFs, aluminum, titanium, and beryllium can form thin oxidization layers on their surfaces. Hence, the effect of oxidization should correctly be taken into account when calibrating FPAFs. Oxidization of filters decreases transmission of FPAFs, especially at longer wavelengths, because the added oxygen absorbs X-rays. Considering oxidization, the transmission of FPAFs ($\mathcal{T}_{FPAF1}$ and $\mathcal{T}_{FPAF2}$ for FW1 and FW2, respectively) is expressed as

$$\mathcal{T}_{FPAF} = \mathcal{T}_{pure} \times \mathcal{T}_{ox} \times \mathcal{T}_{supp}, \tag{19}$$

where $\mathcal{T}_{\rm pure}$, $\mathcal{T}_{\rm ox}$, and $\mathcal{T}_{\rm supp}$ are the transmission of pure metal (unoxidized metal), oxidized metal, and support material, respectively. The transmission $[\mathcal{T}]$ of the material is determined by the material and its thickness $[d]$ by

$$\mathcal{T} = \exp\left(-\frac{d}{l_{\rm att}(\lambda)}\right), \tag{20}$$

where $l_{\rm att}(\lambda)$ is the attenuation length for the material at the X-ray wavelength λ. The attenuation length of respective atoms ($Z = 1-92$, where Z is the atomic number) in the energy range of 50 – 30 000 eV is derived by Henke, Gullikson, and Davis (1993) and can be obtained from "X-Ray Interactions With Matter" (http://henke.lbl.gov/optical_constants/). Using Equations (17), (18), (19), (20) and also Equation (34) in Appendix D.1, $\mathrm{DN}_{\rm exp}$ at an exposure time of $t = 1$ second is written

$$\mathrm{DN}_{\rm exp} = \int P(\lambda) \times A^{\rm open}_{\rm eff@XRCF}(\lambda) \times \exp\left(-\frac{d_{\rm pure}}{l_{\rm att}(\lambda)}\right) \times \mathcal{T}_{\rm ox}(\lambda). \\ \times \mathcal{T}_{\rm supp}(\lambda) \times \frac{C}{\lambda}\,\mathrm{d}\lambda, \tag{21}$$

where $d_{\rm pure}$ is the pure metal thickness of FPAFs, and P is the photon-number spectrum of the X-ray beam at XRCF (see Figure 19). C gives the conversion from number of photons at wavelength λ to signal DN generated on the CCD, and it is expressed as $C = t \times hc/e/3.65/G$, where G is the system gain of the CCD camera, which is 57.5 [e DN^{-1}] for XRT (Kano *et al.*, 2008). In performing the fitting, we set the support thickness $d_{\rm supp}$, namely $\mathcal{T}_{\rm supp}$, as a fixed parameter. The reason for this is described below. For $\mathcal{T}_{\rm ox}$, we adopt the oxidized-metal thickness derived with the on-orbit data, because after the end-to-end test at the XRCF and until the launch of *Hinode*, FPAFs were continuously purged with dry nitrogen to prevent additional oxidization.

On the basis of the analysis in Appendix B.3.1, the oxidized-metal thickness for the polyimide side can be regarded as 0 Å, while that for the metal side (exposed to ambient atmosphere) can be consistently set to 75 Å, irrespective of the metal material. We note that our 75 Å oxidized-metal thickness is consistent with the measurement of a well-oxidized aluminum filter by Powell *et al.* (1990). Hence, in this calibration, the fitting parameter is the metal thickness $[d_{\rm metal}]$ of each FPAF only.

The results of fitting for each FPAF are shown in Figure 21 and Figure 22. For all filters, the fitted value $[R_{\rm diff}]$ is determined within 1σ error. The calibrated thicknesses of the FPAFs are summarized in Table 1.

In this fitting analysis, there are three features worthy of note.

i) The thickness of the polyimide film, which is used in Al-poly, C-poly, and Ti-poly filters as supports of these thin-metal filters. According to the filter manufacturer (Luxel), the thickness of polyimide was well controlled. Therefore we fix the polyimide thickness at the values provided by the manufacturer (see Table 1).

ii) The fraction of the open area of the support mesh for the Al-mesh filter. On the basis of the microscope measurement performed by the manufacturer, we identified the geometrical open area of mesh as 77%. In the calibration of the Al-mesh filter thickness, we adopted the value of 77% with scattering from the mesh pattern and the X-ray shape on it taken into account. The details of the annulus transmission are described in Appendix F.

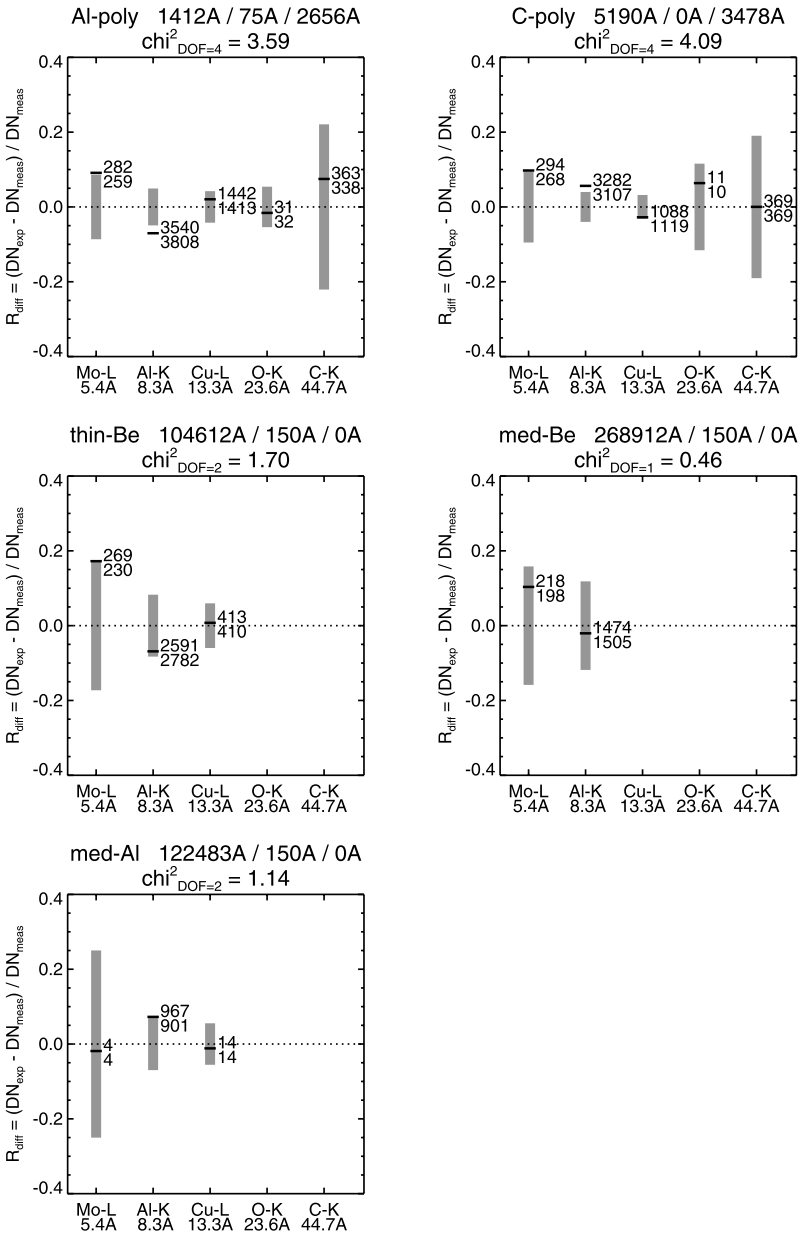

Figure 21 Calibrated thicknesses of focal-plane analysis filters mounted on Filter Wheel 1. The thicknesses described in the left, middle, and right side of "/" show the estimated pure metal, oxidized metal, and support thicknesses, respectively. Black marks (−) indicate the differences defined as $R_{\rm diff} \equiv ({\rm DN_{exp}} - {\rm DN_{meas}})/{\rm DN_{meas}}$, where $\rm DN_{meas}$ is the DN measured with XRT CCD and $\rm DN_{exp}$ is the DN expected with XRCF spectra. The top and bottom values near the black marks (−) show the value of $\rm DN_{exp}$ and $\rm DN_{meas}$ with a one-second exposure, respectively. The gray bar is the 1σ error bar.

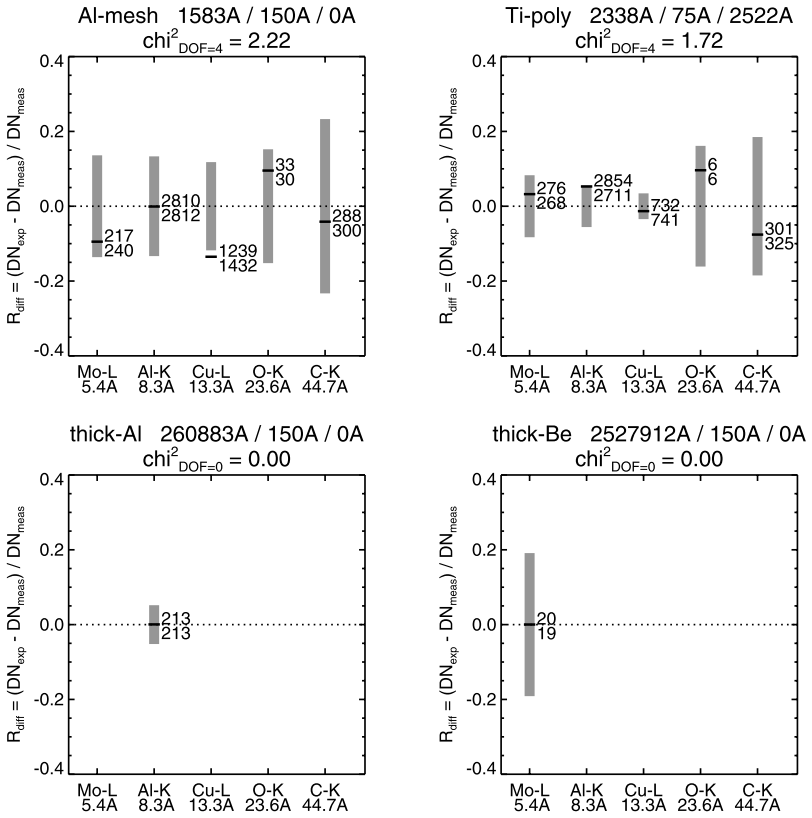

Figure 22 Calibrated thicknesses of the focal-plane analysis filters mounted on Filter Wheel 2. The meaning of this figure is same as Figure 21.

Table 4 Materials used in our calibration.

Material	Molecular weight	Density
Al	26.98	2.699 g cm^{-3}
C	12.01	2.2 g cm^{-3}
Be	9.01	1.848 g cm^{-3}
Ti	47.87	4.54 g cm^{-3}
Al_2O_3	101.96	3.97 g cm^{-3}
TiO_2	79.87	4.26 g cm^{-3}
BeO	25.01	3.01 g cm^{-3}
polyimide ($C_{22}H_{10}N_2O_5$)	–	1.43 g cm^{-3}

iii) The last note is about the calibration of thick filters, namely med-Be, thick-Al, and thick-Be filters. Since low-energy X-rays do not have enough transmission through the thick filters, we were able to use one or two X-ray lines to calibrate these thick filters. Thus we consider the calibration of the thick filters to be less certain. However, according to Equation (20), even if the calibrated thicknesses of the thick filters have some error,

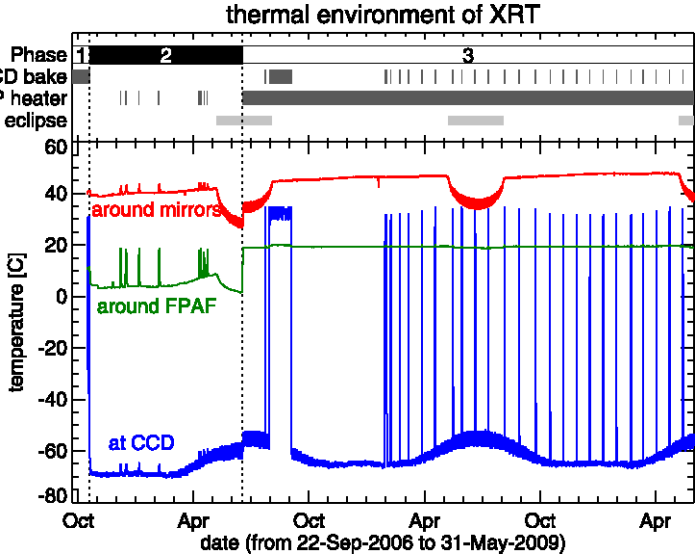

Figure 23 Thermal environment of the XRT. The red, green, and blue lines indicate the temperature at the mirror support plate (XRTD_TEMP_11), at the focal-plane shutter motor (XRTD_TEMP_22), and at the CCD (XRTE_CCD_TEMP), respectively, where XRTD_TEMP_11, XRTD_TEMP_22, and XRTE_CCD_TEMP are names in the *Hinode* telemetry.

the effect on their transmission is small. Hence we accept the thicknesses derived with XRCF data for now. To obtain further knowledge of the thicknesses of the thick filters, we need to take enough data sets with intense X-ray sources, *i.e.* active regions and flares, with thick filters. Calibration with on-orbit observational data is a project for future work.

In Table 1, we see that, for each metal filter, the difference between our thickness and that from the manufacturer is almost within the uncertainties reported by the manufacturer, except for the Al-poly (the difference is 200 Å) and C-poly (800 Å). In the case of the Al-poly filter, the manufacturer found a discrepancy between their measured thickness and that inferred from their own transmission measurement in visible light, and noted that the Al-poly filter should be thicker than their reported value. This information is consistent with our result. In the case of the C-poly filter, the difference is significantly large. This could have been caused by the different method of measurement. As we mentioned, we derived the thickness with the transmission in X-rays and attenuation length. The attenuation length depends on the density of material. In our calibration, we used the typical density of material summarized in Table 4 with the typical density of graphite adopted for our analysis on C-poly filter. However, it often happens that the assumption of a typical density is different from the actual density for the filter, especially in the case of a C-poly filter, because carbon is not a metal. According to the estimates of the manufacturer of the filters, the density of their carbon film is about 90% of typical value of graphite, namely about 1.9 $\mathrm{g\,cm^{-3}}$, because the carbon is evaporated using an electron beam in the process of making the thin carbon filter. Considering this difference in density, the X-ray transmission of the C-poly filter estimated with our calibrated thickness and the typical density is consistent with that calculated with the manufacturer's thicknesses and $\approx 90\%$ of the typical density, because our

calibrated thickness (5190 Å, see Table 1) is about 90% of the manufacturer's thicknesses (6038 Å).

Appendix B: On-orbit Calibration

B.1. Thermal Distribution Inside XRT

Figure 23 shows the temporal evolution of the XRT thermal environment. The red, green, and blue lines indicate the temperature at the mirror support plate, at the focal-plane shutter motor, and at the CCD, respectively. From a thermal viewpoint, there are three distinct periods in XRT operation, which are shown as Phases 1, 2, and 3 in Figure 23. Phase 1 is the period from the launch of *Hinode* to first light, where the CCD bakeout heater was kept on to avoid contaminants accumulating on the CCD. When the CCD bakeout heater is on, we can say that no contaminants accumulate on the CCD, since the temperature of the CCD becomes about 30°C, which is higher than its surroundings. Phases 2 and 3 are the periods of normal operation of XRT without and with enabling (turning on) the operational heater for the telescope tube, respectively. With the operational heater enabled, the rear end of the XRT telescope tube (in front of the CCD camera when viewed from the Sun) is warmed up to about +20°C. In these periods, the CCD was cooled down to a temperature of about −60°C to reduce the dark noise. Since the CCD is the coolest component in XRT, it is possible that the contaminant selectively accumulates on the CCD. The operational heater was originally kept off in Phases 1 and 2 due to technical reasons, and was then enabled from 18 June 2007 on. The period after this date is labeled Phase 3.

Let us now examine the relationship between the thermal environment of XRT and the observed decrease in quiet-Sun X-ray intensity. The bottom panel of Figure 8 shows the temporal evolution of the X-ray intensity ratio normalized by the intensity observed with the Ti-poly filter to remove possible variation in emission measure for the quiet Sun (see Equations (40) or (41) in Appendix D.2). In the subsequent analysis, we make the assumption that the profile of the differential emission measure in the quiet Sun is approximately constant, and the variation in the observed quiet-Sun intensity ratio can be attributed solely to the accumulated contaminant. During Phases 2 and 3, the CCD temperature was almost constant at around −60°C. The decrease in the intensity ratio was continuously observed in these phases, indicating that the contaminant kept accumulating on the CCD in both Phases 2 and 3 (except during the bakeout periods). The X-ray intensity ratio recovered to almost the same level after each CCD bakeout as seen in Phase 3 in the bottom panel of Figure 8. This implies two things:

i) Each bakeout reduces the contaminant on the CCD to the same thickness (except for the "spots" discussed below).
ii) Thickness of contaminant accumulated on each FPAF remains unchanged during Phase 3.

The result *i*) is supported by the behavior of the G-band intensity where the G-band intensity returned (reduced) to almost the same level by the CCD bakeouts (see Figure 28). As will be mentioned in Appendix B.3.3, we found that on/off operations of the operational heater when the temperature around the FPAFs is cooler than 5°C cause accumulation of contaminant on the FPAFs. Hence, we suspect that the accumulation of contaminant on the FPAFs took place in Phase 2 while it did not in Phases 1 and 3.

Meanwhile, the first and third bakeouts created lumps of contaminant which are distributed over the whole CCD as spot-like patterns (see Figure 49 in Appendix G). These spots

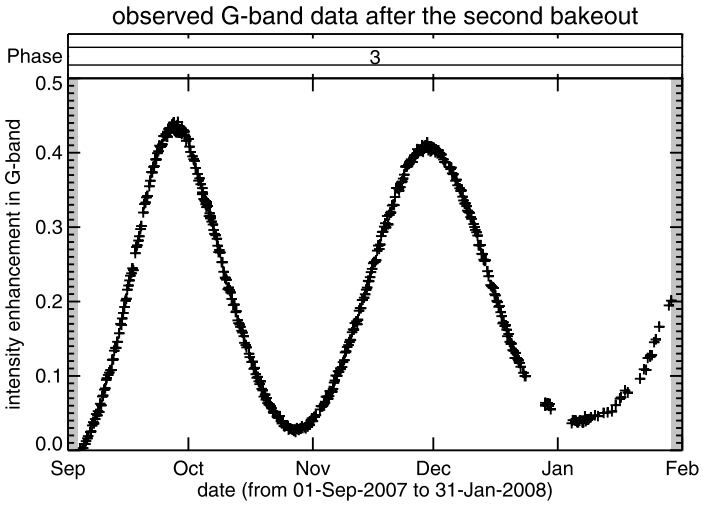

Figure 24 G-band intensity enhancement observed after the second CCD bakeout from 512 × 512 pixels at CCD center. The first G-band data just after the second bakeout has been taken as the reference for intensity enhancement. The gray areas in the left and right sides of this plot are the second and third CCD bakeout periods, respectively.

of contaminant cannot be removed by subsequent bakeouts. We consider the excess amount of contaminant accumulated on the CCD before the first and third bakeouts to be the cause of these spots. The details of the spots are described in Appendix G. In this regard, we consider the contamination on the CCD to comprise two seemingly different components. One is a laminar contaminant that accumulates across the CCD as time goes on and can be well removed by a CCD bakeout when the accumulation thickness is small enough. The other is a "condensed" contaminant forming spot-like patterns over the CCD. This condensation of contaminants occurs in association with a CCD bakeout when the accumulation thickness is large (the threshold thickness is not known) and cannot be removed by any further CCD bakeouts. In this article, we characterize only the laminar contaminant for contamination on the CCD. Detailed characterization of the spot-shaped contamination is a subject for future study.

We assume that no contamination accumulated on the pre-filter, because the temperature of the front end of the telescope (around the mirrors) was the warmest portion inside the telescope with the temperature at around or even exceeding 40°C in all phases.

B.2. Visible Light Analysis – Contamination on the CCD

B.2.1. Method

We explain our method to measure the thickness of the contaminant accumulated on the CCD using visible light (G-band) data. Figure 24 shows the temporal evolution of the G-band intensity after the second CCD bakeout on 3 September 2007. This plot was made from the average G-band intensity over an area of 512 × 512 pixels at the center of the CCD for full-Sun (synoptic) images where the center of the Sun is located at the same position of the CCD (near the center of the CCD). Notable features in this plot are:

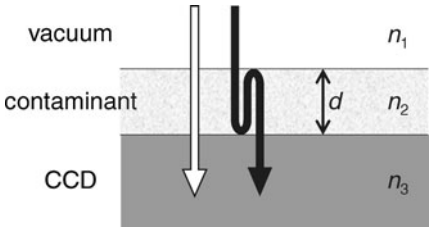

Figure 25 Anti-reflection effect by the contaminant accumulated on CCD.

i) the intensity shows enhancement (non-negative increase) from the first G-band data just after the second bakeout, and

ii) the intensity shows a periodic oscillation. The period of the oscillation is about 53.3 days. The maximum intensity enhancement is about 40% of the reference intensity. This amount of enhancement cannot be explained by the fluctuation of the solar intensity, which is less than 1% in visible light during the 11-year solar cycle.

Our interpretation of the oscillation is that it is caused by interference within a contaminant layer (anti-reflection effect). Figure 25 illustrates anti-reflection with a contaminant layer on the CCD. Both the direct ray (white arrow) and the reflected rays (black arrow) enter the CCD. Assuming three layers (vacuum, contaminant, and CCD) the transmission of the visible light [$\mathcal{T}$] into the CCD is expressed as

$$\mathcal{T} \equiv \frac{I_\mathrm{t}}{I} = \frac{4n_1n_3}{(n_1+n_3)^2}\left[1-\sin^2 k_2 d \times \left\{\frac{(n_3^2-n_2^2)(n_2^2-n_1^2)}{n_2^2(n_1+n_3)^2}\right\}\right]^{-1} \tag{22}$$

(see Appendix H for the derivation of this equation), where I is the intensity in vacuum, I_t transmitted intensity into CCD, n refractive index of each layer, k_2 the wavenumber of the G-band in the contaminant layer, and d is the thickness of the contaminant layer. The enhancement [E] of the G-band intensity is then given by

$$E \equiv \frac{\mathcal{T}-\mathcal{T}_{d=0}}{\mathcal{T}_{d=0}} = \left[1-\sin^2 k_2 d \times \left\{\frac{(n_3^2-n_2^2)(n_2^2-n_1^2)}{n_2^2(n_1+n_3)^2}\right\}\right]^{-1} - 1. \tag{23}$$

This equation clearly shows that the increasing thickness [d] of contamination causes periodic intensity oscillation. The thickness of the contaminant for a local minimum in the intensity enhancement is given by

$$d_\mathrm{min} = \frac{m\pi}{k_2}, \tag{24}$$

where m is a positive integer ($m = 1, 2, 3, \ldots$). The period of the intensity oscillation can be related to the contamination thickness by

$$\Delta d_\mathrm{min} = \frac{\pi}{k_2} = \frac{\lambda_2}{2} = \frac{\lambda_0}{2n_2}, \tag{25}$$

where n_2 is a refractive index of the contaminant and λ_0 is the wavelength of the incident visible light in vacuum (4300 Å in the G-band). This means that if we know the refractive index [n_2] of the contaminant material, then we can measure the thickness of the contaminant using the measured period of the G-band intensity oscillation.

In the above, we considered only contaminants on the CCD. But it is possible that the contaminants also accumulated on the G-band glass filter. (Note that this is indeed the case

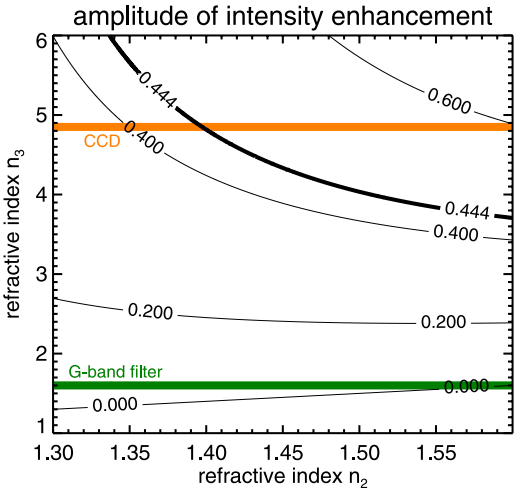

Figure 26 The expected amplitude (maximum value) of the intensity enhancement by the anti-reflection effect (a in Equation (26)) is shown by contours. The observed amplitude of the intensity enhancement (0.444; see Figure 24) is indicated by a thick contour. The refractive indexes of the CCD ($n_3 \approx 4.9$) and the G-band filter ($n_3 \approx 1.6$) are shown in orange and green, respectively.

for the metal filters; see Appendix B.3.1.) Thus, the possible effect of contaminants accumulated on the G-band glass filter should be considered. As will be detailed in Appendix B.3.1, we found that the contaminant is a long-chain organic compound which consists of carbon, hydrogen, and oxygen, and that its refractive index is close to 1.5. With this information, let us next consider the anti-reflection effect with the contaminant accumulated on the G-band filter. Figure 26 shows the expected amplitude (maximum value) of the intensity enhancement caused by the anti-reflection effect based on Equation (23). The material (refractive index) of the G-band filter, the CCD and the contaminant are glass ($n_3 \approx 1.6$), silicon ($n_3 \approx 4.9$) and contaminant ($n_2 \approx 1.5$), respectively. As seen in the green area of Figure 26, intensity enhancement caused by a (possible) contaminant on the G-band filter is close to zero due to the proximity of $n_2 \approx 1.5$ and $n_3 \approx 1.6$. Meanwhile, the contaminant on the CCD can enhance the G-band intensity enough (more than 0.4) for the observed enhancement shown in Figure 24. Hence, even if the thickness of the contaminant accumulated on the G-band filter changes as a function of time, we can ignore the G-band intensity enhancement caused by the contaminant on the G-band filter.

By assuming that the refractive index of the contaminant is 1.5 and using Equation (25), one period of intensity oscillation corresponds to a 1433 Å thickness of contaminant as an average over 512 × 512 pixels at the center of CCD. The accumulation rate of the contaminant there is estimated to be 9800 Å year^{-1}, because the period of the G-band intensity oscillation at the CCD center is about 53.3 days.

B.2.2. Model

In order to avoid excess accumulation of contaminant on the CCD, we started to perform a regular CCD bakeout every three – four weeks, since the third bakeout. This means that, from that time onward there is not much time to see the intensity oscillation in the G-band profile between two adjacent bakeouts. Hence, a quantitative estimate of the contaminant thickness directly from the G-band intensity turned out to be not possible. Instead, for the period after the third bakeout, we developed an empirical model of the G-band intensity oscillation, using the data between the second and third CCD bakeouts. On the basis of this model, we estimated the time-dependent thickness of the contaminant on the CCD after the third CCD bakeout in addition to the period between the second and third CCD bakeouts.

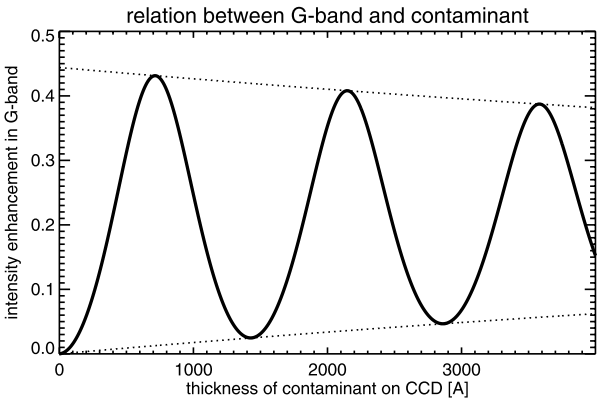

Figure 27 Relation between intensity enhancement in the G-band and thickness of contaminant on the CCD. The dotted curves show the exponentially decaying amplitude of the intensity enhancement oscillation.

In the profile of the observed intensity enhancement (Figure 24), the periodic oscillation and the decay of amplitude are seen. The empirical model incorporates these two properties. Modifying Equation (23), the empirical model, which relates the enhancement of the intensity in the G-band [$E_{\rm model}$] to the thickness of the contaminant [d], is expressed by the following equation whose profile is shown in Figure 27:

$$E_{\rm model} = \left[\left\{\left(1 - \sin^2 k_2 d \times \frac{a}{1+a}\right)^{-1} - 1\right\} - \frac{a}{2}\right] \times \exp(-b \times d) + \frac{a}{2}, \tag{26}$$

where a and b are the amplitude (maximum value) and decay coefficient of intensity enhancement, respectively. The inside of { } in Equation (26) is a rewriting of Equation (23) with

$$\frac{a}{1+a} = \frac{(n_3^2 - n_2^2)(n_2^2 - n_1^2)}{n_2^2 (n_1 + n_3)^2}. \tag{27}$$

The best-fit values to the observed G-band intensity enhancement (see Figure 24) are $a = 0.444$ and $b = 8.23 \times 10^{-5}$.

In this empirical model, there are two features worthy of note:

i) With the observed amplitude (maximum value) of intensity enhancement ($a \approx 0.444$) and the refractive index of the CCD ($n_3 \approx 4.9$), the refractive index of the contaminant is calculated to be $n_2 \approx 1.4$ (see Figure 26). This value is certainly different from our assumption that the refractive index of the contaminant is 1.5.

ii) In the observed intensity profile (Figure 24), there is slight decrease in the amplitude, which is incorporated as an exponential decay in the model (b in Equation (26)) and it is indicated by dotted lines in Figure 27.

As will be discussed in Appendix K.2, we conclude that they do not significantly affect the results of the calibration of the XRT.

We continuously monitor the temporal evolution of the G-band intensity (Figure 28). As seen in Figure 28, only a portion of an entire cycle of the intensity enhancement, namely the initial rise of the intensity, is available for G-band data for each bakeout after 1 February 2008 (after the third bakeout). We apply the empirical model given by Equation (26) to that period. The left panel of Figure 29 is the observed G-band intensity enhancement after the sixth bakeout, and the right panel shows the thickness of contaminant on the CCD derived from the model. The orange line in the right panel shows the linear least-square fit

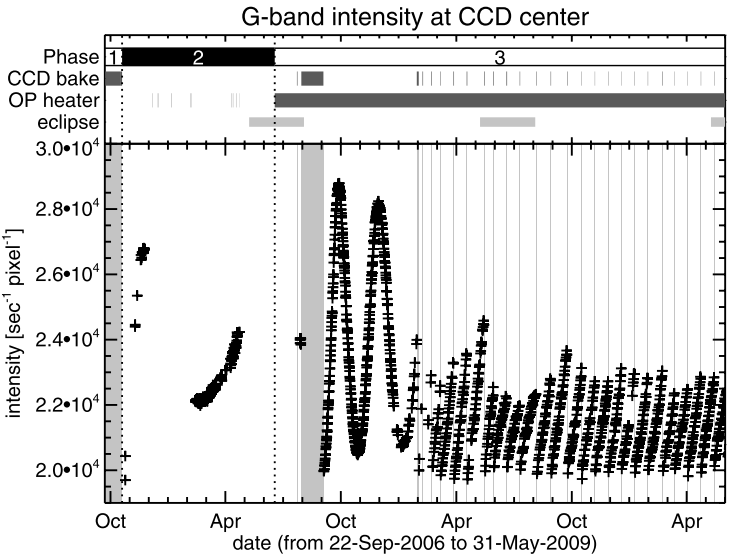

Figure 28 Temporal evolution of the G-band intensity monitored with 512 × 512 pixels at the center of the CCD.

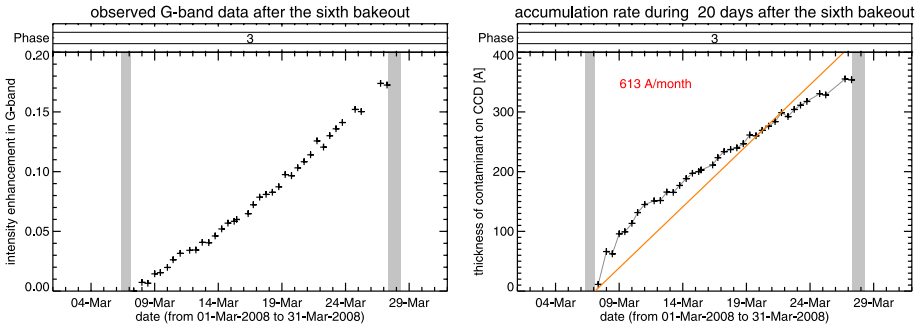

Figure 29 G-band data (left panel) and estimated thickness of the contaminant on the CCD (right panel) after the sixth bakeout.

to the thickness, which yields an accumulation rate of contaminant on the CCD of about 613 Å month^{-1}, where 30 days are taken as one month, unless otherwise noted. In this article, we assume a constant accumulation rate for the contaminant between two successive bakeouts.

We note that the X-ray intensity ratio and the G-band intensity recovered to almost the same level after each CCD bakeout as seen in Phase 3 in the bottom panel of Figures 8 and 28, respectively. This suggests that after each bakeout the contaminant reduces to the same thickness. Furthermore, the recovered G-band intensity in Phase 3 is consistent with the G-band intensity taken just after the end of Phase 1 (until which we expect no contaminant on the CCD due to continuous CCD bakeout since launch). Hence, we conclude that this "same thickness" is actually zero.

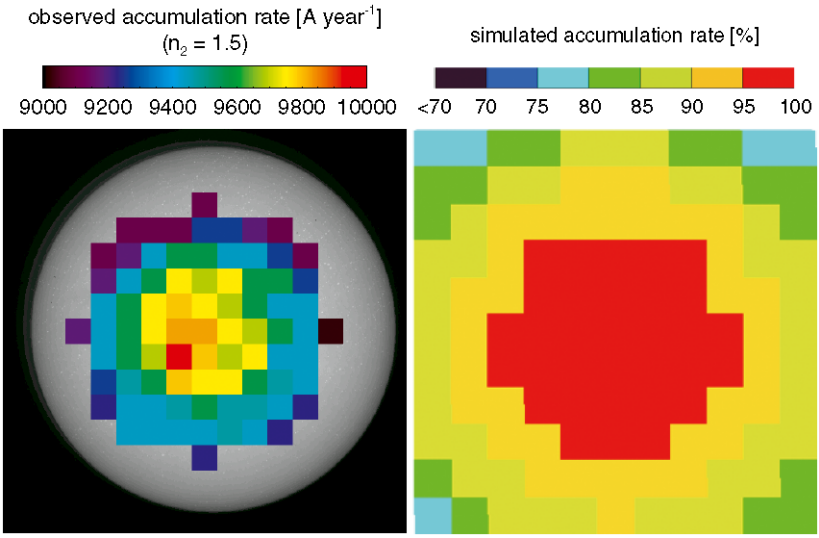

Figure 30 Observed and simulated spatial distribution of the contaminant across the CCD. The left panel is the observed accumulation-rate map with G-band intensity oscillation. The background is a full-Sun (synoptic) image in G-band. The image size is the full CCD area (2048 × 2048 pixels). Each colored box corresponds to 128 × 128 pixels on the CCD. The right panel shows the simulated accumulation-rate map under the condition that the sources of contaminant are located in the forward direction from the CCD. The simulated area in the right panel is also the full CCD area.

Table 7 in Appendix C summarizes the thus-derived accumulation rate of the contaminant between each bakeout, and Figure 6 indicates the temporal evolution of the contaminant thickness on the CCD. The similar plots to Figure 29 after all bakeouts are distributed with Solar Software (SSW) as SSW_DIR/hinode/xrt/idl/response/contam/xrt_contam_on_ccd.pdf, where SSW_DIR indicates the SSW directory in your environment. This file and database of the contaminant thickness will be regularly updated as the CCD is baked out repeatedly.

B.2.3. Spatial Distribution of the Contaminant Across the CCD

To monitor the accumulation rate of the contaminant on the CCD with the G-band data, we have used the 512 × 512 pixels at the center of the CCD. On the other hand, when looking into the fine structure of the contaminant accumulation for the entire imaging area of the CCD, we note that there is certain spatial distribution of the accumulation rate of contaminant across the CCD (see the left panel of Figure 30). The accumulation rate decreases going toward the edges of the CCD from its center. The difference of accumulation rate between the CCD center and outermost area in the left panel of Figure 30 is about 10%.

By building a numerical contamination model in which the geometry and temperature of the structures around the CCD have been incorporated, Urayama *et al.* (2008) studied the expected spatial distribution of contaminants accumulated on the CCD (see the right panel of Figure 30). The resultant distribution was quite similar to the observed one (see Figure 30) when the contaminants come from the forward direction of the CCD, while it was not when the contaminants come from the side of the CCD where the pre-amplifier unit for the CCD is located. The similarity is seen not only in the distribution of the contaminant, but also in a relative difference in the accumulation rate of about 10% between the CCD

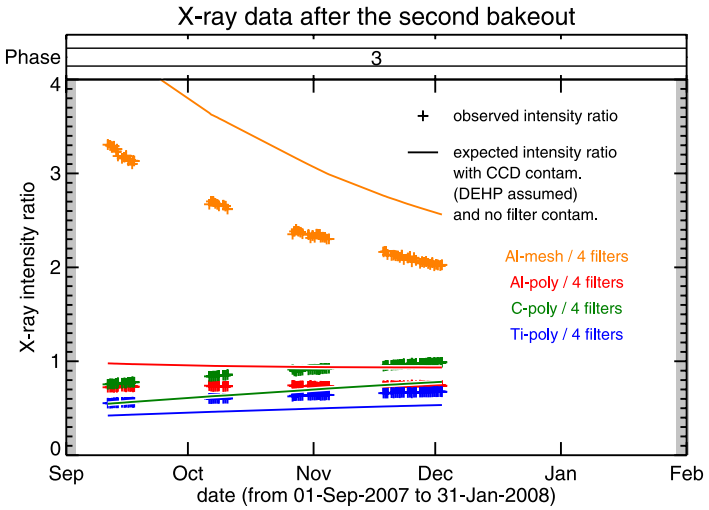

Figure 31 Observed and expected X-ray intensity ratio after the second CCD bakeout in the case of no contaminant on focal-plane analysis filters.

center and the outermost area in the observed data (left panel of Figure 30). Since the edge of the CCD is located outside the solar disk (see the left panel of Figure 30) with synoptic G-band exposure, we cannot measure the accumulation rate at the edges of the CCD. However, on the basis of the comparison between the results of observation and numerical simulation, we conclude that the difference of accumulation rate between the CCD center and its edges is about 20%.

B.3. Analysis of Contaminant with X-Ray Data

Next, we examine whether the decrease in quiet-Sun X-ray intensity shown in Figure 8 is consistent with the effect of the contaminant accumulated on the CCD whose thickness is derived from G-band data. For this analysis, we used data sets in the period between the second and third bakeouts (in Phase 3), because of the availability of data sets both in G-band and in X-rays.

Plus signs in Figure 31 indicate the temporal evolution of quiet-Sun intensity ratios after the second CCD bakeout made from sets of simultaneously taking four filter images: Al-mesh, Al-poly, C-poly, and Ti-poly. In order to remove a possible variation of the emission measure in different quiet-Sun regions, each intensity was normalized by the geometric mean of intensities observed with the four filters,

$$(I_{\text{Al-mesh}} \times I_{\text{Al-poly}} \times I_{\text{C-poly}} \times I_{\text{Ti-poly}})^{1/4}, \tag{28}$$

where I_{filter} is the X-ray intensity with each filter. Data points in this plot were obtained from full-Sun images showing no active regions in order to remove the effect of scattered light from active regions. Data gaps in this plot are due to the appearance of active regions. In the plot, a significant decrease in the intensity ratio with the Al-mesh filter and a slight increase in those with the other three filters are clearly seen. We consider these changes to be caused by the effect of accumulating contamination, which absorbs X-rays. Note that the increase

Table 5 Candidates of contaminant material.

#	Material	Density	Refractive index
1	diethylhexyl phthalate[a] (DEHP) $C_{24}H_{38}O_4$	0.986 g cm^{-3}	$n = 1.5$[b]
2	tetramethyl tetraphenyl trisiloxane[c] (MPS) $C_{28}H_{32}O_2Si_3$	1.07 g cm^{-3}	$n = 1.6$[d]
3	polydimethylsiloxane[c] (PDMS) $(C_2H_6OSi)_n$	0.971 g cm^{-3}	$n = 1.4$[e]

[a]DEHP is a plasticizer.

[b]catalog of chemical reagent by Wako Pure Chemical Industries, Ltd.

[c]MPS and PDMS are classified Siloxane.

[d]Osantowski (1982).

[e]catalog of TORAY Silicone, Ltd.

in intensity ratio with Al-poly, C-poly, and Ti-poly filters is due to the large decrease in intensity with the Al-mesh filter (see the top panel of Figure 8).

Next, we calculate the expected intensity of the quiet Sun observed with the contaminant-accumulated CCD using the differential emission measure (DEM) at the quiet Sun. From Equation (1), the effective area of XRT [$A_{\rm eff}^{\rm contam}$], including the effect of contamination, is given by

$$A_{\rm eff}^{\rm contam} = A_{\rm eff} \times \mathcal{T}_{\rm contam}, \tag{29}$$

where $\mathcal{T}_{\rm contam}$ is the transmission of the contaminant. For the DEM of the quiet Sun, we adopted the DEM profile derived by Brooks and Warren (2006) with the assumption that the profile of the quiet-Sun DEM is almost constant in time. The procedure for deriving the expected intensity from the DEM thus assumed is detailed in Appendix D.2. We will discuss the effect of the difference in the DEM model on our analysis in Appendix K.4.

By adopting the thickness of the contaminant on the CCD (from the G-band data) for deriving $\mathcal{T}_{\rm contam}$, the combination of $A_{\rm eff}^{\rm contam}$ and the DEM profile gives the expected profiles of the intensity ratio, which are overlaid in Figure 31. (The chemical composition of DEHP (diethylhexyl phthalate: $C_{24}H_{38}O_4$) is adopted as the contaminant on the CCD for making the profiles in the figure; see Appendix B.3.1 for details.) The figure clearly shows that the observed and expected X-ray intensity ratios are inconsistent with each other. Especially, in addition to the large deviation in the Al-mesh filter, although the expected intensity ratio with the Al-poly filter is larger than that for the C-poly filter, the observed intensity ratios with these two filters are contrary to expectation. In the following, we investigate the cause of this inconsistency.

B.3.1. X-ray Analysis for Phase 3

In order to solve the intensity discrepancy between Al-poly and C-poly filter, in this section, we characterize the contaminant accumulated on each FPAF. We note that contamination on each FPAF is the only possible candidate to account for this discrepancy, because the other optical elements are jointly used for the data taken with others of the X-ray filters.

Table 6 Fitting parameter to observed X-ray data.

Parameter	Examined range	Expected value	Best-fit value
contaminant	DEHP, MPS, or PDMS	–	DEHP
contam. on Al-mesh filter	0 – 4000 Å	–	1200 Å
contam. on Al-poly filter	0 – 4000 Å	–	2900 Å
contam. on C-poly filter	0 – 4000 Å	–	500 Å
contam. on Ti-poly filter	0 – 4000 Å	–	400 Å
metal thick. of pre-filter	1000 – 2000 Å	1538 Å[a]	1550 Å[b]
oxide thickness[c]	0 – 75 Å	< 75 Å[d]	75 Å / 0 Å[e]

[a]This value is based on the certification sheet (see Figure 3 and Table 1).

[b]The expected metal thickness when it was fabricated. At fabrication, the metals had not oxidized at all. The on-orbit pure and oxidized-metal thicknesses are shown in Table 1.

[c]The oxide thickness of metal filters. We examine it for open side and for polyimide side.

[d]The oxide thickness of well-oxidized Aluminum filter is 150 Å (Powell *et al.*, 1990). Hence, the expected oxide thickness for one side (open side) is < 75 Å.

[e]Best-fit value of "oxide thickness for open side" / "oxide thickness for polyimide side".

As discussed in Appendix B.1, it is expected that there was no additional accumulation of contaminant on the FPAFs in Phase 3. As the period shown in Figure 31 belongs to Phase 3, the data shown in the figure are suitable for identifying the thickness of the contaminant on each FPAF. Moreover, using these data, we can also identify the properties of contaminant material, *i.e.* the chemical composition, density, and refractive index of contaminant material, because the transmission of the contaminant $[\mathcal{T}_{\rm contam}]$ in Equation (29) depends on the above properties, as shown by Equation (20), where the thickness $[d]$ of the contaminant is estimated with the refractive index of the contaminant material (see Equation (25)), and the attenuation length $[l_{\rm att}(\lambda)]$ is determined by the chemical composition and density.

Before proceeding to the above calibration, we first try to identify the possible material of the contamination. We picked three candidate materials, which are listed in Table 5. These three candidates are widely used for satellites, and they are well known to be possible sources of contamination: DEHP (diethylhexyl phthalate: $C_{24}H_{38}O_4$) is the representative of a long-chain organic compound which consists of carbon, hydrogen, and oxygen. MPS (tetramethyl tetraphenyl trisiloxane: $C_{28}H_{32}O_2Si_3$), and PDMS (polydimethylsiloxane: $(C_2H_6OSi)_n$) are long-chain organic compounds that include silicon. Although these contaminant candidates can be classified into two types, namely a long-chain organic compound without and with silicon, their density and refractive index are almost the same (1 g cm^{-3}) and 1.5, respectively. We note that, although DEHP is not used in the XRT, if the actual contaminant material is a long-chain organic compound without silicon, the chemical composition, density, and refractive index would be similar to DEHP. Hence, in our analysis, we refer to DEHP as the representative of a long-chain organic compound without silicon.

We obtained filter parameters that best fit the observed intensity ratio. The parameters and the range examined for the fitting are summarized in Table 6. The examined range of the contamination thicknesses accumulated on the four thin FPAFs is 0 – 4000 Å, since a contaminant thickness larger than 4000 Å gave results that are inconsistent with the observed data. In this calibration, we cannot investigate the contamination thickness on thicker FPAFs, because the thicker FPAFs cannot observe the quiet Sun well enough. The metal thickness of the pre-filter was examined in the range of 1000 – 2000 Å, *i.e.* approximately covering the

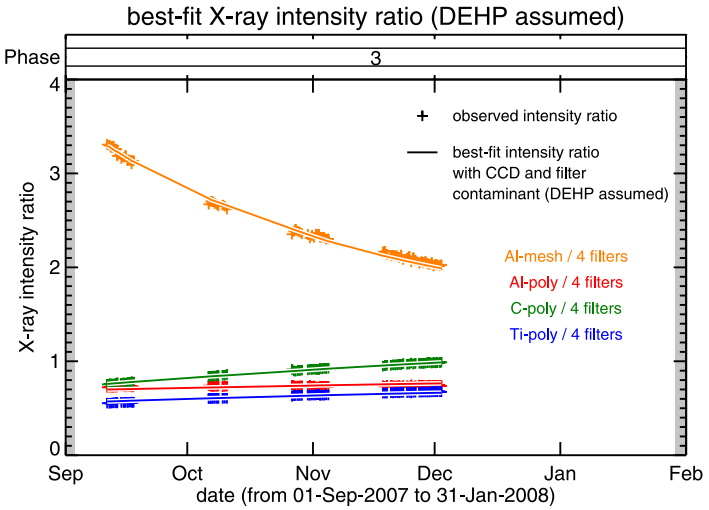

Figure 32 Best-fit X-ray intensity ratio after the second CCD bakeout, where for this analysis we have taken the material to be similar to DEHP.

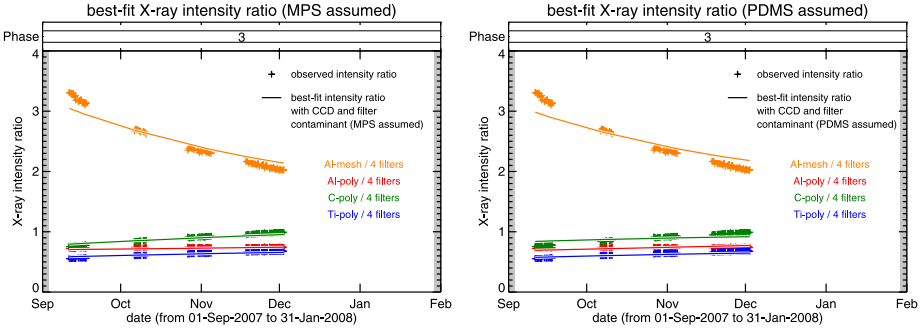

Figure 33 Best-fit X-ray intensity ratio after the second CCD bakeout, where the materials of the contaminant are assumed to be MPS (left panel) and PDMS (right panel).

range of ± 500 Å from the thicknesses provided by the manufacturer. According to Powell *et al.* (1990), the oxide thickness of a well-oxidized, stand-alone aluminum filter is 150 Å in total for both sides, *i.e.* 75 Å for each side. Hence, we examine an oxide thickness for the open side of a filter in the range of $0-75$ Å under the assumption that any metal filters were oxidized with the same thickness. Some of the FPAFs have a support made of polyimide. We also investigated the oxide thickness for the polyimide side in the range of $0-75$ Å under the above assumption.

Figure 32 shows the estimated X-ray intensity ratio from the best-fit parameters summarized in Table 6, including material for the contaminant, which was identified to be consistent with DEHP, namely the representative material of a long-chain organic compound without silicon. The area-weighted average thickness of the pre-filter was calibrated to be 1550 Å, which is the expected metal thickness when it was fabricated. At fabrication, the metals had not oxidized at all. This value is very close to the value of 1538 Å derived from

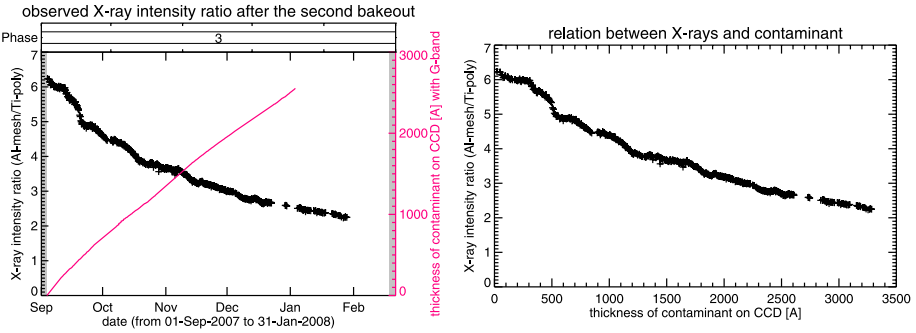

Figure 34 Left panel: Observed X-ray intensity ratio (black +) and measured thickness of the contaminant on the CCD with G-band (magenta line) after the second bakeout; right panel: relation between X-ray intensity ratio and thickness of contaminant on the CCD after the second bakeout.

the manufacturer-supplied information on the thickness for each piece of the pre-filters (see Figure 3). Hence, considering the oxidization (using Equation (56) of Appendix I), the on-orbit pure and oxidized-metal thicknesses of a pre-filter are calibrated to be 1492 Å and 75 Å, respectively, as summarized in Table 1. The calibrated the thickness of the contaminant on each FPAF turned out to be different. The thickness of contaminant on the Al-poly filter was identified to be 2900 Å, which was the thickest. We will see in Appendix B.3.3 that this difference in thicknesses is consistent with the frequency of filter usage.

Figure 33 indicates the difference in the fit among different candidates for the contaminant material. The left panel shows the best-fit result with MPS, while the right panel shows the PDMS case. Clearly, these materials are not able to account for the measured profiles, especially that for the Al-mesh filter. The difference in chemical compositions among the candidate materials for contamination most affect the transmission at longer wavelength X-rays, hence the intensity with the thinnest Al-mesh filter. This results in the situation that the Al-mesh profiles show the largest sensitivity to the different candidates. Furthermore, for MPS and PDMS, the metal thickness of the pre-filter which gives the best fit to the measurements turned out to be 1000 Å and 1050 Å, respectively. These thicknesses are unlikely because of a significant deviation from the averaged pre-filter thickness measured by the manufacturer (1538 Å). Hence, we can conclude that the contaminant material is a long-chain organic compound whose characteristics, namely the chemical composition, density, and refractive index, are similar to DEHP. We will discuss this identified contaminant material in Appendix K.1.

B.3.2. X-Ray Analysis for Phase 2 – Contamination on the CCD

In Appendix B.2, we established the method to monitor the contaminant on the CCD with the G-band data. Using this method, we can measure the thickness of the contaminant on the CCD for the Phase 3 period. However, for Phase 2, we cannot apply this method because there are not enough G-band data. Instead, we rely on the X-ray data for investigating the accumulation of contaminant on the CCD.

For this purpose, let us first derive the relationship between G-band and X-ray data for the period after the second bakeout (which took place in Phase 3) where both data sets are available. The measured thickness of the contaminant on the CCD with the G-band data is shown in red in the left panel of Figure 34. In this panel, the observed X-ray intensity ratio

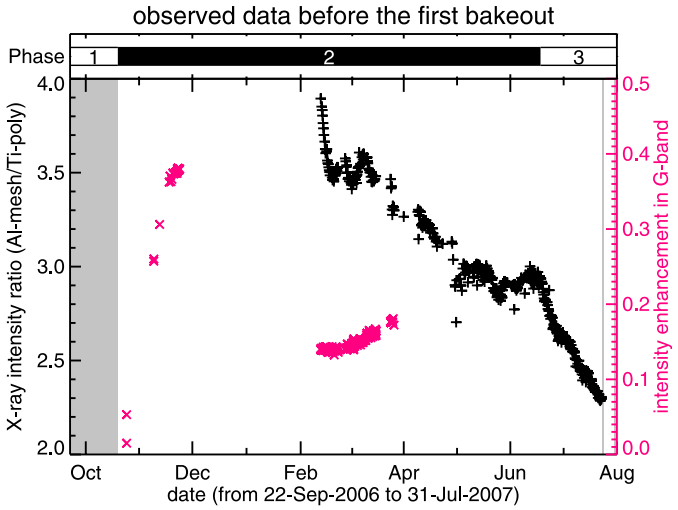

Figure 35 Observed X-ray intensity ratio (black +) and intensity enhancement in G-band (magenta ×) before the first bakeout.

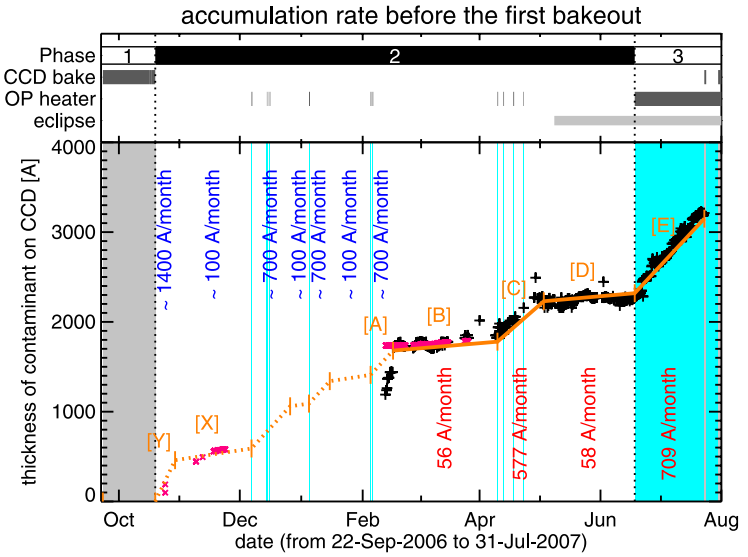

Figure 36 Accumulation rate of contaminant on CCD before the first bakeout. This rate is derived from two kinds of data set: the X-ray intensity ratio between Al-poly and Ti-poly filters (black +), and the G-band intensity (magenta ×). The orange solid and dotted lines show the measured and expected thickness of contaminant on the CCD, respectively. The measured and expected accumulation rates are also shown with red and blue characters. The [A] – [E], [X], and [Y] show the classified periods from the profile of contaminant thickness (orange lines).

between Al-mesh and Ti-poly filters is also shown in black. Using these data, we obtain the relation to convert the X-ray intensity ratio to the thickness of the contaminant on the CCD, which is shown in the right panel. As demonstrated in Appendix B.1, the contaminant on

FPAFs is constant in Phase 3. Note that the necessary condition for applying the right-panel relation of Figure 34 (hereafter, the "XSC relation", where XSC stands for X-ray-suggested CCD contamination) is that the contaminant thicknesses on the FPAFs are the same as those in Phase 3.

Now, let us check whether the above necessary condition is satisfied in Phase 2 too. Figure 35 shows the temporal evolution of X-ray intensity ratio (black $+$) and intensity enhancement in the G-band (red $\times$) observed before the first CCD bakeout. Note that the entire period of Phase 2 is contained in the plot. By applying the XSC relation to the observed X-ray intensity ratio, we estimated the thickness of the contaminant on the CCD as shown by the black pluses in Figure 36. Note that the thickness was estimated by assuming the existence of contaminant on the FPAFs whose thicknesses are identical to those in Phase 3. The thickness of the contaminant on the CCD derived with the G-band data is also plotted in Figure 36 in red crosses. This profile shows some trends. We classify the profile into A – E, as shown in Figure 36. In periods A, C, and E, the thickness of the contaminant increases at a certain rate, but in B and D, the thickness is almost constant. As discussed earlier, the variation of the G-band data is solely affected by the contaminant on the CCD, not by the contaminant on the G-band filter. Hence, using the G-band data, we can monitor the contaminant on the CCD independently. The magenta crosses in Figure 36 are the estimated thicknesses of the contaminant on the CCD from the G-band data. As clearly seen, in period B the thickness of the contaminant on the CCD estimated from the X-ray intensity ratio (black $+$) is consistent with that derived with the G-band data (magenta $\times$). This suggests that the above necessary condition of the XSC relation is valid. Now that we know that the thicknesses of contaminant on the FPAFs in period B are the same as those in Phase 3 and that it is not likely that the thickness would decrease in any certain period (note that they did not decrease even with a FPAF temperature $\approx +20$°C in Phase 3), we can conclude that the thicknesses of the contaminant on the FPAFs are unchanged after (including) period B (after (including) the "late period" of Phase 2 in Figure 5). This means that, after period B, the thickness of the contaminant on the CCD can be measured from the XSC relation as shown by the black $+$. The solid orange lines after period B show a linear fit to the measured thickness (black $+$).

For the interval after period B, there are episodes of rapid accumulation of contaminant on the CCD (periods C and E), while the rest do not show much accumulation (periods B and D). We note that the behavior of the accumulation of the contaminant on the CCD is closely related to the status of the operational heater, as we now describe.

- From turning on the operational heater to about ten days after turning off, which we call the "contamination period" (CP), the contaminant rapidly accumulated on the CCD at a rate of < 700 Å month^{-1} (periods C and E, but see comments below). The periods when the operational heater was on are indicated by blue areas in Figure 36.
- From about ten days after turning off to the next turning on, which we call a "small-contamination period" (SCP), the accumulation rate is small, namely < 100 Å month^{-1} (periods B and D).

Hereafter, we call this relationship the "ODC relation" (operational heater driven contamination). This relationship suggests that the contamination is triggered by the operation of the operational heater.

So far, we have seen that the XSC relation can be applied for the period from period B ("late period" of Phase 2 in Figure 5). Let us check if this relation holds for the rest of Phase 2, namely the period before (including) period A on Phase 2 (the "early period" of Phase 2). From Figure 23, we see the following trends in the temperatures.

i) Until March 2007, when the operational heater was on, the temperature around the FPAFs was ≈+20°C and at the CCD ≈−65°C. When the operational heater was off, the temperature around the FPAFs was ≈+5°C and at the CCD ≈−70°C.
ii) From March 2007 to May 2007, the temperatures around the FPAFs and at the CCD increased a little due to the increased albedo of the Earth toward the beginning of the eclipse season.
iii) In the eclipse season (from May 2007), the temperatures around the FPAFs decreased due to the decreased time of solar illumination, while the temperature at the CCD increased due to the increased Earth albedo.

These changes in the temperatures were negligible for the accumulation rate of the contaminant on the CCD, since the measured accumulation rates were almost constant during periods B and D, which correspond to the above trends *i*) – *ii*) and trend *iii*), respectively. Therefore, we expect that the ODC relation is also applicable to the period before (including) period A.

There are not sufficient X-ray nor G-band data for the interval between periods X and A (the "early period" of Phase 2 in Figure 5) to measure the contaminant thickness on the CCD. Therefore, we rely on the ODC relation for this interval and check if the relation consistently connects the periods from A back to X. To apply the ODC relation, we assumed that the contaminant accumulated on the CCD at a rate of 700 Å month^{-1} for CP, while this rate was 100 Å month^{-1} for the SCP, as shown by dotted orange lines in Figure 36. In performing the extrapolation with the ODC relation, we started from period B and backwards toward period X. Note that the applied rates are somewhat larger than the measured rates in periods C (580 Å month^{-1}) and periods A and D (60 Å month^{-1}). This is because we expect that the accumulation rate in the early period of Phase 2 would be higher than the late period in Phase 2. Note here that the difference in contaminant thicknesses at the beginning of period X is small (≈ 200 Å) even if we adopt the pair of values of 580 Å month^{-1} and 60 Å month^{-1}. For period Y, which is the interval between the end of Phase 1 (until which we expect no contaminant on the CCD due to the continuous CCD bakeout since launch) and the beginning of period X, a constant accumulation rate of the contaminant on the CCD was assumed. We note that the duration of period Y is determined to be ten days, as shown in Figure 36, since we confirmed that the X-ray intensity in the quiet Sun observed with the Al-poly filter was almost constant for the period when more than ten days passed after the beginning of Phase 2. Note that there are no data available on the first ten days. The estimated accumulation rate in period Y is ≈ 1400 Å month^{-1}. This high rate might be caused by the high temperature of the telescope in Phase 1. The temperature of the front-end portion of the telescope turned out to be significantly higher than the temperature predicted before launch. We guess that in Phase 1 a great deal of contaminant was created and filled the inside of the telescope. This contaminant rapidly accumulated on the CCD after the CCD bake heater was turned off (in the beginning of Phase 2, *i.e.* period Y).

Finally, let us check whether the expected contaminant thickness on the CCD is reliable. In periods X and Y, the expected thickness (dotted orange line) is consistent with the contaminant thickness measured with the G-band data (magenta ×). This result strongly supports our expectation. As discussed above, now we understand the accumulation of contaminant on CCD in all periods (see Figure 6).

We note that in period A there is a discrepancy between the contaminant thickness on the CCD derived with the ODC extrapolation (dotted orange line) and the thickness derived with the XSC relation (black pluses +). This discrepancy will be discussed in the next section.

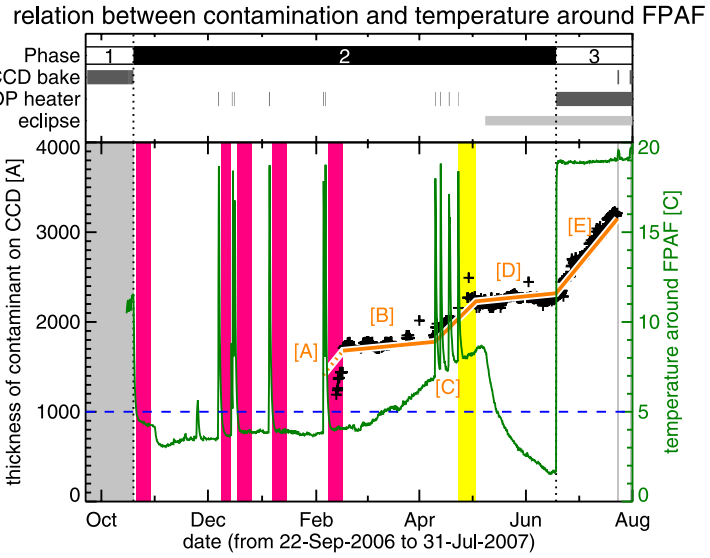

Figure 37 Relation between the temperature around the focal-plane analysis filter (green line) and estimated thickness of contaminant on the CCD with X-ray intensity ratio (orange line). The contaminant would accumulate on FPAFs in the "cool contamination periods" (CCPs) shown in magenta. While, in the "warm contamination period (WCP)" shown in yellow, the contaminant would not accumulated. The blue dashed line indicates the boundary temperature between CCP and WCP (5°C).

B.3.3. X-Ray Analysis for Phase 2 – Contamination on the FPAFs

From the discussion in Appendix B.1 and Appendix B.3.2, we know the following for the contamination on the FPAFs:

- The contaminant did not accumulate in Phase 3.
- In Phase 2, the contaminant did not accumulate after the beginning of period B.

Hence we conclude that the FPAFs contaminant must have accumulated by the end of period A.

Figure 37 shows temporal profiles of the temperature around the FPAFs and the estimated thickness of the contaminant on the CCD. In period A, there is a discrepancy between the thickness of contaminant on the CCD derived with the ODC relation (dotted orange line) and the thickness derived with the XSC relation (black pluses +). Given the successful ODC extrapolation described in the previous section, this discrepancy most likely implies that the thickness of contaminant on the FPAFs that we assumed (being the same as those in Phase 3) for applying the XSC relation in period A is not correct. In other words, the contaminant accumulated on the FPAFs' at least in period A.

Next, we investigate why the FPAFs contamination took place in period A while it did not in period C. Both periods A and C are "contamination periods (CPs)", as defined in Appendix B.3.2. As we mentioned, in these CPs, the contaminant accumulated on the CCD. The difference between periods A and C is the temperature around the FPAFs, as shown in Figure 37. The temperature around the FPAF in period A (about 4°C) was lower than in period C (about 8°C). We classify the CPs into two according to the temperature around the FPAFs: for the periods when the temperature is lower than $\approx 5-8$°C, we call these

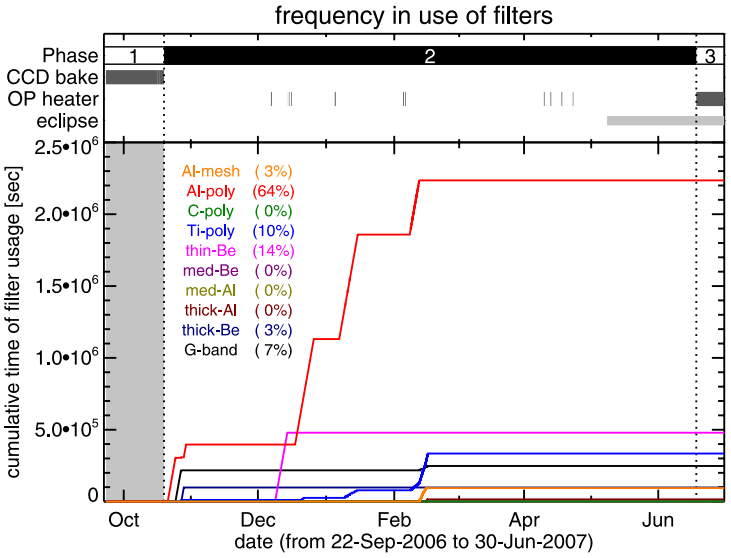

Figure 38 Cumulative time of filter usage during the "cool contamination periods" colored by magenta in Figure 37. The final percentage of cumulative time for each filter is described in parentheses, where the Al-poly filter has the largest cumulative time.

Figure 39 Modeled accumulation rate of contaminant on each focal-plane analysis filter. x and y are the rates of the filters mounted on Filter Wheel 1, and z and w are the rates of the filters on Filter Wheel 2.

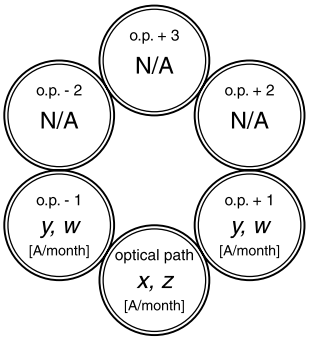

a "cool contamination period" (CCP), while we call them a "warm contamination period (WCP)" for the rest of the CP. The difference in temperature leads to the hypothesis that the contaminant, generated by turning on the operational heater, accumulated on the cool FPAFs in CCPs. On the other hand, the high temperature around the FPAFs in the WCPs prevents the contaminant from accumulating. If this hypothesis is correct, the contaminant accumulated on the FPAFs in the five CCPs is shown in magenta in Figure 37. On the other hand, in the WCP, shown in yellow, the contaminant did not accumulate on the FPAFs. Although the difference of temperature around the FPAFs is only indirect evidence, there is not any reasonable timing for the FPAFs contamination other than the CCPs. On the basis of this result, we expect that the contaminant did not accumulate on the FPAFs in Phase 1, since the temperature around the FPAFs was higher than 10° C in that phase.

As we identified that the CCPs are the periods when the FPAFs suffered from the contamination, next we examine the amount of the contaminant accumulated on each FPAF

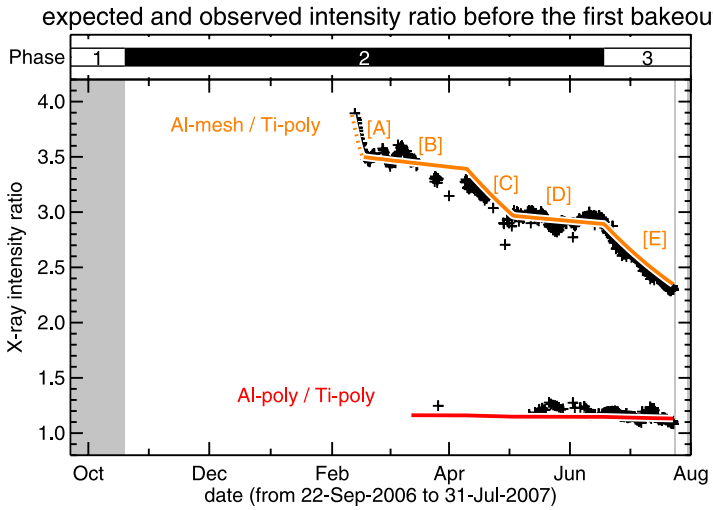

Figure 40 Comparison between the expected (colored lines) and observed (black +) X-ray intensity ratio. The expected intensity ratio is calculated with the calibrated thicknesses of the filters and contaminant.

as a function of time for each CCP. Figure 38 gives the frequency in use of FPAFs during the CCPs. The vertical axis shows the cumulative time for each filter located on the optical path. We expect that this cumulative time should have a positive, linear correlation with the thickness of the contaminant for each FPAF. Hereafter, we call this relationship the "USF relation" where USF stands for FPAF-usage-suggested FPAF contamination. To estimate the thickness, we apply the following simple model: we set the accumulation rates of contaminant on the FPAFs to be x, y, z, and w, as shown in Figure 39. Here, x and z are the accumulation rates on the filters located on the optical path (o.p.), while y and w are the rates on the filters located just next to the optical path (o.p. ± 1, in Figure 39). We assume that no contaminant accumulated on the filters far from the optical path (o.p. ± 2 and o.p. $+3$). Using these accumulation rates, we can express the thickness of contaminant accumulated on each filter d as follows:

$$d_{\mathrm{FPAF1}} = x \times t^{\mathrm{o.p.}}_{\mathrm{FPAF1}} + y \times \left(t^{\mathrm{o.p.}+1}_{\mathrm{FPAF1}} + t^{\mathrm{o.p.}-1}_{\mathrm{FPAF1}}\right), \tag{30}$$

$$d_{\mathrm{FPAF2}} = z \times t^{\mathrm{o.p.}}_{\mathrm{FPAF2}} + w \times \left(t^{\mathrm{o.p.}+1}_{\mathrm{FPAF2}} + t^{\mathrm{o.p.}-1}_{\mathrm{FPAF2}}\right), \tag{31}$$

where $t^{\mathrm{o.p.}}$ and $t^{\mathrm{o.p.}\pm 1}$ are the cumulative times when the filter is located on and next to the optical path, respectively, and the subscripts of FPAF1 and FPAF2 indicate the FPAFs mounted on FW1 and FW2, respectively. On the basis of the estimated thicknesses of the contaminant on the four thin filters (Al-mesh, Al-poly, C-poly, and Ti-poly) in Phase 3 (see Table 6) and the cumulative time [t] of filter usage shown in Figure 38, we derive the accumulation rate of the contaminant on the FPAFs as follows: $x = 3220$ Å month^{-1}, $y = 480$ Å month^{-1}, $z = 2080$ Å month^{-1}, and $w = 1000$ Å month^{-1}. A result of $x > y$ and $z > w$ is likely, because the filter wheels are contained in a closed structure which has holes for the optical path, and the contaminant may have come to the filters through such holes.

So far, we derived coefficients of proportionality [x, y, z, and w] in Equations (30) and (31) using the final thicknesses of the contaminant for the four thin filters at the end of

Phase 2 (beginning of Phase 3). If the coefficients thus derived are correct, Equations (30) and (31) should give a correct contaminant thickness for each FPAF at any instant in Phase 2. Let us now check if this is the case. Figure 7 indicates the temporal evolution of the contaminant thickness on the FPAFs from Equations (30) and (31), while that for the CCD is shown in Figure 6. Figure 40 shows a comparison between the observed intensity ratios in X-rays and those expected using the contaminant thickness thus derived. Note that the contaminant accumulated on both FPAFs and CCD in period A, while it did so only on the CCD in periods B – E. The close match between observed and expected intensity ratios strongly suggests that the estimate of the contaminant thicknesses on the FPAFs with Equations (30) and (31) are reasonable ones. We now have a reasonable estimate on the thickness of the contaminants not only on the CCD but also on the FPAFs throughout the entire period since launch.

We note that, since not enough X-ray signal is acquired from the quiet Sun with the thicker filters, the contaminant thicknesses on the thicker filters have not been directly measured. This is in contradiction to the thinner filters. Hence, the estimate of the thickness of the contaminant on the thicker filters with Equations (30) and (31) may be less accurate than the thinner filters, in that the verification with X-ray data is not possible. Nevertheless, we do not see any reason for Equations (30) and (31) not to be applicable to the thicker filters. Furthermore, the effect of contamination on the thicker filters is much smaller than on the thinner filters, because only short-wavelength X-rays can pass through thicker filters and the effect of contaminant is small or negligible for such short-wavelength X-rays. Hence, our results can be applied to quantitative analyses with the XRT data.

Appendix C: CCD Bakeout

The XRT team decided that 800 Å of contaminant thickness should be the maximum acceptable contamination. The XRT team regularly performs CCD bakeout every three to four weeks to remove the contaminant from the CCD. Table 7 is the summary of CCD bakeout from the launch of *Hinode* (22 September 2006) to the end of April 2009.

Appendix D: Estimate of Data Number and Intensity Detected by XRT

We explain the method to estimate the expected data numbers (DNs) when XRT observes the X-ray spectra from an X-ray generator and from the Sun, in order to compare them with the DNs actually detected at XRCF and on orbit, respectively. First of all, we define the meaning of DN and of the intensity in this article. The DN is the dimensionless value which is proportional to the total energy of the incident X-rays into XRT. Meanwhile, the intensity is the DN normalized by the observation time and number of pixels [DN sec^{-1} pixel^{-1}].

D.1. XRCF

When incident X-rays into XRT have a photon-number spectrum of $P(\lambda)$ [cm^{-2} sec^{-1} $\mathrm{Å}^{-1}$], the energy spectrum observed by XRT ($E_{\mathrm{XRT}}(\lambda)$ [eV sec^{-1} $\mathrm{Å}^{-1}$]) is written

$$E_{\mathrm{XRT}}(\lambda) = P(\lambda) \times A_{\mathrm{eff}}(\lambda) \times \frac{hc}{\lambda} \times \frac{1}{e}, \tag{32}$$

where h, c, and e are Planck's constant, the speed of light, and the elementary electric charge, respectively. This incident energy generates electron hole pairs on the CCD. One

Table 7 Bakeout history of XRT.

No.[a]	Bake heater on	Heater off	Interval [days][b]	Contam. rate [Å month^{-1}][c]	Spot [%][d]
−3	22 Sep 2006, 21:39	16 Oct, 07:53	0.1	–	0.00
−2	16 Oct 2006, 09:35	17 Oct, 08:28	0.1	–	0.00
−1	17 Oct 2006, 10:13	19 Oct, 08:12	277.0	–	0.00
1	23 Jul 2007, 09:09	24 Jul, 08:10	6.0	–	–
2	30 Jul 2007, 08:41	3 Sep, 09:12	148.0	730	2.61
3	29 Jan 2008, 08:42	1 Feb, 10:01	6.0	1866	5.48
4	7 Feb 2008, 08:50	8 Feb, 07:52	13.0	716	–
5	21 Feb 2008, 08:19	22 Feb, 08:22	13.0	747	5.25
6	6 Mar 2008, 08:18	7 Mar, 02:20	20.2	613	–
7	27 Mar 2008, 08:15	28 Mar, 08:12	20.0	656	–
8	17 Apr 2008, 09:10	18 Apr, 10:00	27.0	569	5.26
9	15 May 2008, 09:18	16 May, 09:22	13.0	801	5.25
10	29 May 2008, 09:50	30 May, 10:00	19.9	506	5.27
11	19 Jun 2008, 08:14	20 Jun, 10:00	20.0	481	5.28
12	10 Jul 2008, 09:47	11 Jul, 04:00	25.2	432	5.24
13	5 Aug 2008, 08:33	6 Aug, 04:00	22.3	510	5.23
14	28 Aug 2008, 10:05	29 Aug, 04:00	25.2	514	–
15	23 Sep 2008, 09:53	24 Sep, 04:00	22.3	522	5.24
16	16 Oct 2008, 11:06	16 Oct, 23:07	20.4	567	5.24
17	6 Nov 2008, 09:29	6 Nov, 21:29	20.5	507	5.23
18	27 Nov 2008, 10:11	27 Nov, 22:17	20.4	546	5.23
19	18 Dec 2008, 08:33	18 Dec, 20:39	20.5	544	5.23
20	8 Jan 2009, 09:24	8 Jan, 21:23	20.5	547	5.23
21	29 Jan 2009, 08:29	29 Jan, 21:23	22.5	487	5.22
22	21 Feb 2009, 08:24	22 Feb, 02:26	18.3	527	5.22
23	12 Mar 2009, 09:19	12 Mar, 21:20	20.5	499	5.21
24	2 Apr 2009, 09:16	2 Apr, 21:25	20.5	577	5.23
25	23 Apr 2009, 09:13	23 Apr, 21:14	–	–	5.18

[a]Bakeouts from − 3 to − 1 were preformed before first light (23 October 2006). We count the bakeout number after the first light.

[b]Interval from this bakeout to next bakeout.

[c]Accumulation rate of contaminant on the CCD from this bakeout to the next bakeout. This rate is measured from G-band intensity oscillation. The details are described in Appendix B.2.2.

[d]The ratio of contamination spot area to the full CCD area. The details of the spot are described in Appendix G.

electron – hole pair is generated by 3.65 eV. The data number [DN] detected by the XRT CCD is expressed as

$$\mathrm{DN} = t \times \int E_{\mathrm{XRT}}(\lambda) \times \frac{1}{3.65} \times \frac{1}{G}\,\mathrm{d}\lambda, \tag{33}$$

where t is the exposure time in units of seconds, and G is the system gain of the CCD camera, which is 57.5 [e DN^{-1}] in the XRT case (Kano *et al.*, 2008). Substituting Equation (32) into (33), we obtain the equation to derive the DN from the photon-number spectrum [$P(\lambda)$] to be

$$\mathrm{DN} = t \times \int P(\lambda) \times A_{\mathrm{eff}}(\lambda) \times \frac{hc}{\lambda} \times \frac{1}{e \times 3.65 \times G}\,\mathrm{d}\lambda. \tag{34}$$

D.2. On Orbit

Using the effective area (see Figure 9), we can estimate the intensity [I] detected by the XRT, *i.e.* how much data number [DN] is generated in one pixel of XRT CCD in one second, when XRT observes the Sun whose photon-number spectrum is $P_{\odot}(\lambda)$ [cm^{-2} sec^{-1} sr^{-1} Å^{-1}]. The estimated I [DN sec^{-1} pixel^{-1}] is given by

$$I = \int P_{\odot}(\lambda) \times S \times \frac{A_{\mathrm{eff}}(\lambda)}{R^2} \times \frac{hc}{\lambda} \times \frac{1}{e \times 3.65 \times G}\,\mathrm{d}\lambda, \tag{35}$$

where S [cm^2] is the solar area detected in one pixel of CCD. A_{eff} and R are the effective area of XRT, and distance from the Sun to the XRT (≈ 1 AU), respectively. Then A_{eff}/R^2 is the solid angle of XRT effective area in units of steradians. The meaning of the other terms is the same as in Equation (34). Considering the geometry of the telescope, the relation of

$$\frac{S}{R^2} = \frac{s}{f^2} \tag{36}$$

is given, where s and f are the area of one CCD pixel (13.5^2 μm^2, see Kano *et al.* (2008)) and the focal length of the XRT (2708 mm, see Golub *et al.* (2007)), respectively. Using this relation, Equation (35) can be rewritten as

$$I = \int P_{\odot}(\lambda) \times s \times \frac{A_{\mathrm{eff}}(\lambda)}{f^2} \times \frac{hc}{\lambda} \times \frac{1}{e \times 3.65 \times G}\,\mathrm{d}\lambda. \tag{37}$$

Using Equation (37), we can derive the intensity observed by XRT. The CHIANTI atomic database (Dere *et al.*, 1997) gives us a photon-number spectrum [$\tilde{P}_{\mathrm{iso}\odot}(\lambda, T)$, cm^{-2} sec^{-1} sr^{-1} Å^{-1}] emitted from an isothermal plasma at a given temperature of T and a unit column emission measure (CEM) of 1 cm^{-5}. The definition of CEM is

$$\mathrm{CEM} \equiv \int n_{\mathrm{e}} \times n_{\mathrm{H}}\,\mathrm{d}l, \tag{38}$$

where n_{e}, n_{H}, and dl are the electron number density [cm^{-3}], the hydrogen number density [cm^{-3}], and unit length along the line-of-sight [cm], respectively. We calculate $\tilde{P}_{\mathrm{iso}\odot}(\lambda, T)$ based on CHIANTI version 6.0.1 (Dere *et al.*, 1997, 2009: which was the latest version, which we utilized) with the ionization equilibrium of chianti.ioneq (Dere, 2007) and the abundance of sun_coronal_ext.abund (Feldman *et al.*, 1992; Landi, Feldman, and Dere, 2002). Replacing $P_{\odot}(\lambda)$ by $\tilde{P}_{\mathrm{iso}\odot}(\lambda, T)$ in Equation (37), we can calculate the so-called "temperature response" [$F(T)$: DN sec^{-1} pixel^{-1}] of the XRT, which is the intensity observed by XRT from a plasma at a given temperature of T and a unit column emission measure of 1 cm^{-5} as

$$F(T) \equiv \int \tilde{P}_{\mathrm{iso}\odot}(\lambda, T) \times s \times \frac{A_{\mathrm{eff}}(\lambda)}{f^2} \times \frac{hc}{\lambda} \times \frac{1}{e \times 3.65 \times G}\,\mathrm{d}\lambda. \tag{39}$$

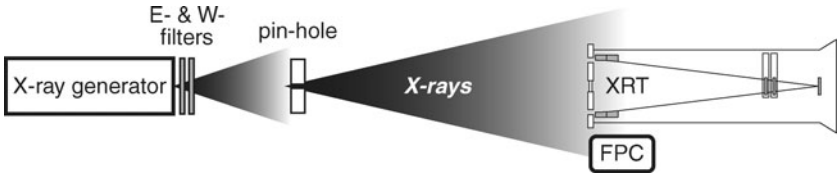

Figure 41 Configuration of the end-to-end test at XRCF.

Figure 10 shows $F(T)$ for each X-ray analysis filter at the launch of *Hinode* and on orbit. According to this figure, we can appreciate that the XRT has a superior ability to observe coronal plasmas over a wide temperature range from less than 1 MK to more than 10 MK.

Using this temperature response [$F(T)$] of XRT, we can estimate the X-ray intensity [I: DN sec^{-1} pixel^{-1}] observed with XRT as follows:

$$I = F(T) \times \mathrm{CEM} \tag{40}$$

for an isothermal corona at a temperature of T, and

$$I = \int F(T) \times \mathrm{DEM}(T)\,\mathrm{d}T \tag{41}$$

for a multi-temperature corona with the differential emission measure [DEM: cm^{-5} K^{-1}], which is defined as

$$\mathrm{DEM} \equiv \frac{\int n_\mathrm{e}(T) n_\mathrm{H}(T)\,\mathrm{d}l}{\mathrm{d}T}. \tag{42}$$

The data number [DN] detected by XRT is given by

$$\mathrm{DN} = I \times t \times p, \tag{43}$$

where t and p are the observation time and the number of pixels used for obtaining the DN, respectively. Using the volume emission measure [VEM: cm^{-3}] defined as

$$\mathrm{VEM} \equiv \int n_\mathrm{e} \times n_\mathrm{H}\,\mathrm{d}l\,\mathrm{d}S = \mathrm{CEM} \times (S \times p), \tag{44}$$

where dS is an unit area of observed solar region, DN is expressed as Equation (2) for an isothermal corona at temperature T.

Appendix E: X-Ray Spectrum at XRCF

We estimate the spectra of X-ray beams at the XRCF. Figure 41 shows the configuration of the end-to-end test performed at the XRCF. The XRCF employs a target-impact type X-ray generator. The five X-ray lines that we used in this test are summarized in Table 8 with target sources, applied acceleration voltage for electrons, and blocking filters. The blocking filters, called E- and W-filters, are introduced to suppress longer and shorter wavelengths than the selected characteristic X-ray line, because lower levels of characteristic X-rays and continuum bremsstrahlung X-rays are also emitted. The X-rays illuminate XRT in an almost-parallel beam, because the small-sized X-ray source is located far from XRT, namely

Table 8 Characteristics X-ray lines used in the end-to-end test at XRCF.

Line	Energy	Wavelength	Source	Voltage	E-filter	W-filter
Mo-L	2.29 keV	5.41 Å	Mo mono	7.0 kV	Lexan[a]	Mo 3.0 μm
Al-K	1.49 keV	8.34 Å	Al mono	7.0 kV	Lexan	Al 18.7 μm
Cu-L	0.930 keV	13.3 Å	Cu mono	1.45 kV	Cu 2.8 μm	Lexan
O-K	0.525 keV	23.6 Å	O on Al	4.0 kV	Cr 0.7 μm	Lexan
C-K	0.277 keV	44.7 Å	C mono	5.0 kV	Lexan	Parylene 10.0 μm

[a]This Lexan is the product of Luxel R/N 6370.

≈ 500 m. A flow proportional counter (FPC) was located beside the XRT to monitor intensity and spectral shape of the X-ray beam.

Here, using the FPC data, we derive the incident X-ray spectrum going into XRT. The FPC detected two humps in the data of each characteristic X-ray line (see Figure 42). Even with the blocking filters, the continuum bremsstrahlung emission component is not completely removed. The main hump comes from the characteristic X-ray line and the other hump from the continuum bremsstrahlung.

To understand the incident X-ray spectrum into the XRT, we need to estimate the spectrum of continuum bremsstrahlung also. On the basis of the thick-target emission model, the continuum bremsstrahlung profile can be described by (Sakao, 1994)

$$I_{\rm thick}(\varepsilon) = \frac{1}{4\pi R^2 K} \int_{\varepsilon}^{\infty} F(E_0) \int_{\varepsilon}^{E_0} E \sigma_{\rm B}(\varepsilon, E)\, {\rm d}E\, {\rm d}E_0, \tag{45}$$

$$\sigma_{\rm B}(\varepsilon, E) = 1.58 \times 10^{-24} \frac{1}{\varepsilon} \ln\left[\left(\frac{E}{\varepsilon}\right)^{\frac{1}{2}} + \left(\frac{E}{\varepsilon} - 1\right)^{\frac{1}{2}}\right], \tag{46}$$

where ε is the photon energy, E the electron energy, E_0 the initial electron energy, F the energy-distribution function of electrons injected to the target [electrons $\sec^{-1}$ keV^{-1}], $\sigma_{\rm B}$ the Bethe – Heitler cross section (Jackson, 1962), $K \equiv 2\pi {\rm e}^4 \ln\Lambda$, $\ln\Lambda$ the Coulomb logarithm (Spitzer, 1962), and R the distance from the X-ray source to the FPC. In our case, because single-energy electrons at an energy of E_{00} were injected, the distribution function can be expressed as

$$F(E_0) = F_{00}\delta(E_0 - E_{00}), \tag{47}$$

where F_{00} is the number of injected electrons per second. The dashed line in Figure 43 is the estimated continuum bremsstrahlung spectrum emitted at the acceleration voltage of 7 kV with Equations (45) – (47). Using the transmission of the E- and W-filters and the efficiency of FPC, the incident continuum spectrum into the FPC is derived as shown by the dotted line in Figure 43. Considering the energy resolution of FPC, which can be written as (Charles and Cooke, 1968)

$$(\Delta E)_{\rm FWHM} = a E^{1/2}, \tag{48}$$

where a is a constant of proportionality, the continuum spectrum detected by the FPC is simulated as shown by a solid curve in Figure 43.

The actual spectrum detected by the FPC is fit by this simulated FPC continuum spectrum and the characteristic X-ray line (Figure 42). The fitting parameters are the constant a in

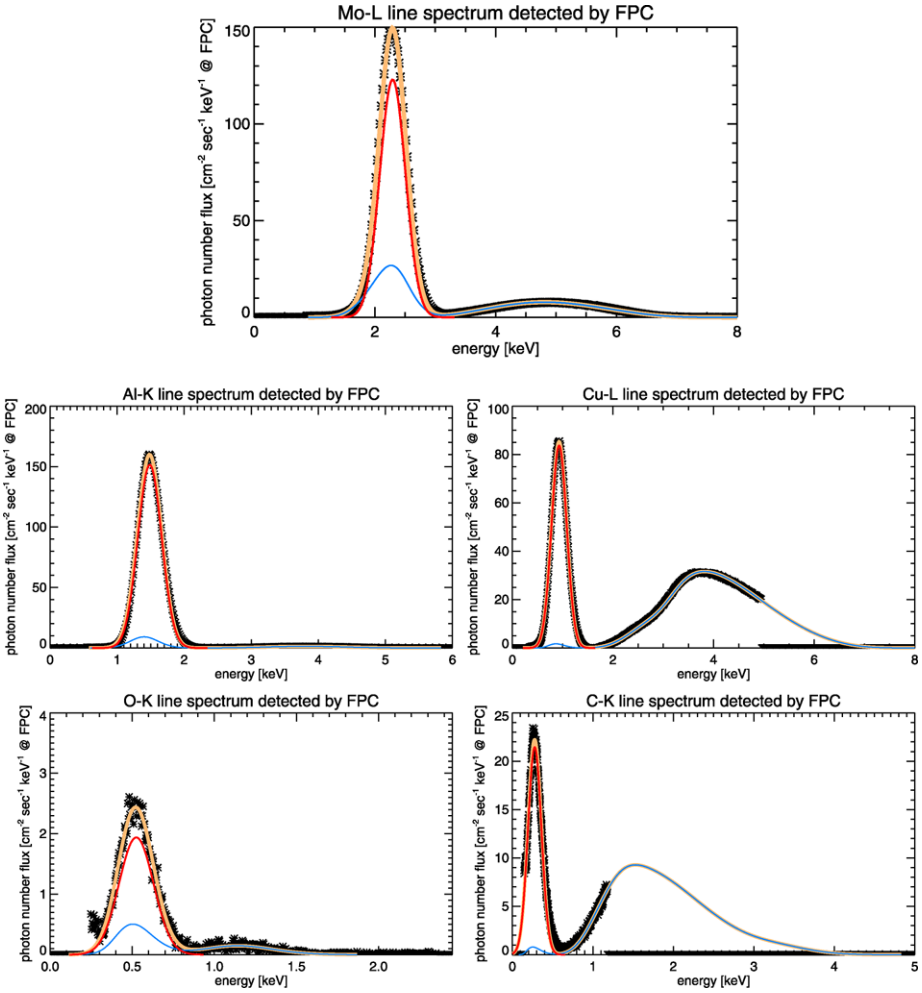

Figure 42 X-ray spectra detected by the flow proportional counter (FPC). The black marks (asterisks) are the data points detected by FPC. The orange line shows the estimated spectrum, which consists of characteristic X-ray line (red line) and continuum bremsstrahlung (blue line).

Equation (48), the number of injected electrons per second F_{00}, and the strength of the characteristic X-ray line represented by a Gaussian shape.

Using the best-fit results in Figure 42, we obtained the incident spectrum going into XRT (see Figure 19). The errors shown by gray areas in Figure 19 are estimated from the photon noise and the energy range of FPC data points. For example, the error bars in O-K and C-K lines are larger than for the other lines, because the total photon number is small in the O-K line case, and because the energy range of the C-K line does not completely cover the continuum. The photon-number fluxes of characteristic X-ray lines and continua are summarized in Table 9. The contribution of the continuum is not negligible even for the Al-K line.

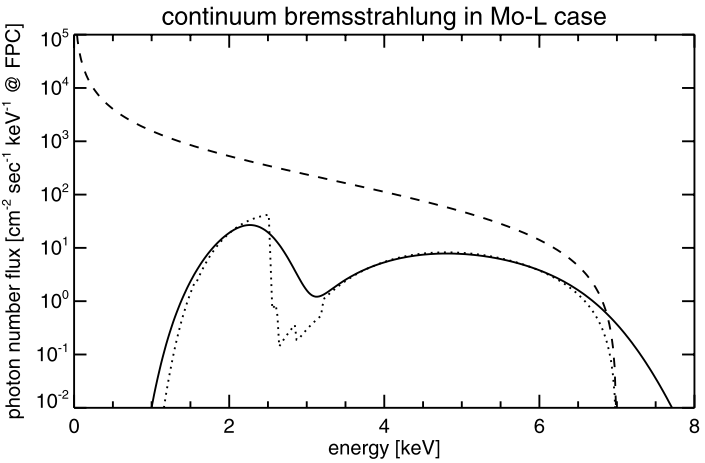

Figure 43 Continuum bremsstrahlung spectrum. The dashed line is the continuum spectrum emitted by 7 keV electrons. The dotted line indicates the incident continuum spectrum into FPC. The solid line shows the continuum spectrum detected by FPC with its energy resolution.

Table 9 Best-fit photon-number fluxes of characteristic X-ray lines and continua.

Line	Energy [keV]	Voltage [kV]	Characteristic line [cm^{-2} sec^{-1}]	Continuum [cm^{-2} sec^{-1}]
Mo-L	2.29	7.0	80.7 (63.6%)[a]	46.1 (35.4%)
Al-K	1.49	7.0	77.4 (90.8%)	7.8 (9.2%)
Cu-L	0.930	1.45	50.8 (36.1%)	89.9 (63.9%)
O-K	0.525	4.0	2.2 (68.7%)	1.0 (31.3%)
C-K	0.277	5.0	7.8 (30.9%)	17.4 (69.1%)

[a]The percentage in parentheses shows the ratio of each component to the total photon flux.

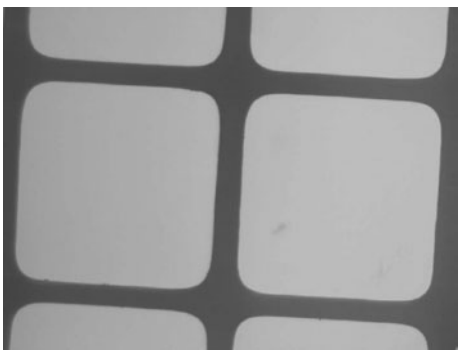

Figure 44 Stainless mesh of Al-mesh filter, obtained by the filter manufacturer with a high-precision digital microscope. This mesh supports the thin Al film of the Al-mesh filter.

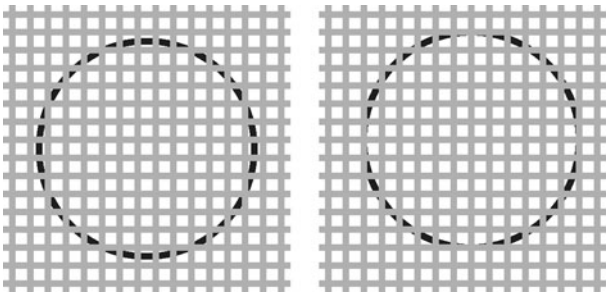

Figure 45 Conceptual images of variation in "annulus transmission". The gray area indicates the mesh of the Al-mesh filter. The black annulus shows the shape of X-rays imaged on the filter. The left and right panels show the difference of annulus transmission caused by the difference in relative position between mesh pattern and annular X-rays. The aspect ratio between the black annulus and gray mesh in this figure is different from the actual aspect ratio between the annular X-rays image and the stainless mesh on the Al-mesh filter.

Figure 46 Variation in "annulus transmission". The left panel is the mesh cell. The black and white regions indicate the mesh wire and open area, respectively. The right panel shows the annulus transmission where the center of annular X-rays imaged is located at the corresponding left panel. White and black mean high and low transmission, respectively.

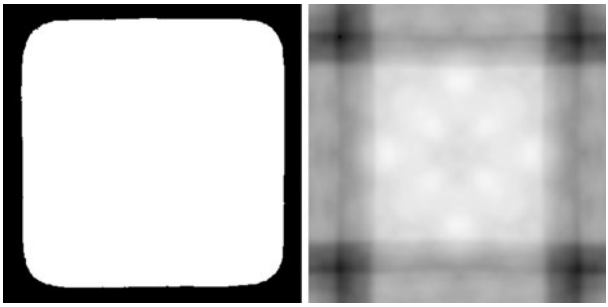

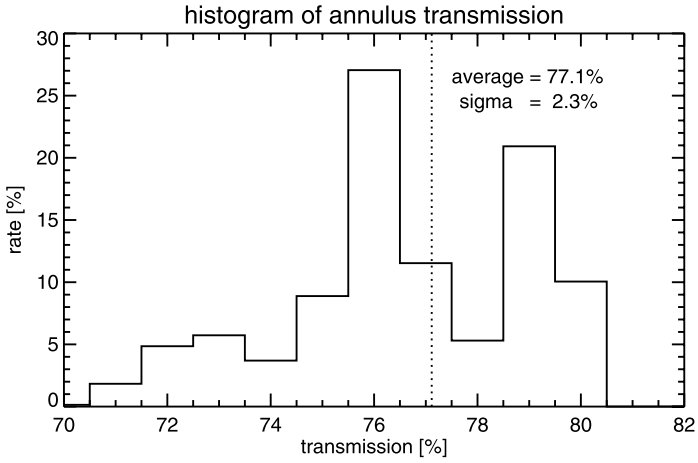

Figure 47 Histogram of annulus transmission based on the right panel of Figure 46. The dotted line indicates the average of annulus transmission: 77.1%.

Appendix F: Variation in Annulus Transmission

The support of the Al-mesh filter is a stainless-steel mesh. Figure 44 is a picture of the mesh taken by the filter manufacturer with a high-precision digital microscope. According

to the manufacturer, the width of the mesh wire and the open area are 38 μm and 330 μm, respectively. On the basis of this measurement, the open area occupies 77% of whole area. We adopt this measured value of 77% for the geometrical open area.

Here we define "annulus transmission" as the fraction of the X-rays passed through the open area of the mesh to the incident X-rays into the mesh. Note that the X-rays pass through the open area without any loss of intensity, while at the wires the X-rays are completely blocked. Hence, the average of the annulus transmission should be consistent with the geometrical open area of the mesh.

The annulus transmission is not uniform and depends on the relative position of the X-rays on the filter with respect to the mesh pattern. However, we do not know this relative position for the flight XRT. Instead, we derive a distribution of the annulus transmission for all possible relative positions, take the average of the distribution as the annulus transmission of the Al-mesh filter and employ the deviation of the distribution as that for the annulus transmission. The procedure is detailed in the following.

The shape of X-rays imaged on the FPAFs is an annulus, because the shape of the XRT aperture is an annulus (see Figure 3). The radius and width of the annular X-ray image are about 4.1 mm and 7.6 μm on the FPAFs, respectively, because the radius and width of XRT annular aperture, focal length, and distance of the focus position to the FPAF are about 170 mm, 0.32 mm, 2700 mm, and 65 mm, respectively. Figure 45 shows some schematic examples of the relationship between the annular X-ray image and the mesh. The gray area indicates the mesh of the Al-mesh filter and the black ring shows the X-ray annulus on the filter. The variation in annulus transmission is shown in Figure 46. The left panel shows a cell (unit opening) of the mesh. The width and height of this cell are both taken as 368 μm on the basis of the manufacturer's measurement. The black and white regions indicate mesh wire and open area, respectively. The right panel shows the annulus transmission in gray scale at the position where the center of the annular X-ray image is located at the corresponding left panel. Figure 47 shows the distribution of the annulus transmission over the varying center position of the X-ray annulus with respect to the mesh pattern. (This is the histogram of the calculated annulus transmission in the right panel of Figure 46.) The average of the annulus transmission is consistent with the geometrical open area of the mesh. However, the annulus transmission has a scatter with the standard deviation [σ] of 2.3%. This σ is also considered in the calibration of the Al-mesh filter thickness.

The uncertainty in the annulus transmission originating from the known relative position of the annulus center with respect to the mesh pattern can thus be evaluated in this way. In this evaluation, we assumed that the shape of the X-ray image on the filter is a perfect annulus. But, in reality, the shape corresponds to the colored area in Figure 3, and this is not symmetrical. Hence, we should consider not only the relative position but also the relative angle between the patterns along the image annulus and the direction of the mesh wires, which also is not known. In order to assess the amount of additional uncertainty caused by this, we calculated the scatter of the annulus transmission due to the uncertainty of the relative position and angle. The standard deviation [σ'] of this scatter (imperfect annulus case) turned out to be almost the same as $\sigma = 2.3\%$ (perfect annulus case). Hence, we claim that our treating the image shape as a perfect annulus is sufficient for deriving the average fraction and σ of the annulus transmission for the X-ray image on the Al-mesh filter.

Appendix G: Spot-Shaped Contaminants on the CCD

After the first bakeout, spot-like patterns appeared in both the X-ray and the G-band data, as shown in Figure 48. Subsequent analyses indicated that the estimated thickness of con-

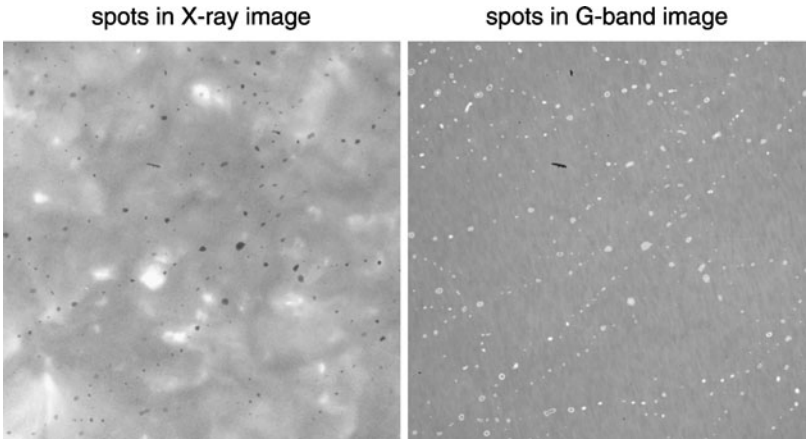

Figure 48 Spot contaminants observed in X-rays and G-band. The spots in the X-ray data are dark, because the spots absorb the X-rays. The spots in the G-band data are bright, since the spots work as anti-reflection coatings.

taminant on the CCD was more than 3000 Å before the first bakeout (see Figure 6). The patterns most likely originate from the condensation of contaminant and are triggered by a bakeout with the thickness of the contaminants accumulated on the CCD exceeding a certain threshold value (the value itself is not known). These spots were not removed at all even with the second bakeout, which lasted for a month. The ratio of spot area to full CCD area was 2.6% at this point (see Table 7). As it took five months before we proceeded with performing the next (third) bakeout, the resultant thickness of the contaminants again exceeded 3000 Å, reaching 3600 Å (see Figure 6). This resulted in the creation of additional contamination spots across the CCD, with an increased spot area ratio of 5.2%. Note, however, that this additional increase was an intentional one; we took the option of keeping a low-temperature-diagnostic capability by removing the accumulated contaminants while accepting an increase in the spot area. The resultant spot distribution is indicated by the black areas in Figure 49. After the third CCD bakeout, we regularly performed the bakeout every three to four weeks. As we guessed, no more spots were created after the third bakeout, as shown in Table 7. The ratio of spot area to full-CCD area has kept to 5.2%.

We investigate the relation between the thickness of some spots measured with their Newton-ring patterns in the G-band and the absorbed X-ray intensities by such spots, and we conclude that the material of spot contaminant is most likely the same material as the laminar contaminant. This result will be presented as a separate paper with a more detailed analysis.

Appendix H: Transmission of Rays Through Three Layers

In Appendix B.2.1, in order to measure the contaminant thickness on the CCD, we used the transmission of visible light into the CCD through contamination layers, Equation (22). Here, we derive this equation.

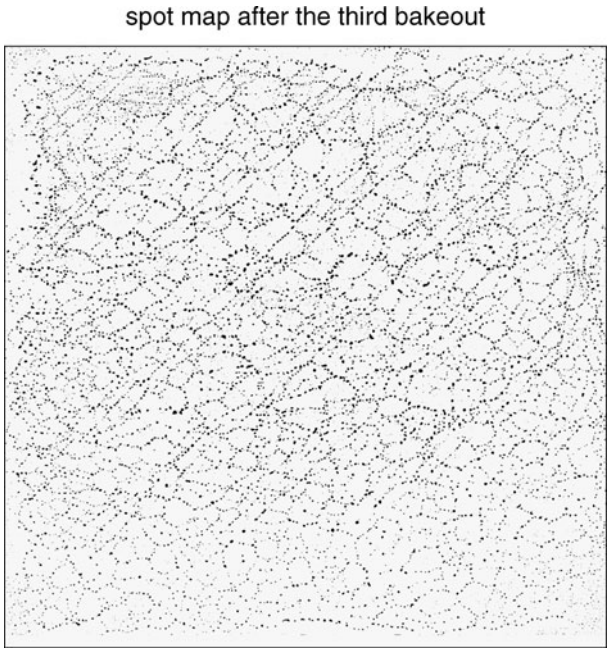

Figure 49 Spot map after the third bakeout. The ratio of spot area to full CCD area is about 5%.

The reflected and transmitted amplitudes [$A_{\rm R}$ and $A_{\rm T}$] of rays at a boundary of two layers whose refractive indexes are n_1 and n_2 are written as

$$A_{\rm R} = A\left(\frac{n_1 - n_2}{n_1 + n_2}\right), \tag{49}$$

$$A_{\rm T} = A\left(\frac{2n_1}{n_1 + n_2}\right), \tag{50}$$

where A is the amplitude of incident rays from the n_1 layer to the boundary.

We consider transmission of three layers as shown in Figure 25. Here, we define A as the amplitude of incident rays in vacuum (n_1 layer), and A_k the complex amplitude of rays which are reflected $2k$ times at the borders of layers ($n_1 - n_2$ border and $n_2 - n_3$ border) and transmitted into the CCD (n_3 layer). Note that the amplitudes of the rays shown by white and black arrows in Figure 25 are A_0 and A_1. A_k is expressed as

$$A_k = A\mathrm{e}^{k\mathrm{i}\Delta\varphi}\left(\frac{2n_1}{n_1 + n_2}\right)\left(\frac{2n_2}{n_2 + n_3}\right)\left\{\left(\frac{n_2 - n_3}{n_2 + n_3}\right)\left(\frac{n_2 - n_1}{n_2 + n_1}\right)\right\}^k, \tag{51}$$

where $\Delta\varphi$ ($= k_2 \times 2d$) gives the phase difference between A_k and A_{k+1}. Hence, the total amplitude [$A_{\rm t}$] of incident rays into the CCD is derived as

$$\begin{aligned} A_{\rm t} &\equiv \sum_{k=0}^{\infty} A_k \\ &= A\left(\frac{2n_1}{n_1 + n_2}\right)\left(\frac{2n_2}{n_2 + n_3}\right)\left[1 - \mathrm{e}^{\mathrm{i}\Delta\varphi}\left\{\left(\frac{n_2 - n_3}{n_2 + n_3}\right)\left(\frac{n_2 - n_1}{n_2 + n_1}\right)\right\}\right]^{-1}. \end{aligned} \tag{52}$$

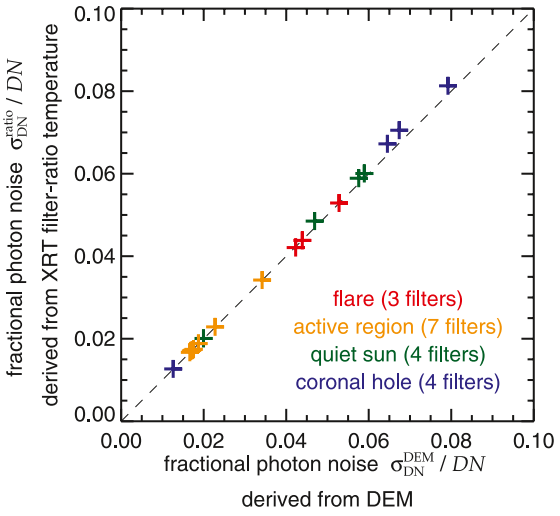

Figure 50 Correlation between the fractional photon noise derived with DEM [σ_{DN}^{DEM}/DN] and with the filter-ratio temperature [σ_{DN}^{ratio}/DN] for four DEMs shown in Table 3. This plot is the case when one month passed after the CCD bakeout, *i.e.* 800 Å of contaminant on the CCD. The dashed line indicates the positions where σ_{DN}^{ratio}/DN is equal to σ_{DN}^{DEM}/DN. The number of analyzed filters is shown in parentheses.

Using the relation between amplitude [$\mathcal{A}$] and intensity [$\mathcal{I}$] in a layer of refractive index n given by

$$\mathcal{I} = n\mathcal{A}\mathcal{A}^*, \tag{53}$$

where * denotes complex conjugation, the intensity [I] in vacuum (n_1 layer in Figure 25) is

$$I = n_1 A A^*, \tag{54}$$

and the total intensity [I_t] detected by the CCD is

$$I_t = n_3 A_t A_t^*. \tag{55}$$

Equation (22) is derived from Equations (52), (54), and (55).

Appendix I: Oxidization of Metal

When the molecular formulae of pure metal and oxidized metal are X and X_AO_B, and the molecular weight of X and O are M_X and M_O (= 16.00), respectively, the reduced thickness [Δd_{pure}] of pure metal by the creation of oxidized metal with a thickness of d_{ox} is

$$\Delta d_{pure} = d_{ox} \times \frac{M_X \times A}{M_X \times A + M_O \times B}, \tag{56}$$

based on the conservation of the number of metal atoms. The information about materials used in our calibration is summarized in Table 4.

Appendix J: Meaning of Photon Noise Calculated with Filter-Ratio Temperature

The photon noise can be derived with Equation (13). For Condition (B) in Section 5.2, we investigated how much photon noise is expected in the observed data with the single temperature of the filter-ratio temperature. However, the actual solar corona may have a multi-temperature structure. Hence, here we discuss the meaning of the estimate of the photon

noise with the filter-ratio temperature. Figure 17 shows the correlation between the fractional photon noise derived with DEM [$\sigma_{\rm DN}^{\rm DEM}$/DN] and with the filter-ratio temperature [$\sigma_{\rm DN}^{\rm ratio}$/DN] for four DEMs (regions), as summarized in Table 3. $\sigma_{\rm DN}^{\rm ratio}$ is the photon noise calculated with the filter-ratio temperature [$T_{\rm ratio}$] and Equation (13). $\sigma_{\rm DN}^{\rm DEM}$ is the photon noise derived with the DEM as in the following steps.

i) We calculate the photon noise [$\sigma_{\rm DN}$] for each temperature bin of DEM with Equation (13).

ii) We derive the net photon noise of step *i*) as $\sigma_{\rm DN}^{\rm DEM} = \sqrt{\sum \sigma_{\rm DN}^2}$.

The values of $\sigma_{\rm DN}^{\rm ratio}$ and $\sigma_{\rm DN}^{\rm DEM}$ are calculated for all filters which are included in the suitable filter pairs in Figure 14 with the typical values of the coronal structures in Table 3. On the basis of this figure, we can say that $\sigma_{\rm DN}^{\rm ratio}$ matches $\sigma_{\rm DN}^{\rm DEM}$ well, which is the actual photon noise.

This equality can be understood as follows. Since the amount of plasma at the DEM peak is dominant, its photon noise mainly affects $\sigma_{\rm DN}^{\rm DEM}$. In the temperature range where the DEM peak is located, the conversion factor [$K^{(2)}$] from observed DN to $\sqrt{\sigma_{\rm DN}}$ (see Equation (13)) is almost constant for the filters which are included in the suitable filter pairs (see Figures 13 and 14). For example, in a temperature range of 3 – 4 MK, where the active region has the DEM peak (see Figure 16), $K^{(2)}$ for Al-poly, Ti-poly, and med-Be filters varies as the factors of 1.07, 1.11, and 1.02, respectively (see the bottom panel in Figure 12). Hence, $\sigma_{\rm DN}^{\rm DEM}$ well matches $\sigma_{\rm DN}^{\rm ratio}$, since $\sigma_{\rm DN}^{\rm ratio}$ is derived from $K^{(2)}$ at $T_{\rm ratio}$, and $T_{\rm ratio}$ is close to the DEM peak temperature (see Section 5.3). We note that, for temperature ranges other than the DEM peak, $K^{(2)}$ varies with as a factor of typically two – four. However, since *i*) the photon noise is a function of $\sqrt{K^{(2)}}$ (see Equation (13)) and furthermore, *ii*) in this temperature range, the contribution of photon noise to $\sigma_{\rm DN}^{\rm DEM}$ is smaller than at the DEM peak, the variation of $K^{(2)}$ in these temperature ranges does not significantly affect $\sigma_{\rm DN}^{\rm DEM}$.

Appendix K: Notes

K.1. Contaminant Material

In Appendix B.3.1, we identified the contaminant material as a long-chain organic compound whose chemical composition, density, and refractive index are similar to those of DEHP, although DEHP is not used in the XRT. This means that the actual contaminant material is narrowed down to the material whose refractive index and density are close to 1.5 and 1 g cm^{-3}, respectively.

Next let us discuss the chemical composition of the actual contaminant material. Since the atomic number of silicon is about twice as large as carbon and oxygen, *i.e.* the cross section of silicon to X-rays is certainly larger, the existence of silicon affects the X-ray transmission certainly. In fact, when we assume that the contaminant contains some silicon atoms, the discrepancy between the observed and expected X-ray intensity ratios rises, as shown in Figure 33. Hence, we conclude that there are no silicon atoms in the contaminant material.

On the other hand, since the atomic numbers of carbon and oxygen (also nitrogen) are comparable, and that of hydrogen is much smaller than carbon and oxygen, *i.e.* hydrogen is much more transparent to X-rays, some slight differences in numbers of such atoms for a long-chain organic compound do not make any significant difference in the transmission of X-rays. Hence, although we cannot precisely identify the chemical composition of the

contaminant material, it is acceptable for the calibration of the XRT that we tentatively employed DEHP as the contaminant material. We note that the identified property of the contaminant, where the chemical composition is a long-chain organic compound without silicon, the refractive index being ≈ 1.5, and the density being $\approx 1\ \mathrm{g\,cm^{-3}}$, is a common property of materials which are widely used for satellites, and which are well known to be possible sources of contamination.

K.2. G-Band Method for CCD Contamination Analysis

In Appendix B.2.1, we explained the method to measure the thickness of the contaminant on the CCD using G-band data. The G-band intensity oscillation shown in Figure 24 is essentially expressed by Equation (23). However, there are two differences between the calculated G-band intensity enhancement, with the anti-reflection effect of Equation (23), and the observed one that is characterized by the empirical model given by Equation (26).

The first is the refractive indices of the contaminant. In this article, we obtained the refractive index of the contaminant with the following two methods.

i) In Appendix B.2.2, from the observed amplitude of intensity enhancement in the G-band, the refractive index of contaminant is estimated to be ≈ 1.4.
ii) In Appendix B.3.1, the decrease in X-ray intensities caused by the accumulation of contaminant can be well explained by adopting a well-known material whose refractive index and density of contaminant are 1.5 and $0.986\ \mathrm{g\,cm^{-3}}$, respectively, as the contaminant material.

This difference may be explained with the possible hypothesis that the density of contaminant actually accumulated is lower than the contaminant in its usual state (as, *e.g.*, commercial products), because the contaminant material is an organic compound and its accumulation was formed under a vacuum deposition process but with a much slower rate than the standard ones in laboratories, and the accumulated contaminant most likely consists of sparsely-structured molecules (rather than the dense crystalline structure). Hereafter, we call this state "sparse". The same trend as this hypothesis is seen in the case of the C-poly filter as described in the last paragraph of Appendix A.2. Generally, the refractive index [n_{sparse}] and density [ρ_{sparse}] of material in the sparse state are smaller than those [n_{usual} and ρ_{usual}] in the usual state. If the above hypothesis holds, method *i*) gives the refractive index of contaminant in the sparse state. On the other hand, in method *ii*), we identified the refractive index and density in the usual state from among the possible candidates of contaminant (see Table 5). Hence, the difference in the refractive indexes in methods *i*) and *ii*) is caused by the different states of the contaminant.

Next, we consider the effect of this difference on the calibration results. On the basis of Equation (25), the smaller refractive index gives the thicker contaminant. Meanwhile, the smaller density gives the longer attenuation length [l_{att}] in Equation (20). Hence, the X-ray transmission calculated with n_{sparse} and ρ_{sparse} would be close to the transmission with n_{usual} and ρ_{usual}. We note that even if the actual state of the contaminant is not sparse, *i.e.* even if the density of the actual contaminant is the same as the usual state, the difference in refractive indices (1.4 and 1.5) is only 7%, and then the difference in the estimated thickness of the contaminant on the CCD is also 7%. Since the maximum thickness of the contaminant is about 3600 Å (see Figure 6), the maximum error in the estimate is about 250 Å. This error is smaller than the accumulated thickness of the contaminant on the thinner FPAFs (see Figure 7), and it is negligibly small compared to the metal thicknesses of the thicker

filters. Hence, we conclude that, whether the hypothesis holds or not, the difference in refractive indices does not significantly affect the results of XRT calibration, and we may adopt $n_{\rm usual} = 1.5$ and $\rho_{\rm usual} = 0.986\ {\rm g\,cm^{-3}}$ for the calibration.

The second one is the decay of the oscillation amplitude. We consider this to be caused by the inhomogeneous accumulation rate of the contaminant. In Appendix B.2.3, we demonstrated that the accumulation rate of the contaminant at the CCD center is larger than at the edges of the CCD. This effect might appear in the 512×512 pixels data which are used to make the G-band intensity plot (Figure 24). The intensity oscillation of each portion of the 512×512 pixels will have a different phase. The G-band intensity plot is the average of such different oscillations, which are sine curves with different phases. Because the phase difference becomes larger and larger as time passes, the oscillation amplitude of the G-band intensity enhancement decays.

On the basis of Equation (25), the thickness of contaminant on the CCD is derived only from the refractive index of the contaminant and the period of the intensity oscillation. Hence, we expect that the refractive index of ≈ 1.5 and the oscillation period in Figure 24 give the average thickness of the contaminant on the CCD area of 512×512 pixels, which is reliable enough for the XRT calibration.

K.3. Accumulation Profile of Contaminant on the CCD

When we estimated the thickness of the contaminant accumulated on the CCD with the visible-light intensity profile (Appendix B.2.2), we assumed a constant accumulation rate for the contaminant between two successive bakeouts. However, actually, we see a rapid accumulation of contaminant right after the CCD bakeout, while for the rest of each period the rate is almost constant (see the right panel of Figure 29). Nevertheless, the assumption of constant accumulation for the entire period between two successive bakeouts is a valid one for the calculation of the XRT effective area, because the contaminants accumulated on the FPAFs are much thicker than the difference between the actual and estimated thickness with the above assumption, *i.e.* such a difference is negligible.

K.4. DEM Model Used for the Analysis

In Appendix B.3, we calibrated the contaminant thickness on the FPAFs with the observed X-ray data and DEM in the quiet Sun. When we performed the calibrations described in this article, the DEM model in the quiet Sun derived by Brooks and Warren (2006) was the latest result available. Hence, we adopted their DEM model for our analysis. Brooks and Warren (2006) derived the DEM of the quiet Sun from a data set taken with SOHO/EIT, SOHO/CDS, and TRACE on 1 May 1998. More recently Brooks *et al.* (2009) analyzed the DEM with 45 data sets observed with *Hinode*/EIS in the period from January to April 2007. The profiles of the DEMs studied in these two articles are very similar up to at least $\log T \approx 6.2$ K in all cases. We confirmed that the calibrated contaminant thicknesses on the FPAFs with the DEMs from Brooks and Warren (2006) and Brooks *et al.* (2009) are consistent.

K.5. Source Location of the Contaminant

We found that there is remarkable similarity between the observed spatial distribution of the contaminant across the CCD and the simulated result by Urayama *et al.* (2008) for the case where the contaminant was assumed to come from in front of the CCD (see Figure 30).

Meanwhile, we found that the contamination is triggered by the operational heater which warms the rear end of the telescope tube up to about 20°C. On the basis of this circumstantial evidence, we suspect that the contaminant most likely originates from somewhere in front of the CCD, in the telescope tube.

K.6. Future Plan for the Calibration

As we mentioned in Appendix A.2, we consider the calibration of thick filters (med-Be, thick-Al, and thick-Be filters) with ground-based test data to be not ideal, although the difference between calibrated and actual X-ray transmission of them should be small. For further calibration of the thick filters, we need to take enough data sets where XRT observes intense X-ray sources, *e.g.*, active regions and flares, with thick filters. Calibration with on-orbit observational data is for our future work.

Also, in order to supplement our calibration, we plan to perform the following cross-calibrations: *i*) between *Hinode*/XRT and *Hinode*/EIS, and *ii*) between XRT and GOES13/SXI, which is a grazing-incidence X-ray telescope, like XRT.

References

Acton, L.W., Weston, D.C., Bruner, M.E.: 1999, *J. Geophys. Res.* **104**, 14827.
Brooks, D.H., Warren, H.P.: 2006, *Astrophys. J. Suppl. Ser.* **164**, 202.
Brooks, D.H., Warren, H.P., Williams, D.R., Watanabe, T.: 2009, *Astrophys. J.* **705**, 1522.
Charles, M.W., Cooke, B.A.: 1968, *Nucl. Instrum. Methods* **61**, 31.
Collura, A., Barbera, M., Inzerillo, G., Mirabello, F., Sciortino, S., Serio, S.: 1994, *SPIE* **2280**, 206.
Dere, K.P.: 2007, *Astron. Astrophys.* **466**, 771.
Dere, K.P., Cook, J.W.: 1979, *Astrophys. J.* **229**, 772.
Dere, K.P., Landi, E., Mason, H.E., Monsignori Fossi, B.C., Young, P.R.: 1997, *Astron. Astrophys. Suppl. Ser.* **125**, 149.
Dere, K.P., Landi, E., Young, P.R., Del Zanna, G., Landini, M., Mason, H.E.: 2009, *Astron. Astrophys.* **498**, 915.
Feldman, U., Mandelbaum, P., Seely, J.F., Doschek, G.A., Gursky, H.: 1992, *Astrophys. J. Suppl. Ser.* **81**, 387.
Freeland, S.L., Handy, B.N.: 1998, *Solar Phys.* **182**, 497.
Golub, L., Deluca, E., Austin, G., Bookbinder, J., Caldwell, D., Cheimets, P., *et al.*: 2007, *Solar Phys.* **243**, 63.
Hara, H., Tsuneta, S., Lemen, J.R., Acton, L.W., McTiernan, J.M.: 1992, *Publ. Astron. Soc. Japan* **44**, L135.
Henke, B.L., Gullikson, E.M., Davis, J.C.: 1993, *Atom. Data Nucl. Data Tables* **54**, 181.
Jackson, J.D.: 1962, *Classical Electrodynamics*, Wiley, New York.
Kano, R., Tsuneta, S.: 1995, *Astrophys. J.* **454**, 934.
Kano, R., Sakao, T., Hara, H., Tsuneta, S., Matsuzaki, K., Kumagai, K., *et al.*: 2008, *Solar Phys.* **249**, 263.
Kosugi, T., Matsuzaki, K., Sakao, T., Shimizu, T., Sone, Y., Tachikawa, S., *et al.*: 2007, *Solar Phys.* **243**, 3.
Landi, E., Feldman, U., Dere, K.P.: 2002, *Astrophys. J. Lett.* **139**, L281.
Martens, P.C.H., Cirtain, J.W., Schmelz, J.T.: 2002, *Astrophys. J. Lett.* **577**, L115.
Mewe, R., Gronenschild, E.H.B.M., van den Oord, G.H.J.: 1985, *Astron. Astrophys. Suppl. Ser.* **62**, 197.
Mewe, R., Lemen, J.R., van den Oord, G.H.J.: 1985, *Astron. Astrophys. Suppl. Ser.* **65**, 511.
Ogawara, Y., Takano, T., Kato, T., Kosugi, T., Tsuneta, S., Watanabe, T., *et al.*: 1991, *Solar Phys.* **136**, 1.
Osantowski, J.F.: 1982, *Proc. SPIE* **338**, 80.
Powell, F.R., Vedder, P.W., Lindblom, J.F., Powell, S.F.: 1990, *Opt. Eng.* **29**, 614.
Sakao, T.: 1994, Ph.D. Thesis, University of Tokyo.
Schmelz, J.T., Kashyap, V.L., Saar, S.H., Dennis, B.R., Grigis, P.C., Lin, L., *et al.*: 2009a, *Astrophys. J.* **704**, 863.
Schmelz, J.T., Saar, S.H., DeLuca, E.E., Golub, L., Kashyap, V.L., Weber, M.A., *et al.*: 2009b, *Astrophys. J. Lett.* **693**, 131.
Schmelz, J.T., Saar, S.H., Nasraoui, K., Kashyap, V.L., Weber, M.A., DeLuca, E.E., *et al.*: 2010, *Astrophys. J.* **723**, 1180.

Shimizu, T., Katsukawa, Y., Matsuzaki, K., Ichimoto, K., Kano, R., Deluca, E.E., *et al.*: 2007, *Publ. Astron. Soc. Japan* **59**, 845.
Spitzer, L. Jr.: 1962, *Physical of Fully Ionized Gases*, 2nd edn., Interscience, New York.
Tsuneta, S., Acton, L., Bruner, M., Lemen, J., Brown, W., Caravalho, R., *et al.*: 1991, *Solar Phys.* **136**, 37.
Urayama, F., Bando, T., Kano, R., Hara, H., Narukage, N., Sakao, T.: 2008, *Japan Soc. Aeronaut. Space Sci.* **56**, 536.
Vaiana, G.S., Krieger, A.S., Timothy, A.F.: 1973, *Solar Phys.* **32**, 81.
Vernazza, J.E., Reeves, E.M.: 1978, *Astrophys. J. Suppl. Ser.* **37**, 485.
Warren, H.P., Brooks, D.H., Winebarger, A.R.: 2011, *Astrophys. J.*, submitted. arXiv:1009.5976v1.